8-2022

Determination of the functional role of Rab-GGT in Physcomitrium patens.

Hyun Jin Jung
University of Louisville

DETERMINATION OF THE FUNCTIONAL ROLE OF RAB-GGT IN *PHYSCOMITRIUM PATENS*

By

Hyun Jin Jung
B.S., Chonnam National University, South Korea, 2014
M.S., University of Louisville, 2017

A Dissertation
Submitted to the Faculty of the
College of Arts and Sciences of the University of Louisville
in Partial Fulfillment of the Requirements for the Degree of

Doctor of Philosophy
in Biology

Department of Biology
Division of Molecular, Cellular, and Developmental Biology
University of Louisville
Louisville, Kentucky

August 2022

DETERMINATION OF THE FUNCTIONAL ROLE OF RAB-GGT IN *PHYSCOMITRIUM PATENS*

By

Hyun Jin Jung
B.S., Chonnam National University, South Korea, 2014
M.S., University of Louisville, 2017

A Dissertation Approved on

July 27, 2022

by the following Dissertation Committee:

_____
Dr. Mark P. Running, Principal Advisor

_____
Dr. Michael H. Perlin

_____
Dr. David J. Schultz

_____
Dr. Kenneth E. Palmer

_____
Dr. Dae-Sung Hwangbo

DEDICATION

This dissertation is dedicated to the Living God, my Savior; to my beloved grandmother, Suk Hwa Ryu; to my dear parents, Hwa Shik Jung and Yoo Kyoung Kim; and to my cherished sister, Yoo Jin Jung. This Ph.D. journey and dissertation work would not have been possible without their love, care, support, guidance, and encouragement.

ACKNOWLEDGEMENTS

I would like to express my sincere gratitude to my advisor, Dr. Mark P. Running, for his advice, encouragement, guidance, and support throughout my entire doctoral program. This Ph.D. journey would not have been possible without his invaluable advice, continuous help, patience, and flexibility.

I would also like to express my deepest appreciation to all my committee members: Dr. Mike H. Perlin, Dr. David J. Schultz, Dr. Kenneth E. Palmer, and Dr. Dae-Sung Hwangbo for their support, encouragement, and assistance in improving my critical and analytical thinking skills. I learned a lot from their valuable scientific guidance and feedback.

My appreciation is also extended to all my graduate teaching assistant (GTA) supervisors, Dr. Linda Fuselier, Dr. Rachel Hopp, and Dr. Jeffery A. Masters, for their support, patience, and flexibility over the past few years.

I am also thankful to Hector Eduardo Mendoza from Dr. Perlin's lab for teaching me qRT-PCR and helping me troubleshoot, Landon Teer from Dr. Joseph Chen's lab and David Grimm from Dr. Michael Menze's lab for helping me visualize the immunostained samples, and Anwar Hossain from Dr. Noppadon Sathitsuksanoh's lab for training me on the solid assay.

Many thanks to my former and current lab members: Dr. Liang Bao, Dr. Parul Singh, Dr. Susana Martinez Perez, Jesse Lee Rozsa, and Matthew McCracken Hart for their smiles, friendship, and support. I feel very blessed to have such wonderful

colleagues. I would like to especially thank Dr. Bao for all his scientific guidance and assistance. He has taught me all the *P. patens*-related experiments and techniques in detail and helped me generate amiRNA transformants. It was a great privilege to work and study under his guidance.

I am also thankful to the faculty and staff members in the Department of Biology, Dr. Sarah Emery, Dr. Perri Eason, Doris Meadows, and Terri Norris, for all the help during a period of difficulty throughout my entire doctoral program.

Finally, words cannot express gratitude to all my family members in South Korea, Suk Hwa Ryu, Hwa Shik Jung, Yoo Kyoung Kim, and Yoo Jin Jung for their endless love, prayers, encouragement, and support.

ABSTRACT

DETERMINATION OF THE FUNCTIONAL ROLE OF RAB-GGT IN *PHYSCOMITRIUM PATENS*

Hyun Jin Jung

July 27, 2022

Protein prenylation, a common lipid post-translational modification, is required for growth and development in eukaryotes. Rab geranylgeranylation involves the addition of one or two 20-carbon geranylgeranyl moieties to Rab-GTPase target proteins, which regulate intracellular vesicle trafficking. The reaction is carried out by heterodimeric Rab geranylgeranyltransferase (Rab-GGT), which is composed of two associated α- and β-subunits, with the assistance of an additional protein called Rab escort protein (REP). Loss of function of the Rab-GGT α subunit *RGTA1* has not been reported in any plant. While knockout of either of the two β subunits *RGTB1* or *RGTB2* results in no phenotype in the moss *Physcomitrium patens (P. patens*, formerly *Physcomitrella patens)*, in the flowering plant *Arabidopsis thaliana,* knockout of *RGTB1* results in loss of apical dominance and photomorphogenic and gravitropic defects, and knockout of *RGTB2* results in a subtle growth defect in certain cells. These results showed that both Rab-GGT β subunits in *P. patens* are redundant, but *RGTB2* in *Arabidopsis* could not fully compensate for the loss of function of *RGTB1* and vice versa. Previous studies in our lab showed that complete knockout of any *P. patens* Rab-GGT components (*RGTA1, RGTB1* & *RGTB2, REP*) appears to be lethal, since no viable single mutant plants of *RGTA1* or

REP and double mutant plants of *RGTB1* and *RGTB2* were recovered. Therefore, the biological function of Rab-GGT remains largely unknown. Here we have generated *P. patens* transgenic plants containing artificial miRNA constructs targeting each Rab-GGT component by an inducible knockdown system, and systematically analyzed the phenotypes upon induction. The results showed that knockdown of either *RGTA1* or *REP*, or knockdown of *RGTB1* in a *rgtb2* knockout background (or vice versa) resulted in defects in tip growth (polar cell elongation), reduced or incomplete caulonema differentiation, and an altered response towards exogenous phytohormones. This dissertation may help to elucidate the functional role of Rab-GGT in *P. patens*, as well as provide fundamental insights into key *P. patens* developmental processes and environmental responses.

TABLE OF CONTENTS

PAGE

LIST OF TABLES

TABLE PAGE

LIST OF FIGURES

FIGURE PAGE

CHAPTER I

INTRODUCTION

Lipid post-translational modification on proteins in plants

Lipid post-translational modification, which is found in all eukaryotic cells, is the covalent attachment of lipid moieties—including fatty acids, isoprenoids, cholesterol, and glycolipids such as glycosylphosphatidylinositols (GPI) and glycosylinositolphosphorylceramide (GIPC) anchors—to specific amino acids. The lipid-modified proteins lead to facilitating targeting and localization, which aids in enhancing protein-membrane association as well as protein-protein interactions by their increased hydrophobicity (Thompson Jr. & Okuyama, 2000; Running, 2014; Hemsley, 2015). Genetic studies have revealed that these processes play essential roles in diverse plant growth processes and developmental mechanisms, including the establishment of cell identity, cell differentiation, cell adhesion, polar cell elongation, and environmental responses (Thompson Jr. & Okuyama, 2000; Running, 2014).

There are three most common intracellular lipid modifications, characterized by the type of lipid group being linked and the region of modification in the protein sequence (Yalovsky et al., 1999; Voet et al., 2013). They include N-myristoylation, prenylation, and S-acylation (palmitoylation). N-myristoylation is an irreversible stable modification involving the addition of a 14-carbon saturated myristoyl chain to the N-terminal glycine residue of proteins through an amide bond by an N-myristoyltransferase

(NMT) enzyme (Farazi et al., 2001; Gordon et al., 1991; Johnson et al., 1994; Resh, 2006). Prenylation is the addition of isoprenoid lipid units, the 15-carbon farnesyl or the 20-carbon geranylgeranyl group, to the cysteine residue or residues at the C-terminal portion of proteins via a thioether bond (Zhang & Casey, 1996). S-acylation is the attachment of a saturated long-chain fatty acid, usually a 16-carbon palmitate or 18-carbon stearate, to the cysteine residue of proteins via a thioester bond (Hallak et al., 1994; Resh, 2006; Hemsley et al., 2013). In contrast to N-myristoylation or prenylation, S-acylation is a reversible modification and is mediated by a large protein family, protein S-acyltransferases (PATs) containing an Asp-His-His-Cys amino acid motif within a cysteine-rich domain (DHHC-CRD) (Hemsley et al., 2005; Batistic, 2012). In addition, unlike the other lipid modifications which have consensus target sequences at C- and N-terminus for modification, there are no specific target sequences for S-acylation to occur, though it often accompanies N-myristoylation or prenylation (Resh, 2006; Roth et al., 2006).

In terms of enzymology, these lipid modifications of proteins appear evolutionarily conserved in animals, plants, and fungi (Yalovsky et al., 1999; Galichet & Gruissem, 2003; Maurer-Stroh et al., 2003; Hemsley, 2015). However, recent studies have shown that these modifications in plants appear to be different when it comes to proteins modified and physiological requirements of lipid-modified proteins (Hemsley, 2015). In the case of N-myristoylation, plants contain up to twice as many proteins shown or predicted to be N-myristoylated than fungi, and the loss of NMT activity shows defects in functions unique to plants (Boisson et al., 2003; Marmagne et al., 2007). For example, *AtNMT1* knockout mutants show a seedling lethal phenotype, disorganized

shoot meristem, a dwarfing phenotype, and defects in post-embryonic development, including flower differentiation, fruit maturation, and fertility; *AtNMT2* knockout results in a delay in flowering time (Pierre et al., 2007). In plants, the loss of protein prenylation activity leads to individuals with reduced fitness, reduced fertility, and developmental defects, while in mammals and yeast loss of this activity appears to be lethal (Running et al., 2004). In regard to S-acylation, which is not as well understood due to the lack of a specific target sequence and the large numbers of protein acyltransferases that carry out the reaction, proteomic studies have recently revealed that plants contain around 600 putative S-acylated (palmitoylated) proteins affecting a diverse array of proteins that regulate the cellular and physiological processes (Hemsley et al., 2013).

This chapter identifies the various aspects of lipid modification, specifically prenylation, on target proteins. Furthermore, to understand the specific functional roles of prenylation in plant developmental processes, the changes or manipulation in lipidation enzymes have been performed in *Arabidopsis* and *P. patens*. This chapter describes the characteristics of phenotypes of those mutants, potentially indicating important roles for prenylation in various signal transduction pathways, metabolic systems, and regulatory mechanisms.

Protein prenylation in *Arabidopsis*

Protein prenylation is the most well-studied post-translational modification. It involves the transfer of either three (15-carbon farnesyl group) or four (20-carbon geranylgeranyl group) isoprene units to cysteines near the C-terminus of proteins via thioether linkages (Zhang & Casey, 1996; Crowell & Huizinga, 2009; Sorek et al., 2009). There are three distinct heterodimeric enzymes consisting of an α subunit and a β subunit

that carry out three different protein prenylation reactions: protein farnesyltransferase (PFT) involved in farnesylation, protein geranylgeranyltransferase-I (PGGT-I) involved in geranylgeranylation, and Rab geranylgeranyltransferase (Rab-GGT, also called protein geranylgeranyltransferase-II, PGGT-II) involved in Rab-geranylgeranylation (Maurer-Stroh et al., 2003; McTaggart, 2006; Running, 2014). These three separate enzymes recognize different motifs of target proteins and catalyze the attachment of different numbers and types of a polyisoprene lipid group (a single 15-carbon farnesyl or single or dual 20-carbon geranylgeranyl group) to one or two C-terminal cysteine residues for modification (Zhang & Casey, 1996; Running, 2014).

PFT and PGGT-I have a shared common α subunit and unique β subunits that have only 25-35% similarity in sequence, providing substrate specificity (Running, 2014). PFT and PGGT-I recognize a C-terminal Ca_1a_2X motif of the target protein in which 'C' is cysteine that potentially can be farnesylated by PFT using the 15-carbon farnesyl group and geranylgeranylated by PGGT-I using a single 20-carbon geranylgeranyl group, 'a' is an aliphatic amino acid, and the final position 'X' is any amino acid but shows preference for certain residues. The identity of 'X' determines which enzyme acts on the target protein. If the 'X' is alanine, cysteine, glutamine, methionine, or serine, the protein will be recognized by PFT; however, if the 'X' is leucine (Ca_1a_2L motif), the protein will be recognized by PGGT-I (Maurer-Stroh et al., 2003; McTaggart, 2006; Nguyen et al., 2010). There are many well-known proteins prenylated by PFT and PGGT-I that are known to be responsible for cellular signal transduction pathways, such as members of the small G proteins related to the Ras proteins, transducin, rhodopsin kinase, fungal mating factors, heterotrimeric G proteins γ

subunits, nuclear protein lamin B, cyclic GMP phosphodiesterase α subunit, and phosphorylase kinase α and β subunits (Maltese, 1990; Stimmel et al., 1990; Casey, 1992; Gelb, 1995). As oncogenic Ras mutations are among the most prevalent mutations in cancer cells and appear to be associated with various types of human cancers through overactivation of proliferation, farnesyltransferase inhibitors have been developed as anti-cancer therapeutics (Wang et al., 2017).

Rab-GGT consists of distinct α and β subunits, which share a weak homology in amino acid sequence (only 20~30% similarity) with their counterparts in PFT and PGGT-I (Running, 2014). Rab-GGT contains a wider spectrum of C-terminal target sequences, which includes dual modified XCC, XCXC, XCCX, CCXX, and CCXXX, and the singly modified CXXX, where 'C' is the prenylated cysteine, and 'X' is a non-specific amino acid (Maurer-Stroh et al., 2003; Running, 2014). While PFT and PGGT-I do not require any additional protein for recognizing target proteins, Rab-GGT requires a cofactor protein, Rab escort protein (REP), to recognize unprenylated Rab GTPases and transfers two geranylgeranyl groups to two cysteines near the C-terminus (Leung et al., 2006). Rab GTPases constitute the largest family of the Ras-related GTPase superfamily (Pereira-Leal et al., 2001; Vernoud et al., 2003; Grosshans et al., 2006). They are responsible for regulating organelle biogenesis and intracellular membrane trafficking, such as vesicle budding, delivery, tethering, and fusion with the target membrane, all of which are essential processes in plants (Grosshans et al., 2006; Leung et al., 2006). Mutation in Rab-GGT prenylation also causes several human diseases (McTaggart, 2006). For instance, deficiency in human REP-1 leads to choroideremia disease, an X-linked retinal dystrophy (Cremers et al., 1992; Merry et al., 1992; Seabra et al., 1992). It was formerly

believed that Rab-GGT only prenylates Rab GTPases when it is combined with REP for target protein specificity (Leung et al., 2006; Guo et al., 2008). However, we have recently demonstrated that, unlike mammalian and yeast Rab-GGT, *Arabidopsis* Rab-GGT prenylates not only diverse Rab-GTPases in the presence of REP, but also non-Rab GTPases *in vitro* independent of REP (Shi et al., 2016).

Many molecular and genetic studies have revealed that the components and mechanisms of prenylation are generally conserved in plants (Galichet & Gruissem, 2003; Crowell & Huizinga, 2009; Sorek et al., 2009; Table 1-1). In *Arabidopsis*, PFT and PGGT-I are made up of a single copy of the shared α subunit *plp* and β subunits *era1* and *ggb*, respectively (Cutler et al., 1996; Ziegelhoffer et al., 2000; Caldelari et al.,2001; Maurer-Stroh et al., 2003; Running et al., 2004; Johnson et al., 2005; Table 1-1). Interestingly, Rab-GGT in *Arabidopsis* contains two copies of α *(RGTA1, RGTA2*) and β *(RGTB1, RGTB2*) subunit homologs, along with a REP homolog, while they are present in a single copy in yeast and animals (Lange & Ghassemian, 2003; Maurer-Stroh et al., 2003; Hála et al., 2005; Crowell & Huizinga, 2009; Leung et al., 2006; Hála et al., 2010; Table 1-1).

Table 1-1

Putative protein prenylation components in *Arabidopsis (At)* and *P. patens (Pp)*.

Enzyme	α subunit	α subunit gene name(s)		β subunit	β subunit gene name(s)	
Farnesyltransferase	PFT/PGGTα	*At PLP*	*Pp PLP*	PFTβ	*At ERA1*	*Pp ERA1*
Geranylgeranyltransferase	PFT/PGGTα	*At PLP*	*Pp PLP*	PGGTβ	*At GGB*	*Pp GGB*
Rab geranylgeranyltransferase	Rab-GGTα	*At RGTA1*, *At RGTA2*	*Pp RGTA1*	Rab-GGTβ	*At RGTB1*, *At RGTB2*	*Pp RGTB1*, *Pp RGTB2*
Unknown	α subunit-like	*At PPAL*	*Pp PPAL1*, *Pp PPAL2*			

PFT and PGGT-I function in *Arabidopsis*

Plants have been used as an ideal model system to study prenylation mechanisms *in vivo* because of the relatively mild phenotypes of knockout mutants compared with the lethality observed in the homologous mutants in yeast and animals (Schafer et al., 1990; Diaz et al., 1993). Many molecular and genetic studies in *Arabidopsis* have revealed the significant roles of prenylation in regulating growth, developmental processes, and environmental responses.

While complete knockout of PFT and PGGT-I in yeast and animals results in lethality, mutations in the α subunit shared between PFT and PGGT-I in *Arabidopsis*, called *PLURIPETALA* (*PLP*) remain viable and fertile, but cause severe developmental defects including increased floral organ numbers (extra floral organs), much larger shoot meristems, and stem fasciation (He et al., 1991; Running et al., 2004). *PLP* mutants also show much slower growth, delayed flowering, abscisic acid (ABA) hypersensitivity in inhibition of seed germination, and enhanced drought tolerance (Running et al., 2004).

Mutations in the *Arabidopsis* PFT β subunit, called *ENHANCED RESPONSE TO ABSCISIC ACID 1* (*ERA1,* also called *WIGGUM*), are also hypersensitive to ABA in the maintenance of seed dormancy and guard cell function (Cutler et al., 1996; Pei et al., 1998; Allen et al., 2002; Brady et al., 2003; Running, 2014). However, *era1* mutants show mild developmental phenotypes in comparison to the *plp* mutants. These include larger shoot meristem, wider floral meristem, slightly shorter stature, slightly slower growth, and increased disease sensitivity (Running et al., 1998).

Mutations in the *Arabidopsis* PGGT-I β subunit *GERANYLGERANYL TRANSFERASE BETA SUBUNIT (GGB)* cause no detectable phenotypes and do not have

any developmental defects under normal growth conditions. *ggb* mutants show slightly increased responses (enhanced sensitivity) in stomata closure under exogenous ABA, and slightly enhanced lateral root formation under exogenous auxin (Johnson et al., 2005).

Phenotypes of *era1 ggb* double mutants resemble *plp* knockout mutants, which provides evidence that they are the only PFT/PGGT-I β subunits in plants (Johnson et al., 2005). Again, mutations in *Arabidopsis era1* or *ggb* result in mild phenotypes compared to *plp* knockout mutants. In addition, overexpression of *ggb* in *Arabidopsis* mutants lacking a functional *era1* gene can significantly rescue the *era1* phenotype (Johnson et al., 2005). These results suggest that there is a considerable functional overlap between *Arabidopsis* PFT and PGGT-I, indicating that PFT can compensate for the loss of PGGT-I and vice versa (Running et al., 2004). Overlap in specificity is also supported by biochemical evidence (Andrews et al., 2010). This target cross-specificity of PFT and PGGT-I in *Arabidopsis* is greater than in yeast and mammals, which have been observed in a small number of target proteins and have a poor substrate cross-specificity in most cases (Zhang & Casey, 1996; Maurer-Stroh & Eisenhaber, 2005; McTaggart, 2006).

Rab-GGT function in *Arabidopsis*

Progress on identification and functional characterization of plant Rab-GGT lagged behind other members of the prenyltransferases family. In early studies, the presence of Rab-GGT activity was shown in total cell extracts of tomato, tobacco, and *Arabidopsis* (Loraine et al., 1996; Yalovsky et al., 1996; Hála et al., 2005). The functional studies on specific subunits have only been conducted recently.

Mutations in one of the two *Arabidopsis* Rab-GGT β subunits, *RGTB1,* cause a series of defects in phenotypes and many physiological processes; e.g., dwarf size,

epinastic and smaller leaves, abnormally developed flowers, loss of apical dominance, abnormally delayed senescence, self-infertility, impaired shoot growth and gravitropism with normal root growth and gravitropism, constitutive photomorphogenesis, deregulation of both exocytosis and endocytosis, and accumulation of unprenylated Rab proteins in the cytosol (Hála et al., 2010; Gutkowska et al., 2015). Mutations in the other *Arabidopsis* Rab-GGT β subunit, *RGTB2,* are indistinguishable from wild-type plants in their overall morphology and the time of flowering, but show abnormal tip growth, including root hair and pollen tube deformations (Gutkowska et al., 2015). While the *Atrgtb1* and *Atrgtb2* single knockout mutants are viable, the *Atrgtb1 Atrgtb2* double mutant is non-viable, due to male sterility, shrunken pollen, abnormal exine structure, and strong disorganization of the endoplasmic reticulum membranes. These results suggest partial genetic redundancy between Rab-GGT β subunits, as each of the single knockout mutants has a distinct set of phenotypes possibly from differential expression (Hála et al., 2010; Thole et al., 2014; Gutkowska et al., 2015; Shi et al., 2016).

Mutations in the *Arabidopsis* Rab-GGT α subunits, either *RGTA1* or *RGTA2*, have not been reported. By using *in vitro* prenylation assays, we have characterized all four α-β combinations among *RGTA1/2* and *RGTB1/2* form heterodimers. *RGTA1-RGTB1* and *RGTA1-RGTB2* can prenylate a wide variety of Rab-GTPases in the presence of *AtREP*, indicating that *RGTB1* and *RGTB2* are biochemically redundant when combined with *RGTA1 in vitro* (Shi et al., 2016). There is not any detectable Rab-GGT activity in *RGTA2-RGTB1* and *RGTA2-RGTB2*, possibly due to a 12-amino acid insertion in the middle of the third (III) protein prenyltransferase α subunit (PPTA) repeat that possibly disrupts the *RGTA2* helical domain (Shi et al., 2016).

As mentioned earlier, *Arabidopsis* Rab-GGT can also prenylate certain non-Rab small GTPases *in vitro* independent of *AtREP*, along with various Rab-GTPases targets dependent on *AtREP* (Shi et al., 2016).

The moss *Physcomitrium patens* as a model plant system

The first land plants (embryophytes) originated approximately 470 million years ago and emerged from the earliest terrestrial plant ancestor, charophyte green algae (Wickett et al., 2014; Delwiche & Cooper, 2015; Wellman & Strother, 2015). The earliest group of land plants, called bryophytes, comprised of hornworts, mosses, and liverworts, successfully colonized diverse land habitats and paved the way for plant terrestrialization (Kramer, 2009). The transition from aquatic to the terrestrial mode of life required adaptations to extreme variations in light, temperature, and water availability. Abiotic stresses caused by UV-light exposure, varying temperature, and drought necessitated extensive modifications from signaling and physiological processes to dramatic changes in body plan (Floyd & Bowman, 2007; Rensing et al., 2008). Due to the phylogenetic position of *P. patens* as a bridge between unicellular green algae and seed vascular plants, and its complete sequenced and well-annotated genome, the moss became an ideal model for comparative genomic analyses of the evolution of multicellularity and photosynthesis facilitated the conquest of the land (Bowman et al., 2007; Floyd & Bowman, 2007; Rensing et al., 2008; Rensing et al., 2020).

Furthermore, *P. patens*' simple cultivation, easy propagation, regeneration ability into a whole new plant from any tissue or single cell under hormone-free conditions, and haploid-dominant life cycles allowing the direct forward analysis of mutants with a recessive phenotype make this moss an attractive model system (Cove, 2005; Cove et al.,

2009). The relatively simple morphology of *P. patens* with few tissues that contain a limited number of cell types (e.g., single-cell layers or filaments) that can absorb water and nutrients via the whole surface makes it ideal for microscopy and subcellular localization studies, analysis of phytohormone, biotic, and abiotic stress responses (Cove et al., 2006; Strotbek et al., 2013). *P. patens*' unique ability among plants for high efficiency targeted mutagenesis via homologous recombination and highly specific endogenous gene silencing mechanism via microRNA (miRNAs) facilitates its use for genetic studies and analysis (Schaefer & Zrÿd, 1997; Cove, 2005; Cove et al., 2006; Khraiwesh et al., 2008; Strotbek et al., 2013). Putting all these favorable features together, the moss *P. patens* has been established as an excellent experimental system for studying plant cellular, physiological, and evolutionary developmental processes (Reski et al., 2018).

The life cycle of the moss *Physcomitrium patens*

The life cycle of *P. patens* alternates between a dominant haploid gametophyte (as in bryophytes) phase and a minor diploid sporophyte (as in vascular plants) phase (Prigge & Bezanilla, 2010). In the initial stage of gametophyte development, *P. patens* germinates from a single haploid spore and undergoes tip growth and cell division of apical and subapical cells to produce protonema, a branched filamentous network of cells (Cove & Knight, 1993; Prigge & Bezanilla, 2010). The protonema filaments consist of two distinct cell types: chloronema and caulonema differentiated from select chloronemal apical cells in an auxin-dependent manner (Cove et al., 2006; Prigge et al., 2010; Jang & Dolan, 2011). Chloronemal cells, the first cell type to emerge from the germinating spore, are rich in chloroplasts providing abundant photosynthesis and have perpendicular cell

plates; whereas caulonemal cells, which are thinner, longer, and faster-growing cells, contain fewer chloroplasts with oblique cell plates and are mainly involved in land colonization and nutrient absorption (Cove & Knight, 1993; Menand et al., 2007; Strotbek et al., 2013). In the latter stage of gametophyte development, *P. patens* shows a drastic transition from filamentous two-dimensional structure, the protonema, to a three-dimensional leafy shoot or gametophore by the appearance of meristematic buds (Cove & Knight, 1993; Schaefer & Zrÿd, 2001). The gametophore is composed of a photosynthetic non-vascularized shoot-like stem, which carries the leaves and the reproductive organs (the male organ antheridia and the female organ archegonia), and anchoring root-like filamentous rhizoids at the basal part of the stem. When water is present, motile spermatozoids from the antheridia are capable of swimming to the archegonia and fertilize the single egg in its basal cavity. The resulting zygote develops into an embryo and then into the diploid sporophyte that will yield about 5,000 haploid spores within the spore capsule, called sporangium, through meiosis. When the sporophyte becomes ripe, the sporangium breaks open to release the spores which will start a new gametophytic cycle (Schaefer & Zrÿd, 2001; Strotbek et al., 2013).

The main cell fate transitions, metabolism, and development in *P. patens* can be manipulated by hormonal and nutritional factors (Schaefer & Zrÿd, 2001; Landberg et al., 2020). Auxin stimulates the transition from chloronema to caulonema and the initiation of rhizoids, both also induced by exogenous auxin treatment (Sakakibara et al., 2003; Prigge et al., 2010; Jang & Dolan, 2011; Landberg et al., 2020). In addition, disruption of auxin transport induces a branching form of the gametophore shoots and sporophyte (Fujita et al., 2008; Bennett et al., 2014). Exogenous ABA application facilitates the

formation of vegetative diaspores (spherical, thick-walled cells called brachycytes or brood cells) from subapical chloronemal cells, inducing their tolerance to unfavorable environmental conditions such as desiccation and freezing (Goode, et al., 1993; Arif et al., 2019). The addition of cytokinin promotes the transition from a two-dimensional to a three-dimensional growth phase by accelerating the bud formation of caulonemal side-branch initial cells, while the auxin suppresses branch initiation (Reski & Abel, 1985; Coudert et al., 2015). Also, it has been found that calcium fluxes alter the establishment of cell polarity, branching patterns and fate of the protonema cells (Schaefer & Zrÿd, 2001).

Cell lineage analyses and cell biological studies can be easily performed on *P. patens* due to its developmental pattern differentiating from the spore through protonema stage to gametophyte (closely resembling the basic organism of most land plants) and similar responses to environmental stimuli and growth substances as those observed in other land plants (Bezanilla et al., 2003; Cove, 2005).

Prenylation in *P. patens* and unknown features of Rab-GGT

In order for cells to differentiate specialized forms and establish their identity, signal transduction is important, which relies on post-translational modifications that determine protein activity such as its activation/deactivation, localization, and function by changes in gene expression (Antimisiaris & Running, 2014; Running, 2014). Three types of commonly studied intracellular post-translational modifications include prenylation, N-myristoylation, S-acylation (Running, 2014). We are especially interested in the mechanism of protein prenylation and its role in developmental signaling and plant growth processes. To identify whether the biological roles of prenylation in plant

development are conserved among plants, our study focuses on the comparison of two model systems with fully sequenced genomes: *Arabidopsis thaliana* (*At*) and *Physcomitrium patens* (*Pp*, formerly *Physcomitrella patens*), representative angiosperm and bryophyte, respectively. Interestingly, gene families encoding proteins with fundamental functions in flowering plant development are conserved in the genome of *P. patens* (Floyd & Bowman, 2007; Rensing et al., 2008).

As in other Eukaryotes, *P. patens* contains three separate heterodimeric enzymes that perform prenylation: protein farnesyltransferase (PFT), protein geranylgeranyltransferase-I (PGGT-I), and Rab geranylgeranyltransferase (Rab-GGT, also called protein geranylgeranyltransferase-II, PGGT-II) (Maurer-Stroh et al., 2003; McTaggart, 2006; Running, 2014). Both *Arabidopsis* and *P. patens* have a single copy of *PLP*, the shared α subunit of PFT and PGGT-I, and each β subunit, *ERA1* and *GGB*, two copies of the Rab-GGT β subunit (*PpRGTB1* and *PpRGTB2*), and Rab Escort Protein (*REP*). Unlike *Arabidopsis*, *P. patens* contains a single copy of the Rab-GGT α subunit (*PpRGTA1*) and two copies of *PPAL* (*PpPPAL1* and *PpPPAL2*) (Thole et al., 2014; Table 1-1).

To see whether the role of prenylation previously identified in *Arabidopsis* developmental processes is similar in *P. patens*, we took advantage of *P. patens'* capacity to perform targeted gene knockouts via homologous recombination for reverse genetic functional analysis of all of the PFT, PGGT-I, and Rab-GGT subunits (Schaefer & Zrÿd, 1997; Cove, 2005; Thole et al., 2014). According to Thole et al. (2014), the PGGT β subunit knockouts, *Ppggb* mutants, display the most striking phenotype compared to wild type. The cells are small and round and remain undifferentiated with no adhesion and no

asymmetric or polarized elongation (no filament formation). Upon cell division, each cell becomes a separate individual organism, resembling unicellular algae. The knockout lines of the shared α subunit of PFT and PGGT-I, *Ppplp* mutants, exhibit small, round cells lacking any sign of cell adhesion, as in *Ppggb* mutants. However, while cell division rate and viability are not affected in *Ppggb* mutants, *Ppplp* mutants show a much slower division rate and significantly reduced survival rate. The PFT β subunit knockouts, *Ppera1* mutants, are much less severe, as the cells show branched filamentous growth, but with reduced cell elongation and delayed differentiation. The single knockout of either of the two Rab-GGT β subunits, *PpRGTB1* or *PpRGTB2,* results in no phenotype under our standard conditions, suggesting possible functional redundancy of these putatively duplicated genes. We have failed to recover any viable knockouts of the single Rab-GGT α subunit *PpRGTA1,* nor *PpREP*, nor the double Rab-GGT β subunit mutant *PpRGTB1*; *PpRGTB2,* indicating an absolute requirement for Rab-GGT activity in *P. patens* viability. The knockouts of either *PpPPAL1* or *PpPPAL2* result in lethality, indicating that both genes are also essential for survival (Thole et al., 2014).

From the phenotypes of protein prenylation mutants in *Arabidopsis* and *P. patens*, prenylation seems to play some similar roles in development, including cell fate acquisition, differentiation, and cell elongation. However, as *P. patens* mutants show much more severe phenotypes with loss of polarity establishment, no cell adhesion, and reduced viability compared to *Arabidopsis* mutants, prenylation may be responsible for such additional roles in *P. patens* (Thole et al., 2014). Both similarities and differences have been found in PFT and PGGT-I mutants between the two species. PFT/ PGGT-I α subunit (*plp*) mutants remain viable in both *Arabidopsis* and *P. patens*, although the loss

of *plp* in *P. patens* has a much more dramatic effect. Thus, these data indicate that PFT and PGGT-1 are not necessary for survival. Enlarged meristem by a delay in differentiation and the smaller stature and reduced leaf lobing by a failure of cell elongation observed in *Atplp* mutants and small, round cells by lack of cell adhesion in *Ppplp* mutants indicate a role for prenylation in cell fate specification and differentiation (Running et al., 2004; Thole et al., 2014). In the case of PFT and PGGT-I β subunit mutants (*era1* and *ggb,* respectively), *Atera1* mutants show much more dramatic effects with reduced differentiation, elongation, fertility compared to *Atggb* mutants, which are indistinguishable from wild type under normal growth conditions (Running et al., 1998; Johnson et al., 2005; Bonetta et al., 2000; Yalovsky et al., 2000). However, the opposite pattern is seen in *P. patens,* as *Ppera1* mutants have much less severe phenotypes with slower growth rate and limited cell elongation than *Ppggb* mutants, which are defective in growth and differentiation with no polar cell elongation. The establishment of polarity is not affected in any *Arabidopsis* prenylation mutants, but no sign of polarity is observed in *Ppggb* and *Ppplp* mutants (Thole et al., 2014). The loss of PFT/ PGGT-I α subunit, *plp,* has a much stronger effect than the loss of either β subunit, *era1* or *ggb,* in both *Arabidopsis* and *P. patens.* But there is a difference as *Atplp* mutants resemble *Atera1* mutants, but more severe, while *Ppplp* mutants resemble *Ppggb* mutants, but more severe (Running et al., 2004; Thole et al., 2014).

Again, because the complete knockouts of any *P. patens* Rab-GGT components appear to be lethal, their specific functions in *P. patens* growth and developmental processes have not been established. In this dissertation, we report the generation of *P. patens* Rab-GGT knockdown mutants by transient RNAi approaches to reduce the

expression of *PpRGTA1*, the two potentially redundant *PpRGTB* genes *(PpRGTB1* in a *rgtb2* knockout background, *PpRGTB2* in a *rgtb1* knockout background), and *PpREP* to see phenotypic changes with a partial loss of function and reveal the biological function of each component. After the morphological and developmental studies, in-depth genetic, molecular, and metabolic studies will follow, allowing us to investigate the hypothesis that the roles of Rab-GGT in growth, development, environmental stress, and hormonal responses are conserved at least partially among disparate species of plants.

CHAPTER II

PHYSCOMITRIUM PATENS RAB-GGT IS ESSENTIAL FOR PROPER CELL MORPHOGENESIS AND POLARIZED CELL GROWTH

Introduction

Post-translational modification of proteins involves proteolysis and/or a covalent attachment of small chemical groups (e.g., phosphorylation and acetylation), carbohydrates (e.g., glycosylation)/lipids (e.g., lipidation), or small proteins (e.g., ubiquitination) and is a key mechanism for regulating most eukaryotic proteins (Walsh et al., 2006; Deribe et al., 2010). These modifications critically influence many cellular processes and biological functions such as enzymatic activity, protein function, stability and localization, various signaling cascades, DNA repair, and cell polarity, growth and division, etc. (Thompson Jr. & Okuyama, 2000; Walsh et al., 2006; Running, 2014; Audagnotto & Dal Peraro, 2017). Lipid-based post-translational modifications, which involve the binding of various lipid moieties to certain amino acids within target proteins, are of increasing interest for their two crucial roles of facilitating subcellular targeting of the lipid-modified proteins and promoting protein-protein interactions by increasing hydrophobicity. Four major classes of protein lipidations identified in plants include cholesterylation, prenylation, N-myristoylation, and S-acylation, also known as S-palmitoylation, the attachment of GPI/GIPC anchors, prenyl (e.g., farnesyl, geranylgeranyl), myristoyl, and acyl (e.g., palmitoyl) groups, respectively (Yalovsky et

al., 1999; Thompson Jr. & Okuyama, 2000; Triola, 2012; Voet et al., 2013; Running, 2014; Hemsley, 2015). While GPI/GIPC anchors are restricted to extracellular proteins found in the outer face of the plasma membrane, all other known protein lipidations are found on cytoplasmic proteins associated with, or essential to, the inner face of the plasma membrane or the cytoplasmic face of internal membranes (Hemsley, 2015). Of the three types of known intracellular protein lipidations, protein prenylation is the most well-investigated. Protein prenylation is an irreversible covalent post-translational modification found in all eukaryotic cells and involves the attachment of either 15-carbon farnesyl or 20-carbon geranylgeranyl isoprenoid groups to cysteine residues at or near the C-terminus of proteins via a thioether linkage (Zhang & Casey, 1996; Sorek et al., 2009; Running, 2014). These processes are catalyzed by three separate heterodimeric enzymes called protein prenyltransferases: **protein farnesyltransferase** (PFT), which adds a 15-carbon farnesyl group to proteins that contain a C-terminal CaaX motif (C = Cys, a = aliphatic amino acid, X = any amino acid; Ala, Cys, Gln, Met, or Ser), **protein geranylgeranyltransferase-I** (PGGT-I), which adds a 20-carbon geranylgeranyl group to proteins that contain a C-terminal CaaL motif (C = Cys, a = aliphatic amino acid, when X = Leu), and **Rab geranylgeranyltransferase** (Rab-GGT, also called protein geranylgeranyltransferase-II, PGGT-II), which adds two geranylgeranyl groups to a broader range of C-terminal target sequences that mainly contain two cysteine residues, including XCC, XCXC, XCCX, CCXX, and CCXXX (C = Cys, X = non-specific amino acid) (Maurer-Stroh et al., 2003; Leung et al., 2006; McTaggart, 2006; Running, 2014).

PFT and PGGT-I have a shared common α subunit and unique β subunits that have only 25-35% similarity in sequence, providing substrate specificity (Running,

2014). There are many signaling proteins prenylated by PFT and PGGT-I that play pivotal roles in cell growth and differentiation, including members of the small G proteins related to the Ras proteins, transducin, rhodopsin kinase, fungal mating factors, heterotrimeric G proteins γ subunits, nuclear protein lamin B, cyclic GMP phosphodiesterase α subunit, and phosphorylase kinase α and β subunits (Maltese, 1990; Stimmel et al., 1990; Casey, 1992; Gelb, 1995). Mutations in the Ras family are the initiating genetic events in various types of human cancers, and this led to the development of farnesyltransferase inhibitors as anti-cancer agents (Nguyen et al., 2010; Wang et al., 2017).

Very little is known about Rab-GGT activity in plants and its regulatory proteins in the cascade of events leading to double geranylgeranylation. Rab-GGT consists of distinct α and β subunits, which share a weak homology in amino acid sequence (only 20~30% similarity) with their counterparts in PFT and PGGT-I (Running, 2014). In contrast to PFT and PGGT-I, Rab-GGT acts on its target proteins with the assistance of an additional protein called Rab escort protein (REP) (Leung et al., 2006). Considering the case of mammalian and yeast Rab-GGT, it was formerly believed that Rab-GGT exclusively prenylates Rab proteins (Rab GTPases), hence the name (Pereira-Leal et al., 2001; Vernoud et al., 2003; Grosshans et al., 2006). However, we have recently established that *Arabidopsis* Rab-GGT prenylates not only diverse Rab-GTPases *in vitro* in a REP-dependent manner, but also certain non-Rab GTPases *in vitro* in a REP-independent manner (Shi et al., 2016).

Rab proteins are small GTPases that form the largest family of the Ras superfamily and are conserved throughout all eukaryotes (Pereira-Leal and Seabra, 2001;

Zerial and McBride, 2001; Vernoud et al., 2003). The Rab family is considerably more diverse in mammalian and higher plant (roughly 60) than in yeasts (around 10), which appears to reflect the greater complexity and diversity of Rab functions in specialized tissues and cell types (Bock et al., 2001; Pereira-Leal and Seabra, 2001; Pinheiro et al., 2009). Phylogenetic analyses show that 57 distinct Rabs present in *Arabidopsis* are categorized into just eight subfamilies and lack 80% of the Rab subfamilies found in mammals (as more than 60 Rabs identified in mammals are grouped into forty subfamilies), showing expansion of the size of each *Arabidopsis* Rab subfamily (Rutherford and Moore, 2002; Vernoud et al., 2003; Pinheiro et al., 2009).

Rabs play pivotal roles in mediating various events involved in organelle biogenesis and intracellular membrane trafficking, such as vesicle budding, delivery, tethering, and fusion with target compartment (Pereira-Leal and Seabra, 2001; Leung et al., 2006). The Rab-mediated vesicular traffic is crucial for completion of plant growth and development by establishing and maintaining cell polarity that regulates membrane asymmetries (Cheung & Wu, 2008; Yang et al., 2020). The extremely polarized cell growth is referred to as “tip growth”, in which the cell expansion occurs exclusively at the tip area and the growth rate is exceedingly rapid, while maintaining cell shape and structural integrity. Examples of the specialized cells that undergo tip growth are root hairs, pollen tubes, rhizoids, and caulonema (Campanoni & Blatt, 2006; Menand et al., 2007; Szumlanski & Nielsen, 2009; Zhou et al., 2020). Alteration in Rab activity leads to defects in polarized growth, such as the formation of shorter, bulged tips with a slower rate of growth (Szumlanski & Nielsen, 2009).

Just like many other small GTPases, Rab proteins behave as molecular switches between two conformations, inactive GDP-bound and active GTP-bound forms, interacting with various regulators and effector proteins. REP recognizes the Rab-GGT substrate, newly synthesized GDP-bound Rab protein, and helps escort the two cysteines near the C-terminus of Rab to the Rab-GGT α-β heterodimer for the addition of usually two geranylgeranyl groups (Anant et al., 1998). Specific regulators called guanine nucleotide exchange factor proteins (GEFs) accelerate the exchange from GDP to GTP, leading to Rab activation, which can recruit effectors engaged in vesicular traffic machinery. Guanine nucleotide activating proteins (GAPs) then deactivate the Rab by enhancing the intrinsic GTP hydrolysis, resulting in the dissociation of effectors. GDP dissociation inhibitors (GDIs) extract inactive Rab from a membrane and diffuse it back to the cytosol for another round of activation (Pfeffer & Aivazian, 2004; Gutkowska & Swiezewska, 2012; Pylypenko et al., 2017). Unprenylated Rab proteins do not associate with membrane and are unable to perform their normal functions (Gomes et al., 2003).

Plants have been used as an ideal model system to study prenylation mechanisms *in vivo* due to their relatively mild phenotypes of knockout mutants compared with the lethality observed in the homologous mutants in yeast and animal (Schafer et al., 1990; Diaz et al., 1993). Until recently, almost all molecular and genetic studies on plant protein prenylation have been obtained only from *Arabidopsis thaliana* through loss of mechanisms, and the resulting biological impact have revealed significant roles of prenylation in regulating growth, developmental processes, and environmental responses. However, whether these roles are conserved among plants remains largely unknown (Running, 2014; Hemsley, 2015). *Physcomitrium patens* (*P. patens*) has emerged as an

excellent model for evolutionary developmental studies and comparative genomic studies with flowering plants (primarily *Arabidopsis*) because of its phylogenetic position as a bridge between algae and seed plants, well-annotated genome, and a remarkable ability for reverse-genetic analysis of gene function by homologous recombination-mediated gene targeting (Schaefer & Zryd, 1997; Kamisugi, 2005; Kamisugi et al., 2008). *P. patens'* high efficiency of gene targeting, which allows the precise mutagenesis (inactivation or modification) of specific sequences, is exceptional among plants and has enabled the generation of gene-targeted knockout mutants (Schaefer & Zryd, 1997). Furthermore, *P. patens'* haploid-dominant life cycle allows the direct forward analysis of mutants with loss-of-function phenotypes caused by disruption of one allele (recessive mutations) (Cove, 2005; Cove et al., 2009).

In contrast to the genome of yeast and animals, which contains only one copy of each Rab-GGT subunit, the *Arabidopsis* genome has duplicated Rab-GGT α subunits, *AtRGTA1* and *AtRGTA2*, and β subunits, *AtRGTB1* and *AtRGTB2* (Leung et al., 2006). Unlike *Arabidopsis*, *P. patens* contains a single copy of the Rab-GGT α subunit, *PpRGTA1*, but has duplicated β subunits as in *Arabidopsis*, *PpRGTB1* and *PpRGTB2* (Thole et al., 2014). Phylogenetic sequence analysis indicates that the β subunits duplicated independently, after the split in the two lineages (Thole et al., 2014). Mutation in the Rab-GGT α subunit have not been reported in any plant. In both *Arabidopsis* and *P. patens*, loss-of-function mutations in the single copy of Rab-GGT β subunits are viable, but the double *rgtb1 rgtb2* mutants are non-viable, indicating possible functional redundancy of these putatively duplicated genes (Shi et al., 2016). In *Arabidopsis*, knockouts of *AtRGTB2* are indistinguishable from wild-type plants in their overall

morphology and the time of flowering, but show abnormal tip growth, including root hair and pollen tube deformations (Gutkowska et al., 2015). Knockouts of *AtRGTB1* show defects in phenotypes and many physiological processes such as a dwarfing phenotype, loss of apical dominance and gravitropic defects, suggesting the partial redundancy of *AtRGTB1* and *AtRGTB2* because *AtRGTB2* could not fully compensate for the loss of function of *AtRGTB1* (Hála et al., 2010; Gutkowska et al., 2015, Shi et al., 2016). However, in *P. patens,* single knockouts of either of two Rab-GGT β subunits, *PpRGTB1* or *PpRGTB2,* result in no phenotype under standard conditions, indicating the complete redundancy between the β subunit homologs. Also, loss of the *P. patens* single Rab-GGT α subunit or *PpREP,* and double Rab-GGT β subunits result in lethality, demonstrating an absolute requirement for Rab-GGT activity in viability (Thole et al., 2014).

Because of (1) lethality of the gene disruption of any *P. patens* Rab-GGT components and (2) functional redundancy of the several homologs *PpRGTB1* and *PpRGTB2*, their specific functions in *P. patens* growth and developmental processes have not been determined. In this research, we take advantage of *P. paten*'s RNA interference (RNAi) mechanisms (Bezanilla et al., 2003) for functional analysis of Rab-GGT related genes. Transient RNAi assays have been especially useful in *P. patens* to evaluate the function of gene families and genes that are required for survival (Bezanilla et al., 2003; Bezanilla et al., 2005; Khraiwesh et al., 2008; Prigge et al., 2010). For instance, *P. patens* has three profilin genes essential for survival. Contrary to the difficulty in characterizing functions due to non-viable mutant upon gene knockout, the simultaneous silencing of all profilin genes by a transient RNAi knockdown approach has helped to elucidate important roles in tip growth and cell division (Vidali et al., 2007). In addition, *P. patens*

contains two myosin XI genes and two class II formin genes that are functionally redundant. Simultaneous silencing of the two functionally redundant genes also revealed that they are required for proper actin organization mediating polarized growth (Vidali et al., 2009; Vidali et al., 2010). Thus, we implemented posttranscriptional gene silencing strategy via artificial microRNAs (amiRNAs) in *P. patens* for the specific knockdown of essential gene and observation of deviating phenotypes (Khraiwesh et al., 2008). We have generated *P. patens* transgenic plants containing amiRNA constructs targeting each Rab-GGT component by an inducible knockdown system using pPGX8 as a destination vector and β-estradiol as an inducer, and systematically analyzed the phenotype upon induction (Kubo et al., 2013). Assessment of genetic modification of the model system was performed by using polymerase chain reaction (PCR) and agarose gel electrophoresis analysis, in combination with Sanger sequencing (Eurofins Genomics, Louisville, KY, USA) and the knockdown was confirmed indirectly by observing the resulting phenotype and directly by using quantitative real-time PCR (qRT-PCR).

Here a detailed phenotypic characterization of *P. patens* Rab-GGT knockdown mutants is provided. Our findings show that knockdown of either RGTA1 or REP, or knockdown of RGTB1 in a *rgtb2* knockout background (or vice versa) results in various morphological and cell polarity establishment defects, such as retarded growth by affected polar cell elongation, reduced or incomplete caulonema differentiation, defective bud development, and defects in cytokinesis.

Materials and Methods

Design of Artificial MicroRNAs (*PpRGTA1*, *PpRGTB1*, *PpRGTB2*, and *PpREP*)

The sequences of *Physcomitrium patens* genes were acquired from JGI Phytozome (Goodstein et al., 2012). All oligonucleotides for artificial miRNAs (amiRNAs) were designed to target Rab-GGT components (Table 2-1) using Web MicroRNA Designer (WMD3, http://wmd3.weigelworld.org/) and they were used as PCR primers. Primer sequences are listed in Table 2-2. Then, the amiRNAs was cloned into the RS300 plasmid (Figure 2-1) containing the *Arabidopsis* precursor miR319a by site-directed mutagenesis using PCR. amiRNAs primers of 4 oligonucleotide sequences and forward & reverse primers (Forward: A #339/ Reverse: B #389) used pRS300 as template and substituted the miRNA-miRNA duplex by overlapping PCR (Schwab et al., 2006).

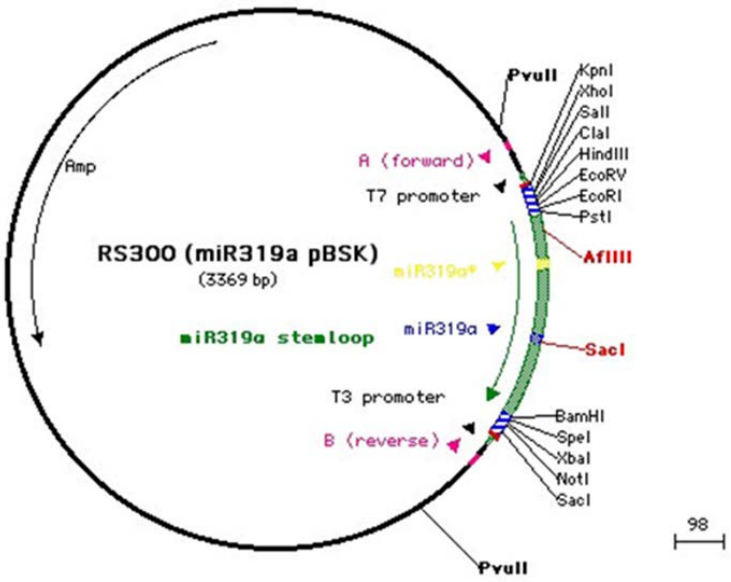

Figure 2-1: Map of pRS300 (Schwab et al., 2006).

Table 2-1

List of WMD3 ID used for designing amiRNA.

Target (Accession No)	WMD3 ID
RGTA1 (Pp1s139_38V6.1)	TC9807
RGTB1 (Pp1s163_87V6.1)	TC5971
RGTB2 (Pp1s34_430V6.2)	TC3414
REP (Pp1s155_53V6.1)	NP13141152

Table 2-2

List of primers used for constructing amiRNA.

Primers	Sequence
pRS300 (miR319a pBSK)-F #339 (A)	caccAGCTTGATATCGAATTCCTG
pRS300 (miR319a pBSK)-R #389 (B)	GCTCTAGAACTAGTGGATCCCCC
RGTA1 I miR-s	gaTCTGTAATTAATCTAGTCCCGtctctcttttgtattcc
RGTA1 II miR-a	gaCGGGACTAGATTAATTACAGAtcaaagagaatcaatga
RGTA1 III miR*s	gaCGAGACTAGATTATTTACAGTtcacaggtcgtgatatg
RGTA1 IV miR*a	gaACTGTAAATAATCTAGTCTCGtctacatatatattcct
RGTB1 I miR-s	gaTTAAGCCACGTGCTTATGCAAtctctcttttgtattcc
RGTB1 II miR-a	gaTTGCATAAGCACGTGGCTTAAtcaaagagaatcaatga
RGTB1 III miR*s	gaTTACATAAGCACGAGGCTTATtcacaggtcgtgatatg
RGTB1 IV miR*a	gaATAAGCCTCGTGCTTATGTAAtctacatatatattcct

RGTB2 I miR-s	gaTACATGAATGAATGGCCGCGCtctctcttttgtattcc
RGTB2 II miR-a	gaGCGCGGCCATTCATTCATGTAtcaaagagaatcaatga
RGTB2 III miR*s	gaGCACGGCCATTCAATCATGTTtcacaggtcgtgatatg
RGTB2 IV miR*a	gaAACATGATTGAATGGCCGTGCtctacatatatattcct
REP I miR-s	gaTACTTTCGTATGGAACTGCGGtctctcttttgtattcc
REP II miR-a	gaCCGCAGTTCCATACGAAAGTAtcaaagagaatcaatga
REP III miR*s	gaCCACAGTTCCATAGGAAAGTTtcacaggtcgtgatatg
REP IV miR*a	gaAACTTTCCTATGGAACTGTGGtctacatatatattcct

EX Taq PCR

Standard PCR was performed in 15 µl reactions containing 10X Ex-Taq buffer, 2.5 mM dNTP, 10 µM of each primer dilution, Ex Taq polymerase (cat no: RR001A, Takara BioUSA, Inc), 24 ng/µl pRS300 plasmid, and nuclease-free water. The PCR cycling protocol consisted of a gel electrophoresis analysis running 1 µL on a 1% agarose gel with ethidium bromide at 100V for 40 min. Once the presence and the size of the product were confirmed, EtOH purification was performed with 5 M NaCl, cooled 100% EtOH and deionized water.

KOD PCR (proofreading activity and high rates of elongation)

The amplified fragments were agarose-gel extracted using QIAquick® Gel Extraction Kit (cat no: 28704 and 28706, QIAGEN). KOD PCR was performed to fuse the 3 amiRNA fragments to create the amiRNA template constructs. PCR amplification was performed in 15 µl reactions containing 10X KOD buffer, 2 mM dNTP, MgSO4, MIR319a 10 µM forward and reverse primers, KOD Hot Start DNA Polymerase (cat no: 71086-5,

MilliporeSigma) and nuclease-free water. The PCR cycling protocol consisted of an initial denaturation at 95°C for 3 min, followed by 30 cycles of 95°C for 20 sec, 55°C for 20 sec, and 68°C for 30 sec, and a final extension at 68°C for 10 min. The product was held at 4°C at the end of the cycle. The fragment sizes of the KOD-amplified product were assessed by gel electrophoresis running 1 µL on a 1% agarose gel with ethidium bromide at 100 V for 40 min. Once the presence and the size of the product were confirmed, EtOH purification was performed with 5 M NaCl, cooled 100% EtOH, and deionized water.

TOPO Cloning (Check insert by sequencing)

Ethanol-purified KOD-amplified product was diluted to make 5~20 ng/µL concentration. Topo cloning was performed in 1.5 µl reaction containing salt (200 mM NaCl, 10 mM MgCl2), nucleus-free water, pENTR/D-TOPO (cat no: K243520, Invitrogen; Figure 2-2), which is used as an entry vector, and the diluted PCR products. The pENTR/D-TOPO plasmid with our gene of interests was transformed into NEB® 5-alpha Competent *E.coli* (DH5α) prepared by the protocol from the OpenWetWare website (https://openwetware.org/wiki/Preparing_chemically_competent_cells). For selection of positive transformants, the *E.coli* cells were plated on LB agar plates containing kanamycin (50 µg/ml) and grown at 37°C overnight. Primer sequences used for insertion check are indicated in Table 2-3.

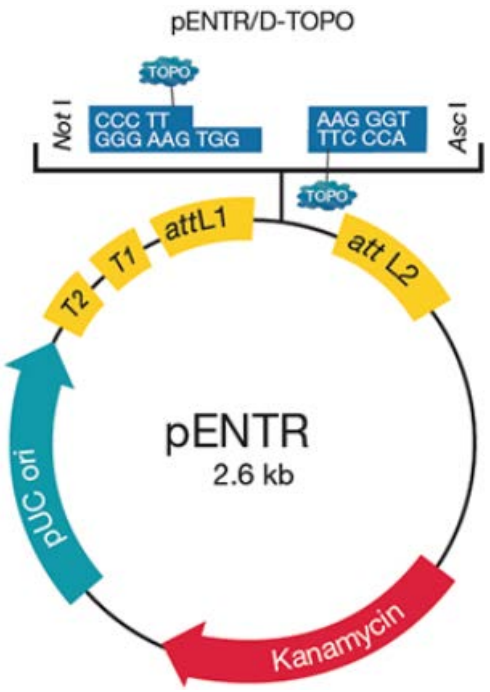

Figure 2-2: pENTR/D-TOPO for TOPO cloning (Invitrogen).

Table 2-3

List of primers used for sequencing.

Primers	Sequence
pENTR (M13)-F #304	TGTAAAACGACGGCCAGT
pENTR (M13)-R #305	CAGGAAACAGCTATGACCA

Colony PCR

For determining the presence or absence of the DNA fragment of interest in the pENTR/D-TOPO plasmid (backbone size w/o insert: 2580 bp), portions of each individual colony were added directly to the PCR reaction and lysed during the initial heating step, causing the release of the plasmid DNA from the cell. The released plasmid DNA was served as template for the amplification reaction and the insert DNA was

confirmed by the specific primers (Forward: pENTR #304; Table 2-3/ Reverse: pRS300 #389; Table 2-2). The colony PCR amplification was performed in a 10 µl reaction containing 10X Ex-Taq buffer, 2.5 mM dNTP, 10 µM of each primer dilution, Ex Taq polymerase and nuclease-free water. The PCR cycling protocol consisted of an initial denaturation at 94°C for 3 min, followed by 33 cycles of 94°C for 30 sec, 55°C for 30 sec, and 55°C for 1 minute 30 sec, and a final extension at 72°C for 10 min. The product was held at 4°C at the end of the cycle. The sizes of the insert DNA were determined by gel electrophoresis running 1 µL on a 1% agarose gel with ethidium bromide at 100 V for 40 min.

Plasmid Extraction and Digestion

All positive colonies with the insert of interest were selected and grown in LB liquid medium containing kanamycin (50 µg/ml) at 37°C overnight. The plasmids containing the insert of interest, designed amiRNA, were extracted using E.Z.N.A.® Plasmid Mini Kit I (SKU: D6942-01, Omegabiotek). Extracted plasmids containing the amiRNA construct were double digested using restriction enzymes EcoRI and BamHI from New England BioLabs. Gel electrophoresis was used to confirm the size of the amiRNA constructs.

Sequencing amiRNA Construct

The amiRNA constructs were confirmed again by Sanger DNA sequencing (Eurofins Inc, Louisville, KY, USA).

Gateway LR Reaction (Cloning amiRNA precursor into estradiol inducible vector pGX8)

LR reaction was mediated by Gateway® LR Clonase® II enzyme mix (Invitrogen) which catalyzes the *in vitro* recombination between an entry clone pENTR (Figure 2-2) and a destination vector pPGX8 (provided by Dr. Hasebe Mitsuyasu of NIBB, Japan; Figure 2-3). Rab-GGT amiRNA fragments flanked by attL sites in pENTR were cloned into Gateway reading frame cassette in pPGX8 containing attR sites to generate an expression clone.

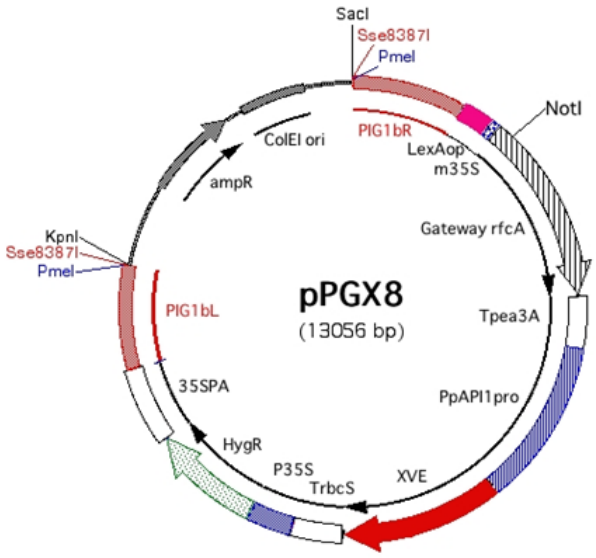

Figure 2-3: β-estradiol inducible vector, pPGX8 (Kubo et al., 2013).

Confirmation of The Insert by Restriction Digestion and Linearization Before Moss Transformation

Restriction digestion was conducted according to manufacturer's instructions (New England BioLabs, http://www.neb.com) to verify the presence of the Rab-GGT amiRNA fragment in the pPGX8. Gel electrophoresis was performed to visualize the result of digest and examine the size of the digest fragments. The insert was confirmed again by DNA sequencing (Eurofins Inc, Louisville, KY, USA). The confirmed pPGX8 containing

the correct insert was linearized using PmeI or Sse8387I restriction enzyme and the linearization was confirmed by gel electrophoresis.

Plant Culture Conditions and Maintenance

The moss *Physcomitrium patens* was propagated on BCDAT agar medium under continuous white light at 50 μmol m^{-2} s^{-1} intensity at 25℃ (Thole et al., 2014). For maintenance, subculture was routinely carried out at an interval of 15 days. *P. patens* tissue was blended with 5 ml of autoclaved deionized water using a Polytron homogenizer (T20B.S1, IKA) and distributed onto BCDAT medium overlain with cellophane disks (Cove et al., 2009). For long-term storage, tissue was maintained on BCDAT medium in screw capped tube sealed with parafilm and stored at 10℃.

Moss Transformation Using Polyethylene glycol (PEG) Mediated System

The moss *P. patens* protoplasts were isolated and the linearized PGX8 plasmid containing the amiRNA construct was introduced into the protoplasts using PEG-mediated DNA uptake according to the protocol described by Yuji Hiwatashi and Mitsuyasu Hasebe (http://www.nibb.ac.jp/evodevo/PHYSCOmanual/9.1_180418.htm). Protoplasts mixed with PRM/T (protoplast regeneration medium for the top layer) were regenerated on a cellophane membrane overlaying a PRM/B (protoplast regeneration medium for the bottom layer) plate at 25°C under continuous white light for 10 days. A representative image of protoplast regeneration is shown in Figure 2-4. For selection, hygromycin B (Invitrogen) was used at the final concentration of 30 μg/l in the BCDAT medium. After 10 days, protoplasts grown on the cellophane were transferred all together by lifting the cellophane to a hygromycin B/BCDAT plate. After the first selection period

of 3~4 weeks, each surviving colony was transferred to an antibiotic-free BCDAT plate and incubated for 1 week. After 1 week, a small part of each protonemal colony was transferred again to a selection medium and incubated for 1 week. After the second selection period, candidate stabled positive transformants were isolated.

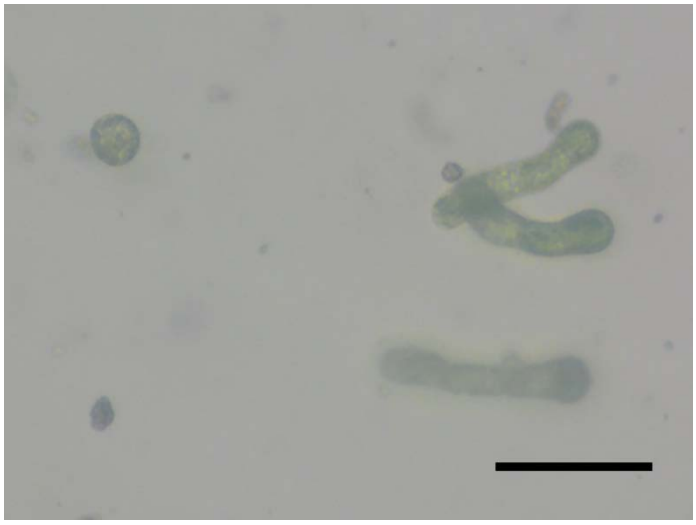

Figure 2-4: Protoplast regeneration, Bar = 100 µm.

Confirmation of Knockdown Lines Harboring amiRNA Constructs by Genomic DNA Extraction and PCR Screen

Genomic DNA was extracted from 7-day-old positive transformants using the IBI plant isolate DNA extraction kit (IBI Scientific) or DNA extraction buffer (stock 10 ml; 1 M Tris-HCL [pH 7.5, 2 ml], 5 M NaCl [0.5 ml], 0.5 M EDTA [pH 8.0, 0.5 ml], 10% SDS [0.5 ml], water [6.5 ml]) and confirmed by PCR using amiRNA construct specific primers (Forward: A #339/ Reverse: B #389).

β-estradiol Treatment

β-estradiol (E8875-1G, Sigma-Aldrich) was dissolved to 10 mM in dimethyl sulfoxide (DMSO) (D8779, Sigma-Aldrich) and stored at -20°C. 10 mM stock solution was diluted to 1 μM with BCDAT medium and poured into plates and stored at 4°C. Knockdown lines were incubated under continuous white light at 25°C for induction.

Sample Preparation for RNA Extraction

Rab-GGT knockdown lines were subcultured twice using a Polytron homogenizer (T20B.S1, IKA) and grown on a cellophane membrane overlaying a BCDAT plate for 5 days. For induction of knockdown, the plants grown on the cellophane were transferred all together by lifting the cellophane to a 1 μM β-estradiol plate. After 5~7 days incubation, around 100 mg of plant sample was collected and the water was removed from the collected sample using a pipet. The dehydrated sample was frozen immediately in liquid nitrogen to prevent RNA degradation and stored at -80°C for further use in RNA extraction.

RNA Extraction and Reverse Transcription

Total RNA was extracted from the frozen Rab-GGT knockdown lines stored at -80°C using the Qiagen RNeasy mini kit (cat no: 74134, QIAGEN). cDNA was synthesized from 0.5 μg of extracted RNA using the ImProm-II™ Reverse Transcription System (cat no: A3800, Promega) following the kit's instructions. All synthesized cDNAs were stored at -20°C.

Semi-Quantitative RT-PCR

For Reverse transcription PCR, primers specific to GapC1 (Forward #403: TGCCATTAAGACGGCTATCA/ Reverse #404: CGAGATTATTTCCAACAGATGGTCTA) as an internal control and primers specific to Rab-GGT components were used. The RT-PCR was performed in 10 µl reaction containing 10X Ex-Taq buffer, 2.5 mM dNTP, 10 µM each primer, Ex Taq polymerase, nuclease-free water and 1/10 diluted template cDNA (around 200 ng/µl). The amplification system consisted of an initial denaturation of 3 min at 94°C, followed by 30 sec at 94°C, 30 sec at 55°C, and 1min 30 sec at 72°C for 30 cycles, and a final extension of 5 min at 72°C. The product was held at 4°C at the end of the cycle. PCR products were visualized and assessed by gel electrophoresis on a 1% agarose gel with ethidium bromide at 100 V for 40 min.

Quantitative Real-time Polymerase Chain Reaction (qRT-PCR)

All oligonucleotides specific to a specific target sequence were designed using Primer3 (Rozen & Skaletsky, 2000, https://bioinfo.ut.ee/primer3-0.4.0/) for use in a SYBR™ Green-based qRT-PCR. For internal control, primers specific to adenine phosphoribosyltransferase (Ade PRT, Phypa_443007) were used to equalize the amounts of cDNA from the different sources (Le Bail et al., 2013). Primer sequences are indicated in Table 2-4. qRT-PCR was performed in 10 µl reactions containing a SYBR™ Green (cat no: 4367659, Applied Biosystems), 2.5 µM of each primer, cDNA and nuclease-free water for 3 reactions per DNA sample. The 96 well thermocycler (QuantStudio™ 3, Applied Biosystems) was programmed to run for 10 min at 95°C, followed by 40 cycles of 15 sec at 95°C and 1 min at 60°C, and ending with a melting curve analysis. Endogenous control primers (Ade PRT) and PCR primers for each DNA sample were run

together on the same plate. Three sets of experimental replicates were performed. Quantification was based on the comparative Ct method.

Table 2-4

List of primers used for qRT-PCR.

Primers	Sequence
Ade PRT-F (Phypa_443007)	AGTATAGTCTAGAGTATGGTACCG
Ade PRT-R (Phypa_443007)	TAGCAATTTGATGGCAGCTC
RGTA1-F	CGACTTTGCCTGATTCGTCT
RGTA1-R	CCACCCTCTTTCTCCCTCTC
RGTB1-F	ACCCGCACATCCTCTATACG
RGTB1-R	ACAGCATCAACCCTGTCAAA
RGTB2-F	GAGGAAACCATCAGCACGA
RGTB2-R	CCTGTCAAACAATGCCAGAA
REP-F	TATCTCTCTCCGTGGGCATC
REP-R	ATTTGGGCAAGTACCCTCCT

Transformation of Knockdown Lines with Cell Polarity Markers, T10G-YFP-*At*RabA4d

35s:eYFP-*At*RabA4d was obtained from Dr. Erik Nielsen lab (Szumlanski & Nielsen, 2009). For amplification of YFP-*At*RabA4d, KOD PCR was performed with GoTaq Green (Promega) using primers specific to YFP-*At*RabA4d (Table 2-5). The same procedure mentioned above (TOPO-cloning → Colony PCR → Plasmid extraction with

mini-prep → Plasmid digestion → Sequencing → LR reaction with pT10G → Restriction digestion checking → Linearization → Transformation into knockdown lines) was performed but using a constitutive expression vector pT10G (Figure 2-5) as a destination vector targeting a redundant copy of the PTA1 gene in *P. patens*, instead of pPGX8. Candidate positive transformants were isolated using zeocin (Alfa Aesar) at the final concentration of 100 μg/l in the BCDAT medium and kept on an antibiotic-free BCDAT plate.

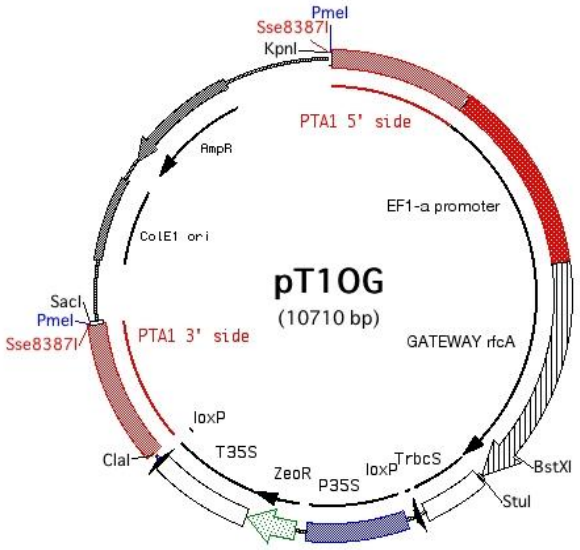

Figure 2-5: Constitutive expression vector, pT10G (Aoyama et al., 2012).

Table 2-5

List of primers used to amplify YFP-AtRabA4d.

Primers	Sequence
eYFP-*At*RabA4d-F	CACCATGGTGAGCAAGGGCGAGG
eYFP-*At*RabA4d-R	TTACGATTTGCCGCAACATCC

Immunostaining for Observation of Actin and Microtubules

Homogenized WT and Rab-GGT knockdown lines grown on BCDAT medium supplemented with or without 1 μM β-estradiol for 7 days were used for the immunostaining experiment according to the procedures of Yoshikatsu Sato and Takashi Murata (http://www.nibb.ac.jp/evodevo/PHYSCOmanual/3.8.htm). Briefly, protonema cells were fixed in fixation solution containing 8% (w/v) paraformaldehyde, 1× PME (0.2 M PIPES-NaOH [pH 6.8], 5 mM EGTA [pH 8.0], and 2 mM $MgCl_2$), 0.01% (v/v) Nonidet P-40, and 1% (v/v) DMSO for 60 min. Then the samples were rinsed with PMEN0.01(PME supplemented with 0.01% (v/v) Nonidet P-40) and attached to 0.1% PEI (polyethyleneimine)-coated coverslip. All experiments were performed on a 24-well tissue culture plate (Mark II tissue culture clusters, 16 mm well diameter, cat no: 3424, Costar) until the step of attaching to the coverslip. The attached samples were treated with a driselase solution containing 2% (w/v) driselase, 1× proteinase inhibitor (cOmplete™ Protease Inhibitor Cocktail; cat no: 046931160001, Roche Diagnostics), 5 mM EGTA [pH 8.0], and 0.4 M mannitol for 10 min at room temperature and then rinsed with PMEN0.01. The samples were soaked in cold methanol for 10 min at -20°C and rinsed with PMEN0.01. Then the samples were permeabilized and blocked with 0.05% (v/v) Triton X-100 and 0.05% (w/v) BSA for 10 min and rinsed with PBS. For α-tubulin staining, the samples were labeled with Mouse monoclonal anti-α-tubulin antibody (cat no: T9026, Sigma-Aldrich) at a dilution of 1:100 in PBS overnight at 4°C. Then the samples were rinsed with PBS and labeled with Goat anti-mouse IgG cross-absorbed secondary antibody Alexa Fluor™ 546 (cat no: A11003, Invitrogen) for 3 h at 37°C.

After rinsing with PBS, the samples were stained with 0.2 μg/ml DAPI for 10 min for nuclei visualization and rinsed with PBS. Finally, the samples were mounted on a glass microscope slide with a ProLong™ Diamond Antifade Mountant (cat no: P36961, Invitrogen) and sealed with clear nail polish. The samples were stored in the dark at room temperature. For F-actin staining, the same procedure was performed using Acti-stain™ 488 phalloidin (cat no: PHDG1, Cytoskeleton, Inc.).

Microscopy

The morphology of *P. patens* was studied using a Nikon Digital Slight DS-Fi1 camera mounted on a Nikon inverted brightfield microscope (Eclipse TE-200) or a Nikon stereomicroscope (SMZ1500) with a Nikon digital slight DS-U3 camera controller. A Nikon Super High Pressure Mercury Lamp Power Supply (HB-10103AF) was used for fluorescence applications in microscopy such as calcofluor white stained *P. patens* and visualization of cell polarity markers T10G-YFP-*At* RabA4. Time-lapse images of YFP-*At*RabA4d were taken every 20 sec using a Nikon A1 confocal microscope with a 40× objective (1.30 NA) with a 525 nm (GFP) emission filter. Cytoskeleton image acquisition was performed with a Nikon A1 confocal microscope with a 60× objective (1.40 NA) and 450 nm (DAPi), 525 nm (GFP) emission filters for F-actin, and with a 100×/1.45 Oil objective (Nikon CFI Plan Apochromat λ) and 450 nm (DAPi), 595 nm (TxRed) emission filters for microtubules.

Phenotype Analysis

BCDAT medium was routinely used for tissue maintenance and propagation, but for observation of protruding caulonemal filaments and gametophores, ammonium tartrate-

free BCD medium was used. For longer period of induction on medium, the plate was sealed with surgical tape and parafilm to prevent evaporation of water.

Statistical Analysis

Statistical analysis was performed using GraphPad Prism version 9.3.1 for Windows (GraphPad Software, San Diego, California USA, www.graphpad.com). The P-values were obtained with one-way or two-way analysis of variance (ANOVA) and GP P value style was used: 0.1234 (ns), 0.0332 (*), 0.0021 (**), 0.0002 (***), < 0.0001 (****).

Results and discussion

Generation of Rab-GGT knockdown lines and confirmation of an inducible RNAi system mediated by β-estradiol

Four *P. patens* Rab-GGT knockdown (KD) lines, *PpRGTA1* KD, *PpRGTB1* KD in *rgtb2* knockout background (KO), *PpRGTB2* KD in *rgtb1* KO, and *PpREP* KD were generated using the β-estradiol-dependent inducible RNAi system developed by Kubo et al. (2013). The generation of the single *rgtb1* KO and *rgtb2* KO lines were previously described (Thole et al., 2014). This system is mediated by an estrogen receptor-based transcriptional activator XVE, which attaches to the LexA operator upon β-estradiol induction and aids in the recruitment of RNA polymerase II to the cauliflower mosaic virus (CaMV) minimal 35S promoter (Pm35S) to induce expression of the downstream gene, introduced with the Gateway system (Zuo et al., 2000; Kubo et al., 2013). This *P. patens* XVE system allowed modulation of the induction level by controlling the β-estradiol concentration from 0.001 μM to 1 μM, and a longer maximal gene expression

period for at least 7 days, without causing any noticeable morphological or growth defects (Kubo et al., 2013). The amiRNA constructs confirmed by DNA sequencing (Eurofins Inc, Louisville, KY, USA) were cloned into the Gateway reading frame cassette in pPGX8, which were then used for conventional PEG-mediated protoplast transformation. After a repeated series of independent transformations, whether resistant transformed moss lines carry amiRNA constructs targeting each gene was identified by genotyping of extracted DNA samples. Through Ex Taq PCR using gene-specific primers (Forward: A #339/ Reverse: B #389) and agarose gel electrophoresis analysis, it was confirmed that all four lines displayed a band at the desired size of 459 bp (Figure 2-6).

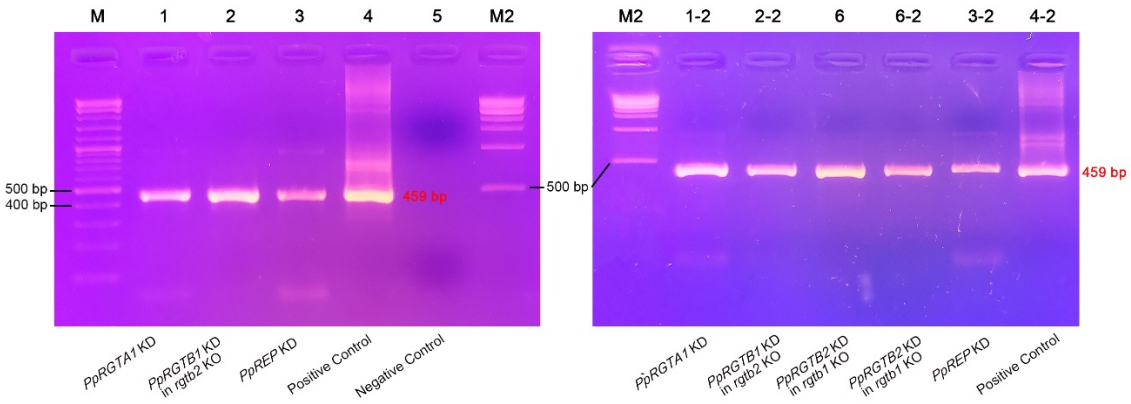

Figure 2-6: Genotyping of Rab-GGT knockdown lines for amiRNA inserts.

Lane M showing 2-log DNA ladder, Lane M2 showing l kb ladder, Lane 1, 1-2 (*PpRGTA1* KD), 2, 2-2 (*PpRGTB1* KD in *rgtb2* KO), 3, 3-2 (*PpRGTB2* KD in *rgtb1* KO), & 6, 6-2 (*PpREP* KD) showing the 459 bp amplified PCR product of amiRNA gene. Lane 4, 4-2 & 5 showing positive (pPGX8 plasmid containing amiRNA construct) & negative control, respectively.

The knockdown levels in confirmed KD lines were validated by quantitative real-time PCR. Five candidate internal controls known as stable expressed reference genes in *P. patens* described in Le Bail et al. (2013) and Khraiwesh et al. (2015) were tested with WT samples with or without β-estradiol induction. The adenine phosphoribosyl transferase (AdePRT) showing the least difference in Ct values between the two was selected to normalize samples with different endogenous quantities (Figure 2-7A). Extracted RNA from all four KD mutants were tested in triplicate, and all showed a decrease in fold change indicating reduced gene expression, with approximately 66% in *PpRGTA1* KD, 46% in *PpRGTB1* KD in *rgtb2* KO, 86% in *PpRGTB2* KD in *rgtb1* KO, and 71% in *PpREP* KD compared to WT control sample, and 67% in *PpRGTA1* KD, 62% in *PpRGTB1* KD in rgtb2 KO, 89% in *PpRGTB2* KD in rgtb1 KO, and 76% in *PpREP* KD compared to un-induced KD lines (Figure 2-7B).

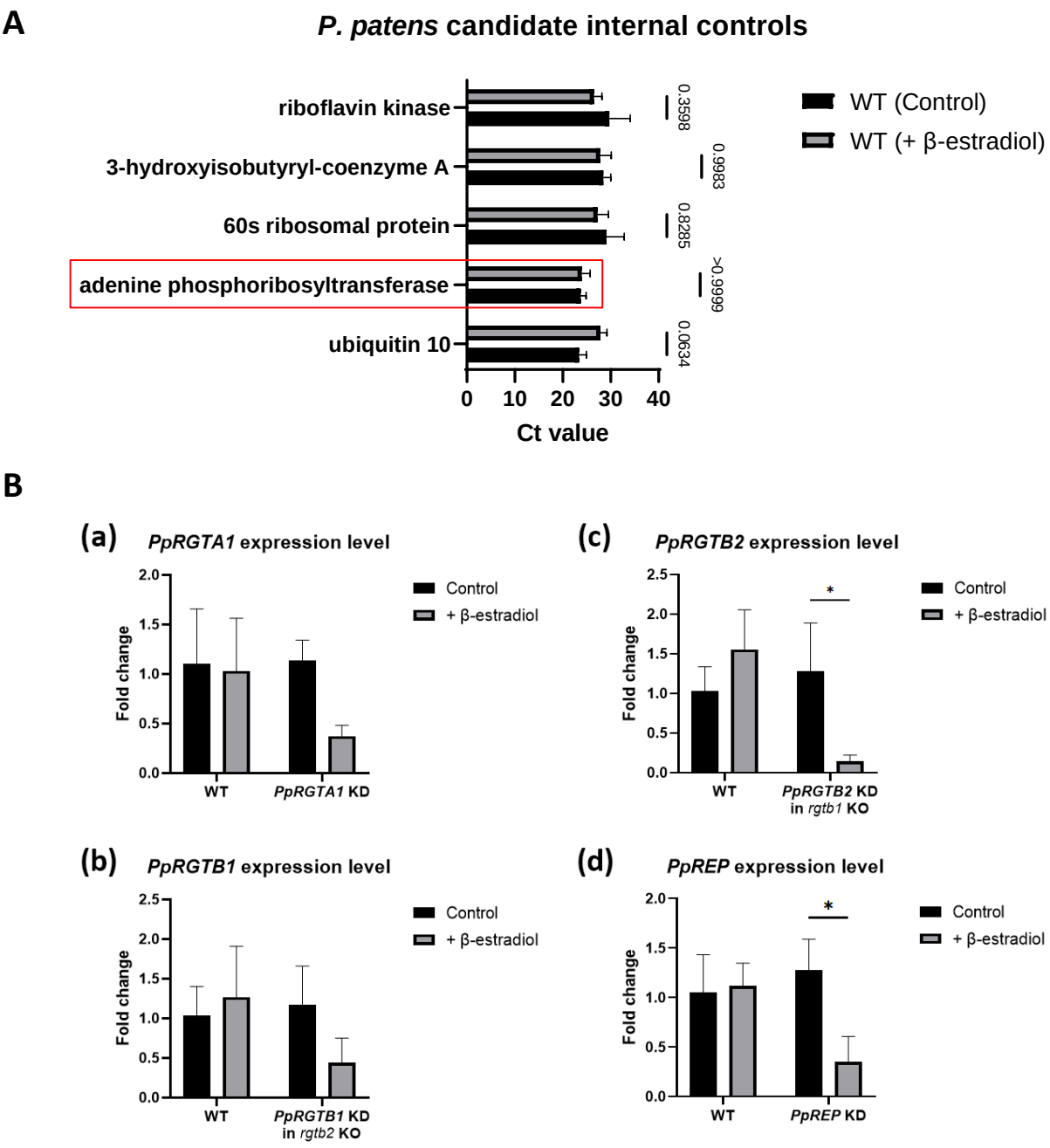

Figure 2-7: qRT-PCR analysis to quantify relative expression levels of *PpRGTA1*, *PpRGTB1*, *PpRGTB2*, and *PpREP* with or without β-estradiol induction.

(A) Mean Ct value ± SD representing expression levels of candidate internal controls in *P. patens* WT with or without β-estradiol induction based on the analysis of three or more

independent experiments. (B) Data represent the mean ± SD of three independent experiments after normalization with the picked internal control gene *PpAdePRT*.

Phenotypes of *P. patens* Rab-GGT knockdown lines

P. patens forms protonema composed of two cell types: shorter, slow-growing chloronemal cells that are rich in chloroplasts and perform a photosynthetic function, and longer, fast-growing caulonemal cells that contain fewer chloroplasts and are involved in terrestrial colonization (spread of the moss colony) (Cove & Knight, 1993; Cove et al., 2006; Prigge & Bezanilla, 2010). To examine the effects of partial loss of Rab-GGT on the moss, the morphology of protonema was observed after 10 days of β-estradiol induction. Unlike complete KO mutants of Rab-GGT, all four induced-KD lines remained viable and showed branched filamentous growth (Figure 2-8 c–f) like WT (Figure 2-8 a) and un-induced KD lines (Figure 2-8 b; collected from un-induced *PpRGTB1* KD in *rgtb2* lines). However, β-estradiol induction resulted in defects in cell morphology and development such as abnormal swelling cell growth in chloronemal tissue, and reduced or incomplete caulonema differentiation, presumably due to disrupted polarized tip growth; thus, the branched hairy appearance was much less prominent (Figure 2-8 c–f).

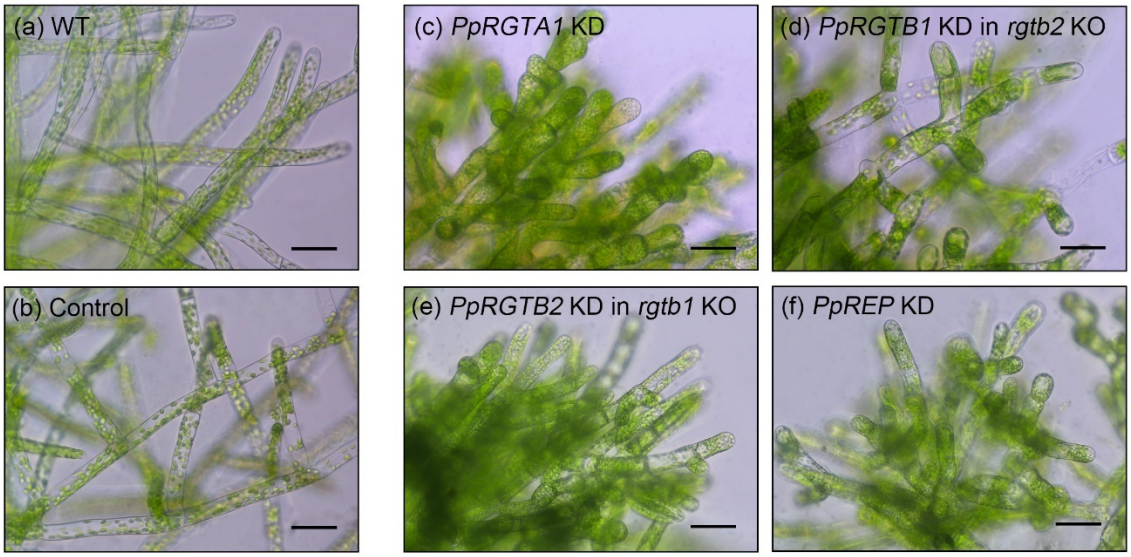

Figure 2-8: Phenotypes of WT and Rab-GGT knockdown lines.

Representative morphology of protonema in WT and Rab-GGT knockdown lines under control conditions (a and b), and four Rab-GGT knockdown lines under 1 μM β-estradiol induction (c–f). Scale bars = 50 μm.

The *P. patens* Rab-GGT knockdown lines show significantly reduced colony size

A fragment of tissue 1-2 mm in diameter, as uniform as possible, was placed on the BCDAT medium with or without β-estradiol. The average colony diameter of 10 individual colonies per strain was obtained after 7 and 14 days. After induction by 1 μM β-estradiol, growth of all lines including the WT was delayed overall, and the colony size was smaller compared with the un-induced samples (Figure 2-9). The growth rates from day 7 to day 14 (Colony diameter at day 14 – day 7 / Colony diameter at day 7 × 100) were compared between β-estradiol induced and un-induced samples. In the control condition, the colony size of all samples was significantly increased by 120% in WT,

81% in *PpRGTA* KD, 99% in *PpRGTB1* KD in *rgtb2* KO, 99% in *PpRGTB2* KD in *rgtb1* KO, and 81% in *PpREP* KD (Both WT and all KD lines ****P < 0.0001). However, samples with β-estradiol induction, even WT, showed impeded growth compared to those without induction. WT, which increased by 120% when without induction, increased by 59% when with induction, but it was still significant (****P < 0.0001). In contrast, *PpRGTA* KD increased by only 6% (ns, P > 0.9999), *PpRGTB1* KD in *rgtb2* KO by 13% (ns, P = 0.9993), *PpRGTB2* KD in *rgtb1* KO by 15% (ns, P = 0.9995), and *PpREP* KD by 32% (ns, P = 0.4671), showing greatly delayed (no significant) growth. After 14 days, colony diameters of the β-estradiol-induced samples (Induced samples' colony diameter at day 14 / Un-induced samples' colony diameter at day 14 × 100) were 39% of that of the un-induced samples for WT, 32.1% for *PpRGTA* KD, 42% for *PpRGTB1* KD in *rgtb2* KO, 38.6% for *PpRGTB1* KD in *rgtb2* KO, and 43.5% for *PpREP* KD, resulting in significantly reduced colony size by β-estradiol treatment (Both WT and all KD lines ****P < 0.0001). Although colony growth in all samples, including WT, was inhibited by β-estradiol treatment itself, on day 7, WT differed insignificantly compared to all other KD lines (P = ns), but on day 14, the difference widened significantly (****P < 0.0001). Even without β-estradiol induction, all KD lines exhibited more delayed growth than WT at both day 7 and day 14 (****P < 0.0001), suggesting that there may be effects due to the basal level of transgene expression in the un-induced state (leaky expression) or the vector insertion. However, since no reduction of gene expression level was observed in the absence of β-estradiol, it is most likely due to reasons other than leaky expression. In the future, another possible variable, the effect of vector insertion, could be eliminated by transforming the samples with an empty pPGX8 vector and comparing the resulting

phenotype with that of the induced samples, demonstrating that the phenotype is the result of knockdown.

The smaller colony size in the mutants may be caused by defects in rapidly growing caulonemal cell differentiation and/or apical cell elongation. For more specific comparisons, cell morphology was examined under a Nikon inverted brightfield microscope (Figure 2-10A).

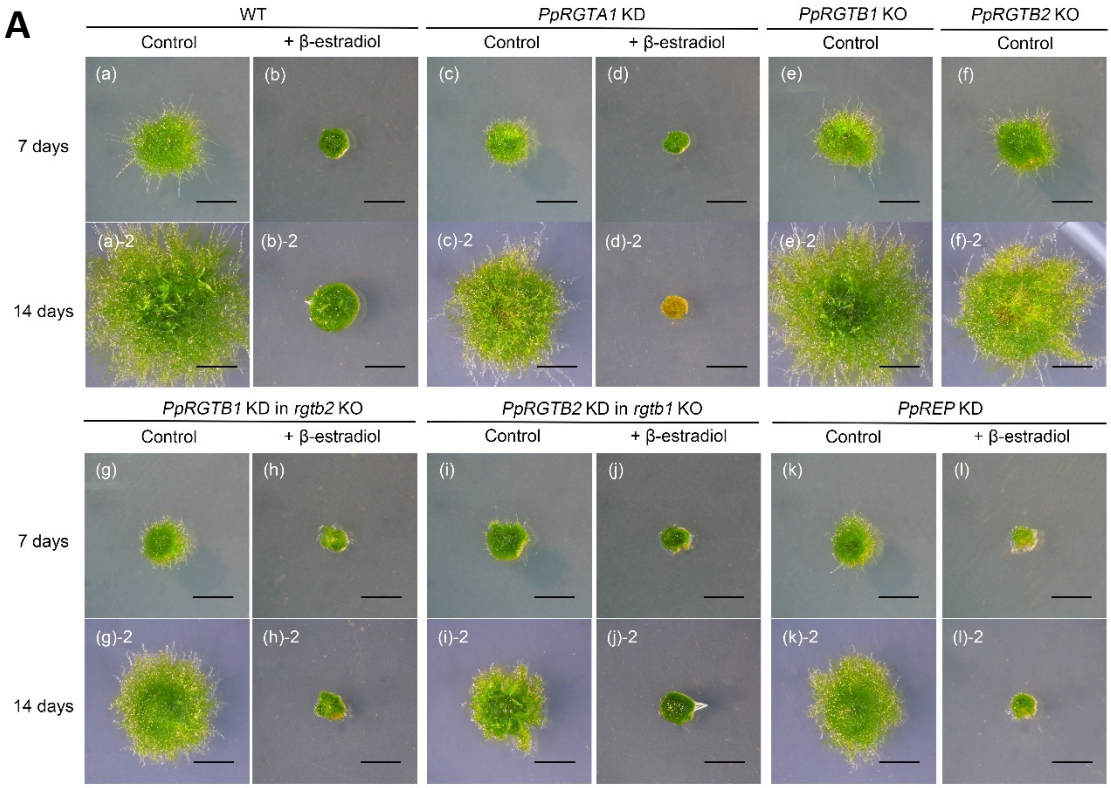

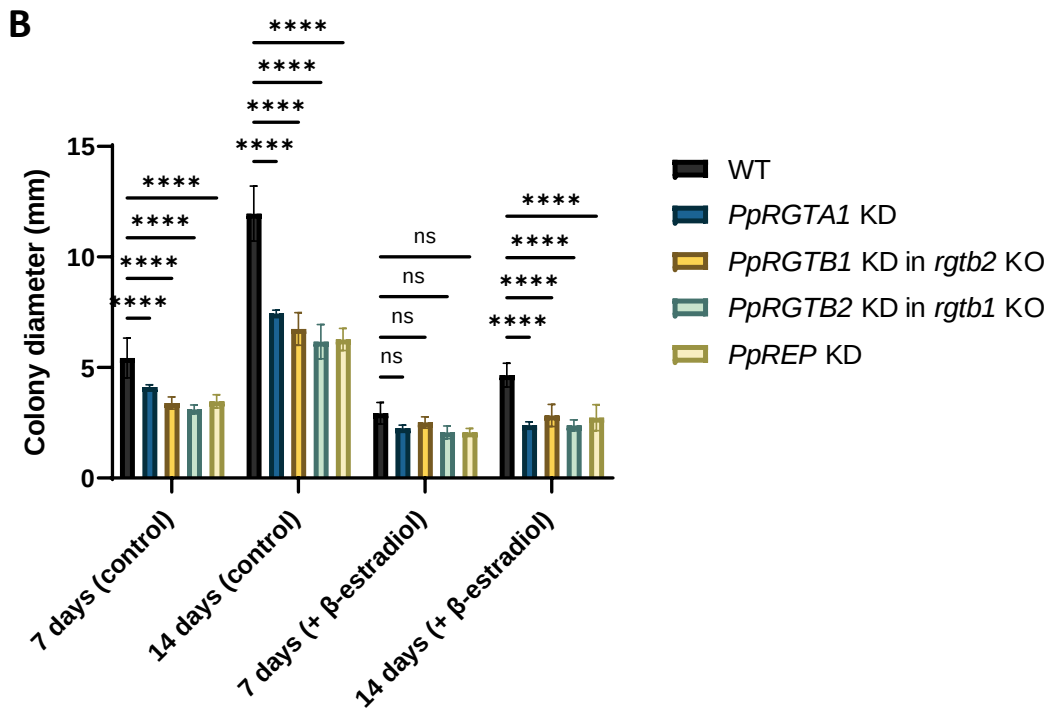

Figure 2-9: Colony morphology and average colony diameter of Rab-GGT knockdown lines with or without β-estradiol induction.

(A) Magnification of colonies of knockdown lines grown for 7 days (a–l) and 14 days (a-2–l-2) on BCDAT agar medium supplemented with 0.01% DMSO (a, c, e, f, g, i, and k, and -2) and 1 μM β-estradiol (b, d, h, j, and l, and -2). Scale bars = 5 mm. (B) Size of single colonies of each 7 and 14-days-old strain measured as diameter in millimeters. The data shown are the Mean ± SD of 10 individual colonies per line.

Chloronemal cells of the *P. patens* Rab-GGT knockdown lines are significantly shorter and thicker compared to the WT and display irregularly shaped cells with abnormal division pattern

In order to confirm that the phenotype of the KD lines is caused by reduced gene expression level and not by the inducer, we checked whether β-estradiol has an effect on cell morphological aspects in addition to delayed growth. For accurate measurement, the length and thickness of non-apical protonemal cells that have almost completed cell expansion after cell division were measured and only chloronema cells were used to eliminate the variable that can come from the different growth rates of the two protonemal cell types. The KD lines induced by β-estradiol for 10 days were stained by calcofluor-white, which binds with cellulose in cell walls of plants, and cell morphology was observed under UV light (Figure 2-10A a-3–l-3). Compared to un-induced lines (Figure 2-10A c, g, i, and k), induced KD lines (Figure 2-10A d, h, j, and l) showed cellular morphological defects, such as swollen chloronemal cells with shorter, bulged tips and reduced growth of caulonemal cells, due to reduced extension growth of the apical cell. Also, the aberrant orientation of the cell wall caused by abnormal division patterns was observed, as the obliquely oriented cell wall, characteristic of caulonema, was found in chloronema. Thus, the distinction of protonemal cell state was possible only through chloroplast mass (chloroplast-sparse cell, caulonema; chloroplast-rich cell, chloronema).

Before and after induction, WT decreased only 1% in cell size ($P > 0.9999$), but KD lines significantly decreased by 33.6% in RGTA1, 27.3% in RGTB1, 27.2% in RGTB2, and 30.4% in REP (all KD lines ****$P < 0.0001$) (Figure 2-10B). Also, some or most cells in KD lines expanded by diffuse (intercalary) growth, which made cells thicker than typical filamentous cells by cell wall expansion that occurs over large areas of the cell surface (Smith, 2003). In cell thickness, the Mean ± SD of WT before and after

induction was very similar, 13.74 ± 1.21 and 15.35 ± 2.33 respectively (P = 0.4965), but in KD lines, RGTA showed the greatest change with an increase of 81.45%, and RGTB1, RGTB2, and REP showed a 54.89%, 52.34%, and 27.67% increase as well (all KD lines $P \leq 0.0001$) (Figure 2-10C). These results show that β-estradiol only delays overall growth, but does not affect cell morphogenesis, thus indicating that these defects in cell morphology and elongation were induced by transient knockdown.

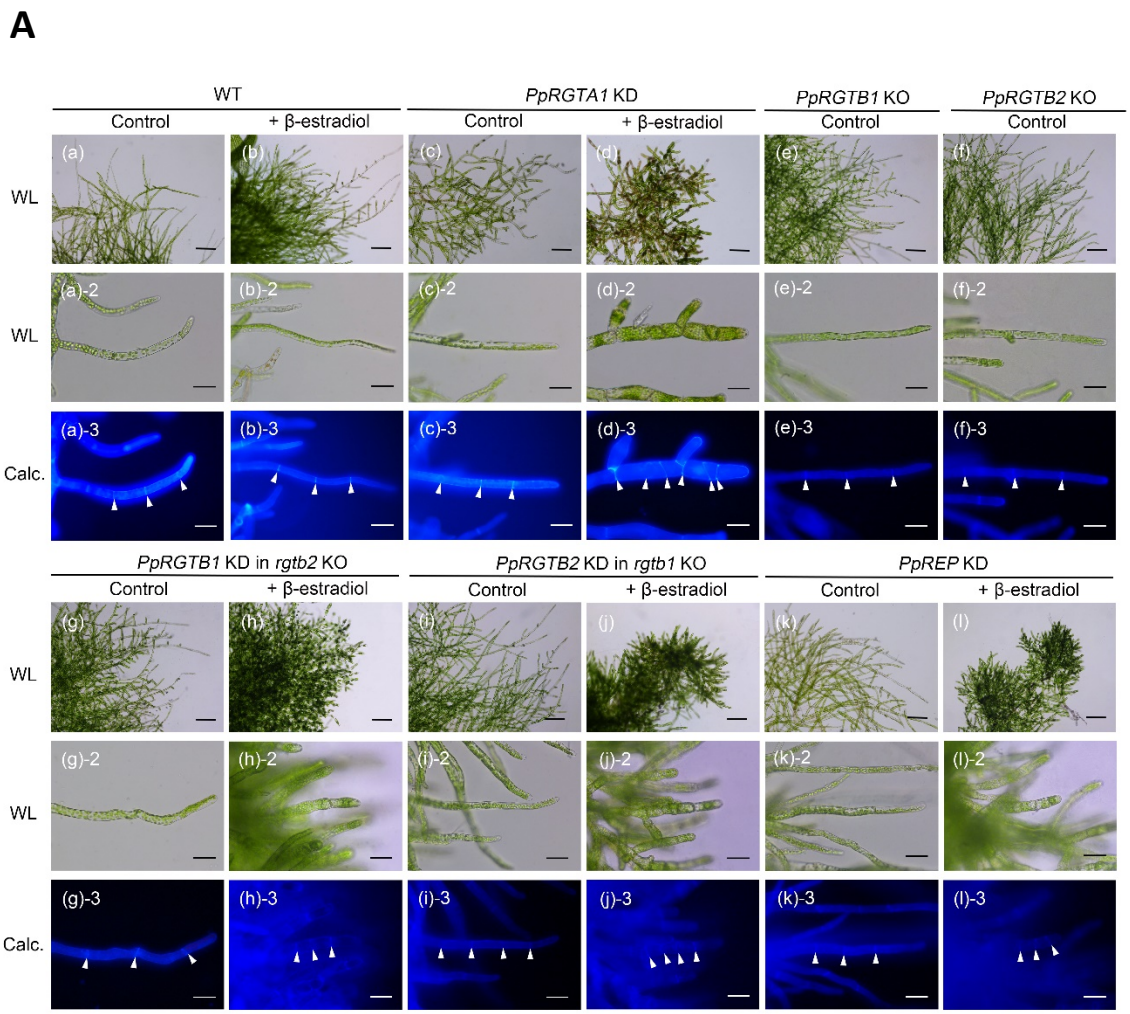

B

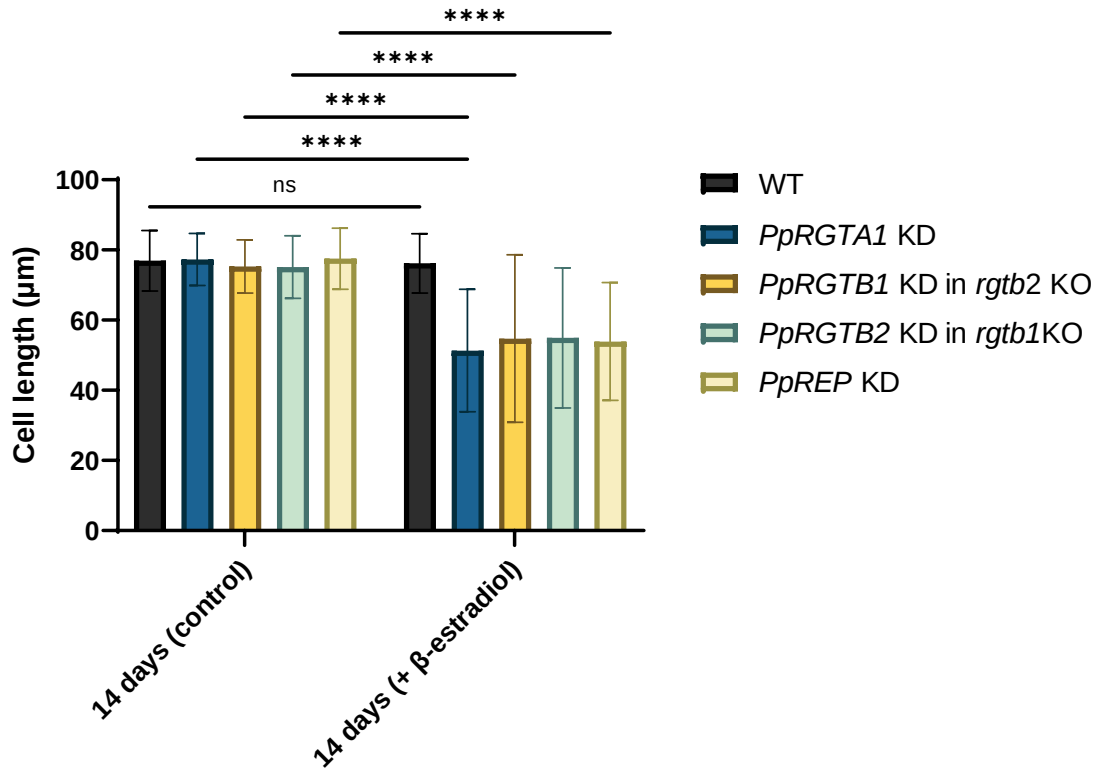
****
****
****
****
ns
Cell length (µm)
100
80
60
40
20
0
14 days (control)
14 days (+ β-estradiol)
WT
PpRGTA1 KD
PpRGTB1 KD in rgtb2 KO
PpRGTB2 KD in rgtb1KO
PpREP KD

C

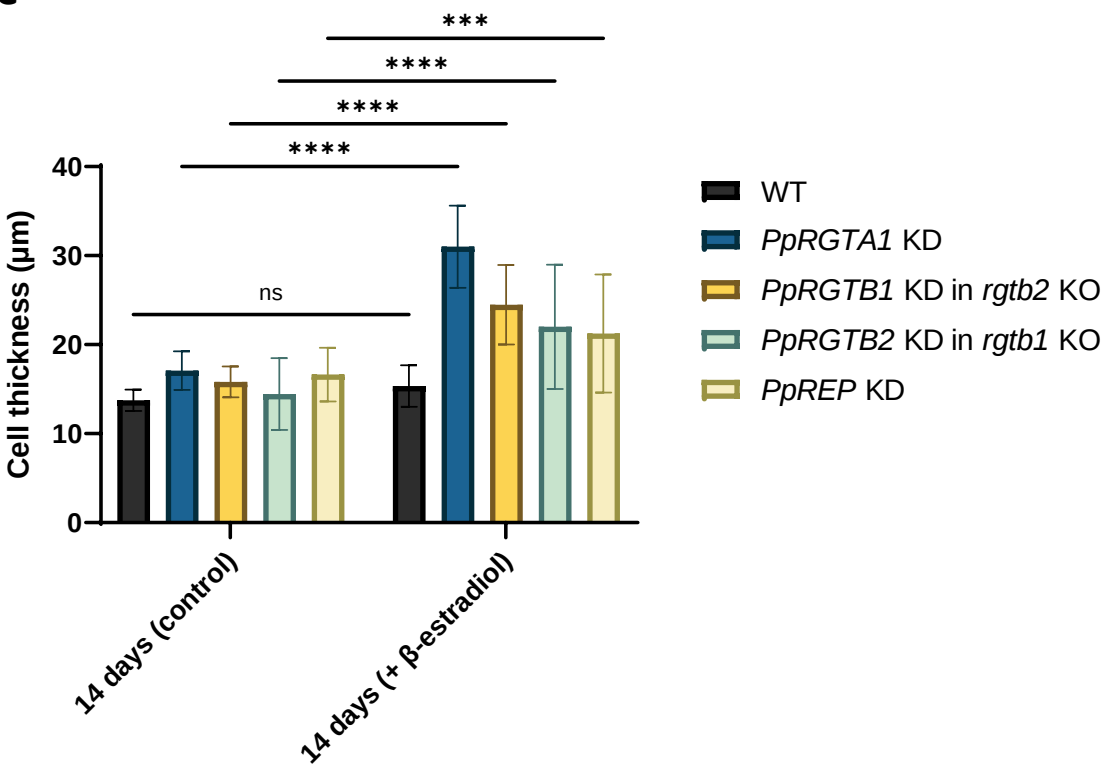
***
****
****
****
ns
Cell thickness (µm)
40
30
20
10
0
14 days (control)
14 days (+ β-estradiol)
WT
PpRGTA1 KD
PpRGTB1 KD in rgtb2 KO
PpRGTB2 KD in rgtb1 KO
PpREP KD

Figure 2-10: Filament & cell morphology and average cell length & thickness of chloronemal cells in the Rab-GGT knockdown lines with or without β-estradiol induction.

(A) Magnification of filament of WT and knockdown lines grown for 14 days on BCDAT agar medium supplemented with 0.01% DMSO (a, c, e, f, g, i, and k, -2, and -3) and 1 μM β-estradiol (b, d, h, j, and l, -2, and -3) under white light (WL) and UV light with calcofluor staining (Calc.). (a–l) Scale bars = 200 μm. (a-2–l-2 and a-3–l-3) Scale bars = 50 μm. (B) Size of single cells of each strain measured in micrometers. Data shown are Mean ± SD (n = 50). (C) Cell thickness of single cells of each strain measured in micrometers. Data shown are Mean ± SD (n = 30).

Caulonema and gametophore formation is strongly reduced in the *P. patens* Rab-GGT knockdown mutants

A fragment of tissue 1-2 mm in diameter was inoculated on ammonium tartrate-free BCD medium with or without β-estradiol. The average number of protruding caulonemal filaments for 6 individual colonies per line and the quantification of gametophores for 4 individual colonies per line were obtained after 30 days. Although protonemata grow slowly in BCD medium, protonemata differentiate into caulonemata earlier than BCDAT and the differentiation of chloronemata and caulonemata can be observed more easily in BCD medium than in other mediums. In addition, BCD medium is suitable for observation of bud formation and gametophores because the addition of ammonium (nitrogen source) to the medium promotes the growth of abnormal callus-like buds caused by irregular cell division at the young stage. This BCD medium is also used

for induction of sporophytes (PHYSCOmanual version 2.0, http://www.nibb.ac.jp/evodevo/PHYSCOmanual/3.1.htm). A few days after inoculation, the round colonies are mostly composed of chloronemata, and as the differentiation of chloronemata into caulonemata begins, caulonemal filaments protrude from the edge of the colony for expansion of the moss colony. Differentiated chloronemata and caulonemata are reprogrammed to form stem cells called side branch initial cells, which develop into secondary chloronema apical cells, caulonema apical cells, and gametophore apical cells, forming buds which become gametophores with stems, leaves and later reproductive organs (Cove & Knight, 1993).

The protruding caulonemal filaments of some KD lines were too short and fine to be observed with a dissecting microscope (Figure 2-11A b). Therefore, a brightfield microscope was used to observe the formation of caulonemata and count the number of them protruding from the colony edge. While more than 100 caulonemal filaments were observed in the WT and all un-induced KD lines, all induced KD lines displayed significantly shorter and reduced caulonema formation (****$P < 0.0001$) (Figure 2-11B).

In addition to the number of caulonemal filaments, the number and height of gametophores and the number of leaves per gametophore were determined to investigate whether disturbance of Rab-GGT function affects gametophore development with an extension of impaired protonema outgrowth (Figure 2-12). The induced *PpRGTA1* KD lines exhibited the most severe phenotypic deviation among all Rab-GGT KD mutants with the slowest growth rate, shortest and thickest chloronemal cells (Figure 2-10, B and C), and the fewest number of caulonemal filaments (Figure 2-11B). Despite partial loss of function through knockdown of gene expression, the viability of the *PpRGTA1* KD

lines began to be affected from approximately 10 days after induction, leading to loss of gametophore formation (Figure 2-12A c). Except the *PpRGTA1* KD lines, all other KD lines showed significant reduction in gametophore number and height (****P < 0.0001) (Figure 2-12, B and C) and leaves number per gametophore (*PpRGTB1* KD in *rgtb2* KO, **P = 0.0019; *PpRGTB1* KD in *rgtb2* KO, *P = 0.0159; *PpREP* KD, **P = 0.0011) (Figure 2-12D) compared to the WT. The length of rhizoids, hairy root-like structures which develop from base of the gametophores (Schaefer & Zrÿd, 2001), was also drastically shorter (Figure 2-12A a-3–f-3). This stunted gametophore phenotype of the *P. patens* Rab-GGT KD lines may be due to delayed induction of gametophore formation from protonemata, a slower growth rate of gametophores or a defect in the proliferation activity of gametophores to produce leaves and rhizoids. Taken together, diminished elongation of the chloronemal filaments by potentially affected tip growth leading to shorter and thicker cells and severe defects in differentiation of caulonema and rhizoids that expand by tip growth and gametophores that expand by diffuse growth suggest that Rab-GGT may play a vital role in both tip growth and diffuse growth in *P. patens*.

A

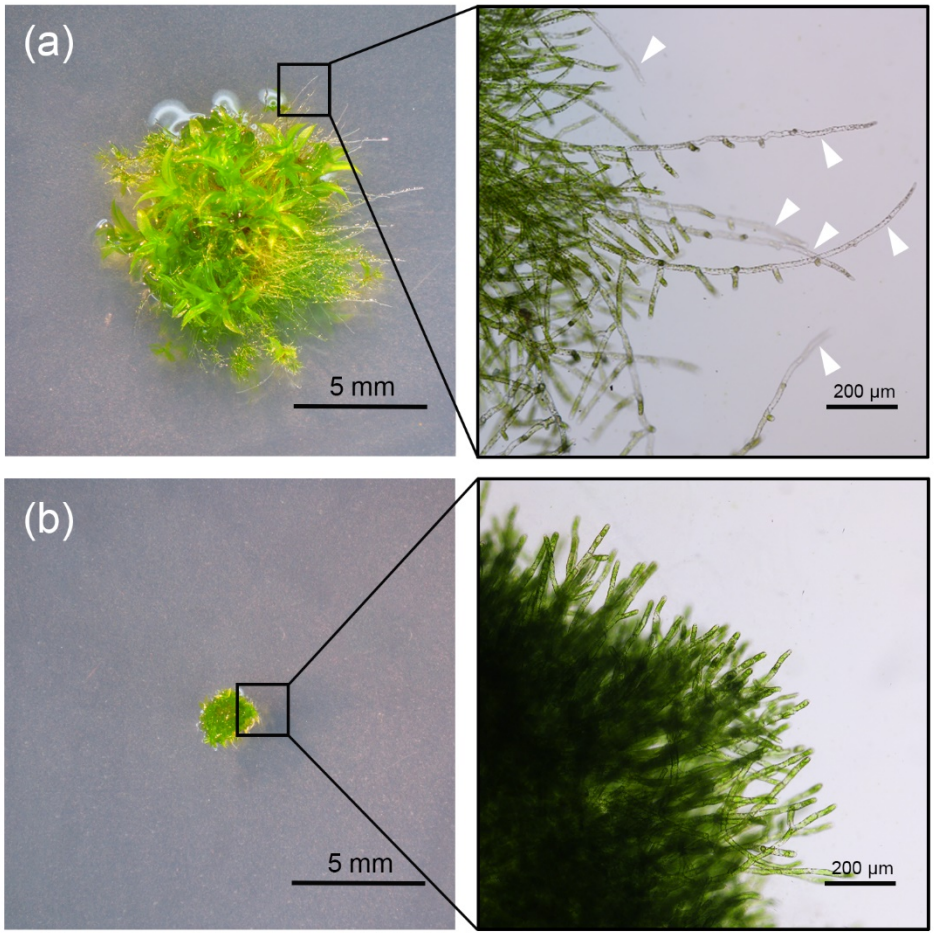
(a)
5 mm
200 µm
(b)
5 mm
200 µm

B

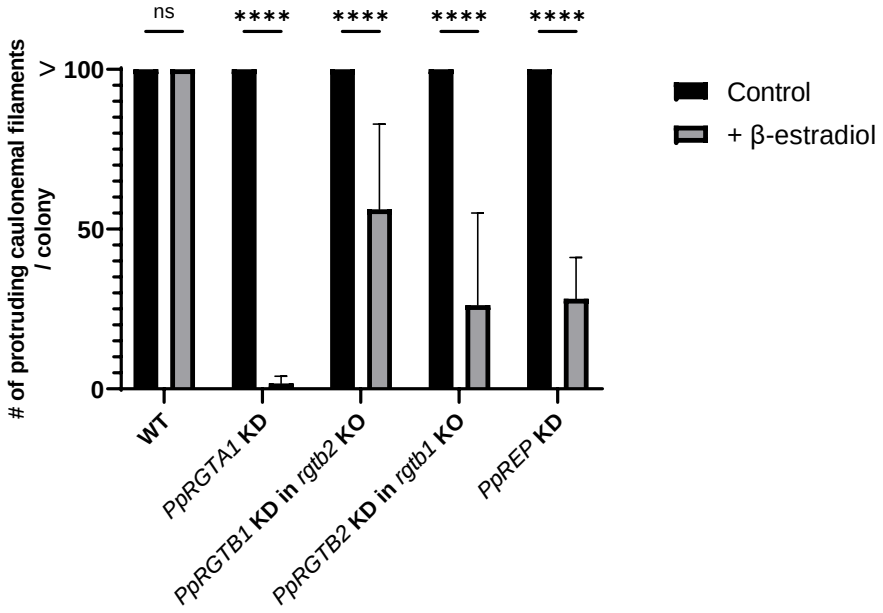
ns
****
****
****
****
# of protruding caulonemal filaments / colony
> 100
50
0
WT
PpRGTA1 KD
PpRGTB1 KD in Δrgtb2 KO
PpRGTB2 KD in Δrgtb1 KO
PpREP KD
Control
+ β-estradiol

Figure 2-11: Analysis of caulonema formation in WT and Rab-GGT KD lines grown with or without β-estradiol induction.

(A) Representative colony and filament images of WT & un-induced knockdown lines (a; collected from WT) and induced knockdown lines (b; collected from uninduced *PpRGTB2* KD in *rgtb1* KO lines) grown for 30 days on BCD medium showing how the number of protruding caulonemal filaments was measured. White arrows indicate caulonemal filaments that protrude from the edge of the colony. (B) Number of protruding caulonemal filaments counted by a Nikon TE-200 inverted brightfield microscope. The data shown are the Mean ± SD of 6 individual colonies per line.

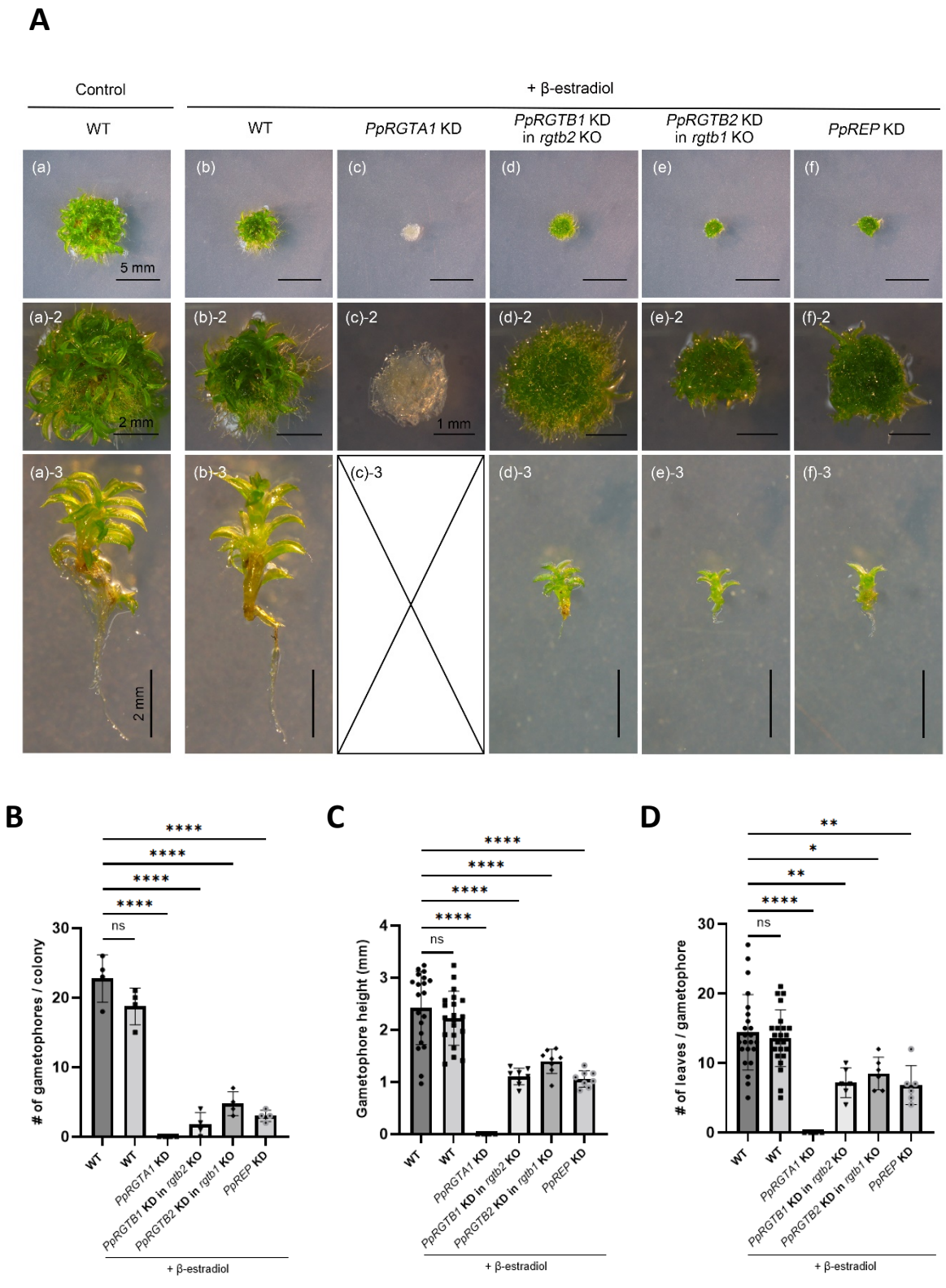
A
Control
+ β-estradiol
WT
WT
PpRGTA1 KD
PpRGTB1 KD in rgtb2 KO
PpRGTB2 KD in rgtb1 KO
PpREP KD
(a)
(b)
(c)
(d)
(e)
(f)
5 mm
(a)-2
(b)-2
(c)-2
(d)-2
(e)-2
(f)-2
2 mm
1 mm
(a)-3
(b)-3
(c)-3
(d)-3
(e)-3
(f)-3
2 mm
B
# of gametophores / colony
ns
****
C
Gametophore height (mm)
D
# of leaves / gametophore
*
**
WT
WT
PpRGTA1 KD
PpRGTB1 KD in rgtb2 KO
PpRGTB2 KD in rgtb1 KO
PpREP KD
+ β-estradiol

Figure 2-12: Morphology of colony and gametophore of WT and Rab-GGT knockdown lines with or without β-estradiol induction, and measurement of average gametophore number & height, leaves number per gametophore.

(A) Magnification of colonies (a–f and a-2–f-2) and gametophores (a-3–f-3) of 30-days WT and knockdown lines under control (a–a-3) and 1 μM β-estradiol (b, b-2, b-3–f, f-2, f-3). (B) Average number of gametophores per colony. Data shown are Mean ± SD of 4 individual colonies of WT and knockdown lines. (C-D) Average number of gametophore height and Average number of leaves per gametophore. Data represent Mean ± SD (WT $n \geq 20$, all KD lines $n \geq 5$).

The *P. patens* Rab-GGT knockdown mutants exhibit cell polarity establishment defects

As plants are composed of immobile cells, plant cell morphogenesis relies on mechanisms enabling precise control of cell division and cell expansion patterns, which are balanced by cooperation between cytoskeleton and secretory pathways (Fowler & Quatrano, 1997; Kim & Brandizzi, 2014; Wu & Bezanilla, 2014). Plant cell division is accomplished by a dynamic and complex structure called a phragmoplast, containing cytoskeletal polymers, actin filaments, and microtubules, that directs the traffic of vesicles carrying cell wall components to the nascent cell plate (Wu & Bezanilla, 2014). While most plant cells grow by diffuse (intercalary) growth, the growth of protonemal filaments, including chloronemal and caulonemal tip cells and branch initial cells in *P. patens* grow in a highly polarized manner, just like root hairs, pollen tubes, and rhizoids of many plants (Menand et al., 2007; Yi & Goshima, 2020). This mode of cell expansion

is known as tip growth, as cell wall deposition occur only at the tip of the cell (apex and sub-apex of an elongating cell), while no growth occurs in the rest of the connecting cells (Menand et al., 2007). In *P. patens* protonemal cells, actin filaments and microtubules are known to be essential for establishing and maintaining polar growth. Actin filaments accumulate near the cell tip and their directionality is determined by the convergence of microtubules near the cell tip (Wu & Bezanilla, 2018). In addition, the site of actin accumulation overlaps with class XI myosins and secretory vesicles, indicating that the apical actin accumulation correlates with polarized secretion (Furt et al., 2012). Phenotypes of the Rab-GGT KD lines included cells with randomly curved tip and multiple tips due to random planes of division, swollen or bulged cells at or near the cell tip due to reduced extension growth of the apical cells, defects in side-branch formation, indicating a partial failure in tip growth, and defects in actin-dependent chloroplast distribution, resulting in chloroplast clustering (Yang et al., 2011; Figure 2-13). RabA4D is the only member of the *Arabidopsis* RabA4 superfamily expressed in pollen and involved in the polarized deposition of cell wall components in the tips of growing pollen tubes. The loss of RabA4D in *Arabidopsis* pollen tubes leads to bulge formation, defects in tip growth and alterations in cell wall patterning (Szumlanski & Nielsen, 2009), similar to the filament phenotypes of our *P. patens* Rab-GGT KD lines. We took advantage of molecular markers, YFP-*At*RabA4d, that have been shown to be tip-localized in *P. patens* WT (Perroud & Quatrano, 2008), and examined their localization in the *P. patens* Rab-GGT KD lines (Figure 2-14).

Compared to WT, in which YFP-*At*RabA4d proteins accumulate specifically at the tip of apical protonemal cells, the site of cell extension, they were randomly

distributed throughout the filament in all Rab-GGT KD lines (Figure 2-14A). A loss of tip accumulation of YFP-*At*RabA4d in bulged protonemal cells of the *P. patens* Rab-GGT KD lines indicates loss of proper regulation of tip growth. Time-lapse microscopy was also used to observe the migration pattern of the YFP-*At*RabA4d (Figure 2-14B). While YFP-*At*RabA4d migrated towards the tip and maintained tip localization in both WT and un-induced Rab-GGT KD lines, those in induced Rab-GGT KD lines were scattered throughout the filament and especially for those in the middle, no tip-toward movement was detected. We therefore concluded that Rab-GGT plays a key role in the control of tip growth such as regulating vesicle targeting, delivery at the tip of the filament, or vesicle fusion.

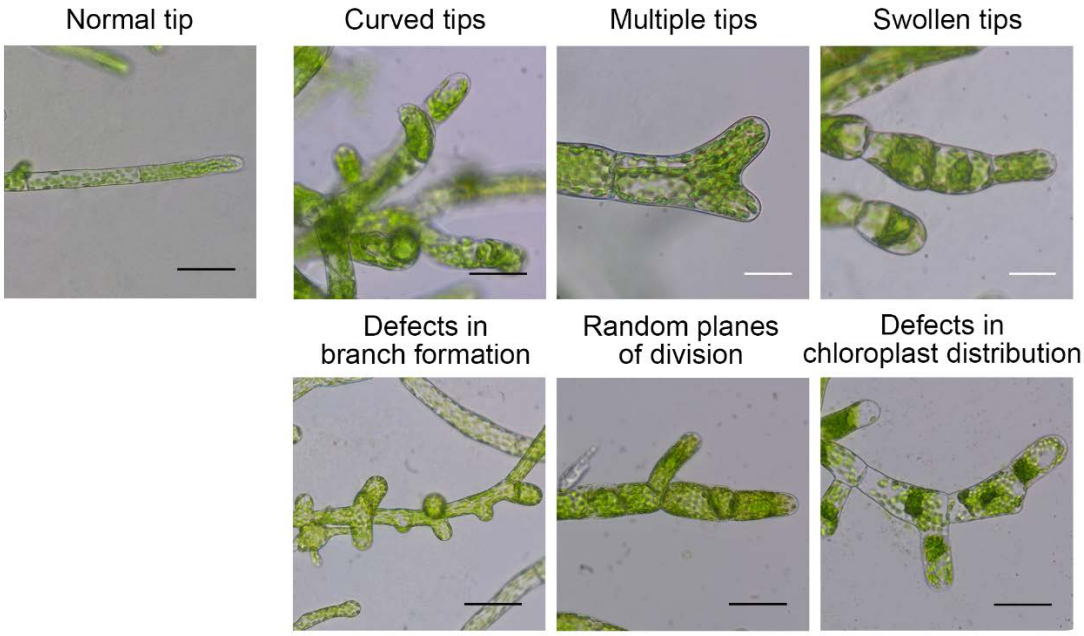

Figure 2-13: Phenotypic aberrations in Rab-GGT KD lines.

Black scale bars = 50 μm, white scale bars = 20 μm.

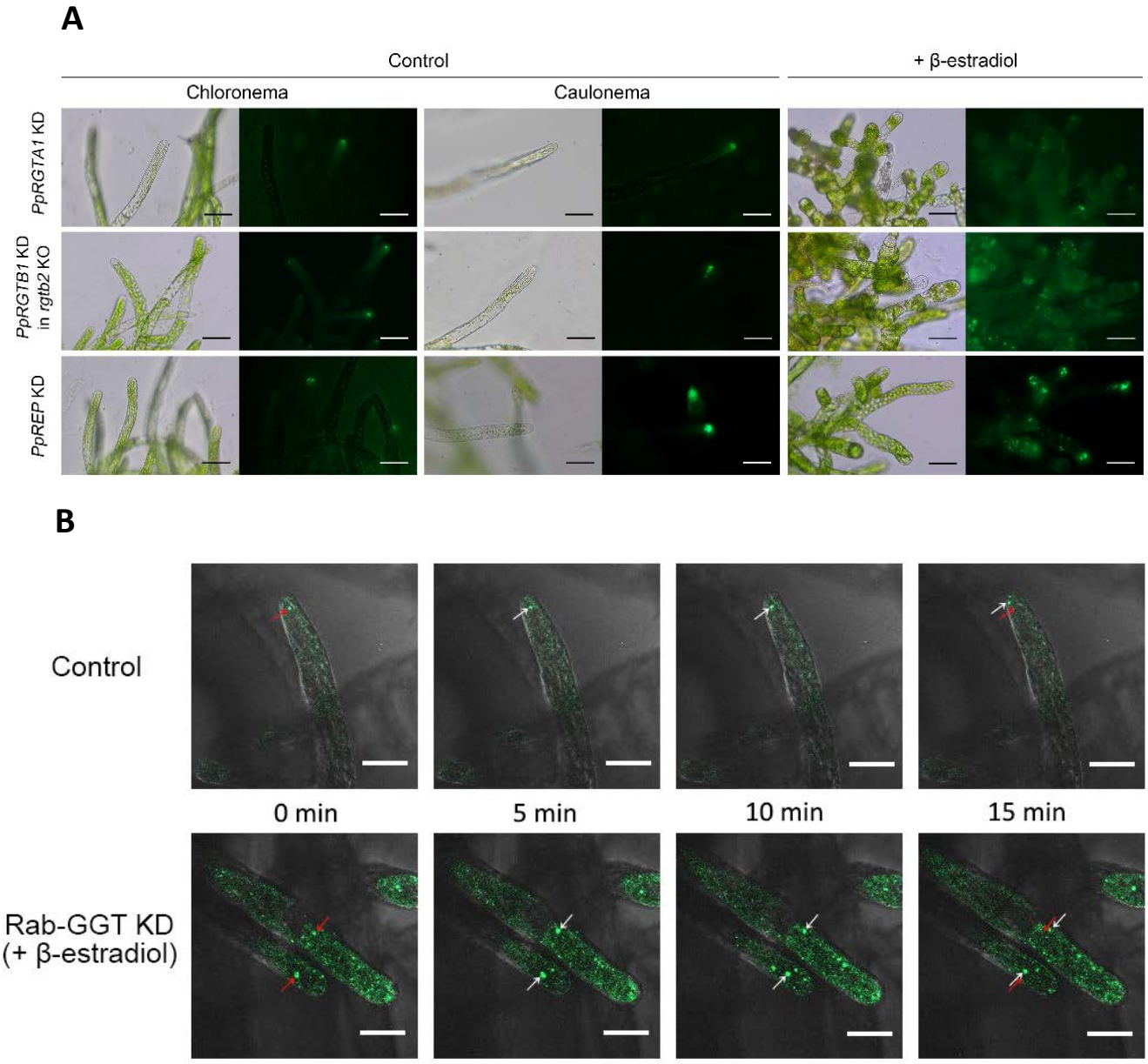

Figure 2-14: Localization of YFP-AtRabA4d in Rab-GGT knockdown lines with or without β-estradiol induction.

(A) Magnification of growing filaments of WT and Rab-GGT knockdown lines expressing YFP-*At*RabA4d grown for 10 days on BCDAT agar medium supplemented with 0.01% DMSO (Control) and 1 μM β-estradiol (+ β-estradiol). Scale bars = 50 μm. (B) Representative time-lapse images of growing filaments of WT and un-induced knockdown lines (control, top; collected from un-induced *PpRGTA1* KD lines) and

induced knockdown lines (+ β-estradiol, bottom; collected from induced *PpREP* KD lines) expressing YFP-*At*RabA4d. Images were collected every 20 sec at 40× objective (1.30 NA) with a 525 nm (GFP) emission filter. Scale bars = 50 μm. Red arrows indicate the first position of the marker and white arrows indicate the position of the marker that changes as it moves.

As in most tip-growing cells in plants, the importance of harmonization of actin filaments (or F-actin) and microtubules on the tip growth of *P. patens* protonemal cells has been demonstrated (Wu & Bezanilla, 2018). Disrupted actin filaments lead to unfocused microtubules with random orientation in contrast to the normal cytoplasmic microtubules that are oriented along the long axis of the cell, with their plus ends converging to a focused point near the cell apex (Hiwatashi et al., 2014; Wu & Bezanilla, 2018). Alterations in a subtle balance of actin assembly and disassembly and loss of function of actin-related proteins result in a dramatic reduction of filamentous tip growth, showing the requirement of the actin cytoskeleton in the expansion of tip-growing cells (Perroud & Quatrano, 2006; Augustine et al., 2011). Unlike disrupted actin filaments, disrupted microtubules do not abolish tip growth, thus do not appear to be essential for tip growth. However, pharmacologically inhibited microtubule function leads to severely altered actin organization with abnormal actin bundles migrating throughout the cell, resulting in loss of directional growth with cells that bend randomly and often form multiple tips (Doonan et al., 1988; Wu & Bezanilla, 2018).

There are several other proteins that are associated with actin filaments and/or microtubules and play essential functions in tip growth. The plant-specific kinesins

(KINID1), microtubule-based motor proteins, contribute to the proper microtubule organization during both tip growth and cytokinesis, and the loss of its function leads to slower and less straight growth (Hiwatashi et al., 2014). The actin nucleator, class II formin, is required for the generation and elongation of the actin filaments within the cluster at the cell tip and the cell cortex, and at the phragmoplast during cytokinesis (van Gisbergen et al., 2012). The proper distribution of class II formin is made by the convergence of cytoplasmic microtubules near the cell apex, and its mis-localization results in aberrant actin structure, causing cell expansion from random sites (Wu & Bezanilla, 2018). A class VIII Myosin is known to be associated with microtubule plus ends during cytokinesis to guide phragmoplast expansion near the cell tip by interacting with actin filaments (Wu & Bezanilla, 2014). Loss of Myosin VIII function exhibits reduced convergence of microtubules (spread-out), larger apical actin clusters near the cell tip, and higher class II formin activity, which triggers more and longer actin filaments produced in the apical actin accumulation and at the cell cortex, leading to a slower turnover of the actin structure, though the mechanism between the two is unclear. Also, depolymerizing the actin filaments reduces the clustering of Myosin VIII (Wu & Bezanilla, 2018). Therefore, all these cytoskeletal components are functionally connected and the coordination of them near the cell tip is crucial for persistent cell polarity during tip growth (Wu & Bezanilla, 2018).

Defects in growth directionality and cell expansion in the *P. patens* Rab-GGT KD lines resembled *P. patens* WT that lacks the function of actin, microtubule, or either or both related proteins. To determine whether those Rab-GGT KD phenotypes are associated with an altered cytoskeletal systems, we examined actin filaments and

microtubule orientation with immunofluorescence studies using F-actin antibody and anti-α-tubulin antibody respectively (Yoshikatsu Sato and Takashi Murata, http://www.nibb.ac.jp/evodevo/PHYSCOmanual/3.8.htm) (Figure 2-15). Due to the overlapping localization of secretory vesicles, apical actin cluster, and microtubule convergence (Furt et al., 2012; Wu & Bezanilla, 2018), all at the same apical domain, and the disruptions in YFP-*At*RabA4d localization from our previous data, we predicted defects in the apical actin accumulation and microtubule organization. Furthermore, since organelle distribution and partitioning rely upon the activity of the actin cytoskeleton in plants, impaired chloroplast distribution in Rab-GGT KD lines indicates that Rab-GGT might play a role in actin organization (Sheahan et al., 2004; Wada & Suetsugu, 2004). Not surprisingly, WT and un-induced KD lines showed accumulation of F-actin at the cell tip (Figure 2-15A a) and longitudinally oriented microtubules that focus at the very apex of the cell where directional cell expansion occurs (Figure 2-15B a). However, all induced KD lines displayed extensively disorganized apical F-actin and microtubule arrays throughout the bulged protonemal cells (Figure 2-15, A b and B b), indicating that Rab-GGT is required for coordination of actin and microtubules essential for proper expansion of tip-growing protonemal cells. Transformation of Rab-GGT KD lines with pTZUBI-Lifeact-mEGFP (a gift from Dr. M. Bezanilla) will allow us to track the dynamic apical F-actin network during growth and the localization of actin accumulation according to the direction of cell expansion (Vidali et al., 2009).

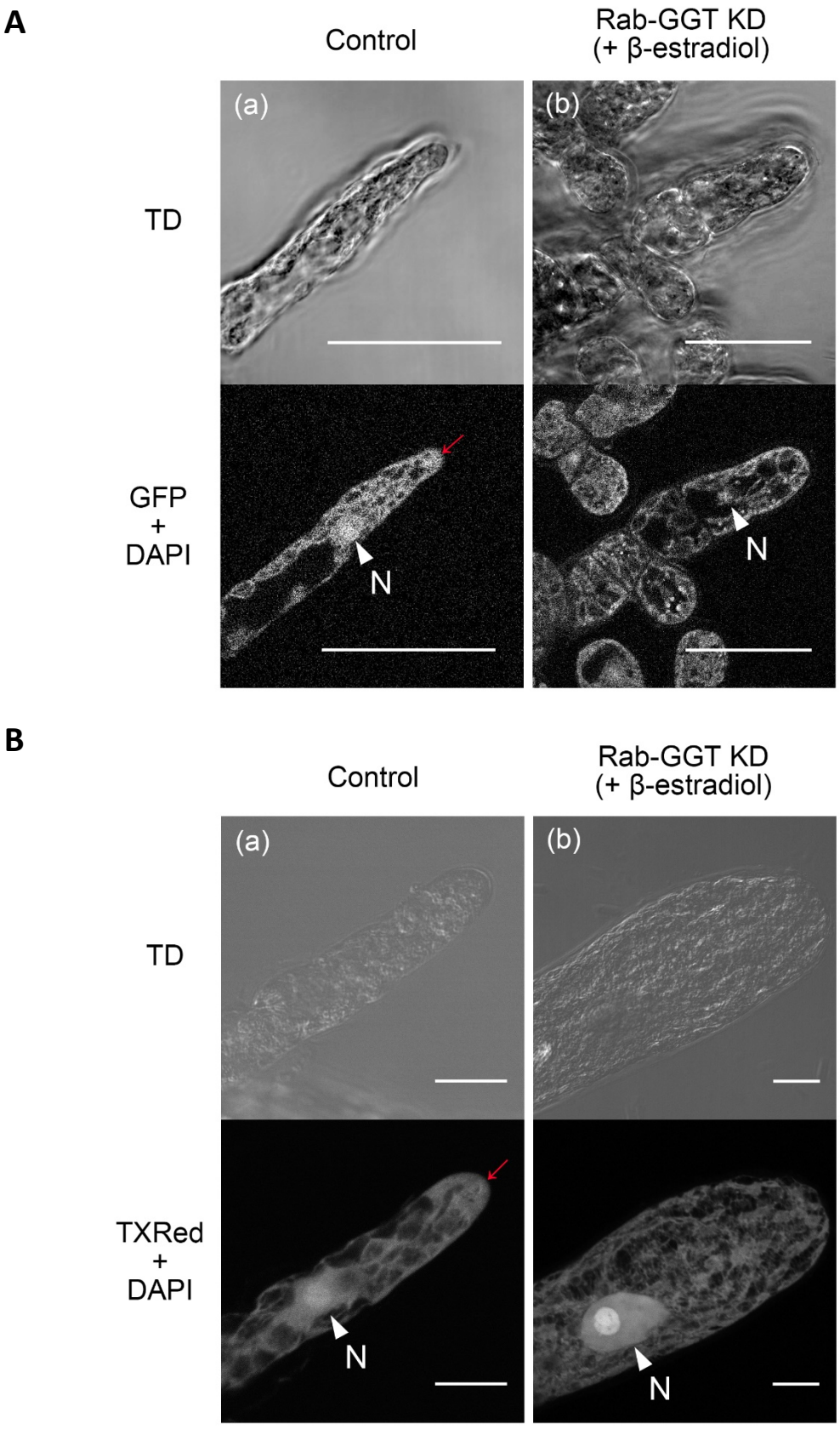
A
Control
Rab-GGT KD
(+ β-estradiol)
(a)
(b)
TD
GFP
+
DAPI
N
N
B
Control
Rab-GGT KD
(+ β-estradiol)
(a)
(b)
TD
TXRed
+
DAPI
N
N

Figure 2-15: Immunofluorescence of the organization of the cytoskeleton in WT and Rab-GGT knockdown lines with or without β-estradiol induction.

(A) Immunostaining of actin in WT and Rab-GGT KD lines with F-actin antibody. Representative images of WT & un-induced knockdown lines (control, a; collected from un-induced *PpRGTB2* KD in *rgtb1* lines) and induced knockdown lines (+ β-estradiol, b; collected from induced *PpRGTB2* KD in *rgtb1* lines) collected at a 60× objective with 450 nm (DAPi), 525 nm (GFP) emission filters. Red arrow indicates dense converging arrays of F-actin at the cell tip. Scale bars = 30 μm. (B) Immunostaining of microtubules in WT and Rab-GGT KD lines with anti-α-tubulin antibody. Representative images of WT & un-induced knockdown lines (control, a; collected from un-induced *PpRGTA1* KD lines) and induced knockdown lines (+ β-estradiol, b; collected from induced *PpRGTA1* KD lines) collected at a 100× objective with 450 nm (DAPi), 595 nm (TxRed) emission filters. Red arrow indicates the convergence of longitudinally oriented microtubules near the cell apex. Scale bars = 10 μm. TD, The transmitted light channel; TXRed, Texas Red filter; GFP, Green Fluorescent Protein filter; DAPi, 4′,6-diamidino-2-phenylindole filter. N with white arrow indicates nuclei.

CHAPTER III

RAB-GGT IN *PHYSCOMITRIUM PATENS* SHARES PARTIALLY OVERLAPPING FUNCTIONS WITH THAT IN *ARABIDOPSIS THALIANA* BUT HAS UNIQUE AND TISSUE-SPECIFIC ROLES

Introduction

Rab proteins, the largest branch of the Ras GTPase superfamily, are crucial mediators/regulators of protein transport along the endocytic and exocytic pathways in all eukaryotic cells (Hutagalung & Novick, 2011; Bhuin & Roy, 2014; Banworth & Li, 2017). They mediate intracellular membrane trafficking such as vesicle budding, vesicle delivery along cytoskeleton elements, vesicle tethering, and fusion at target compartments through the recruitment of a diverse collection of effector molecules (Pereira-Leal and Seabra, 2001; Leung et al., 2006). Similar to other small GTPases, Rab proteins function via a guanine nucleotide-dependent switch mechanism, alternating between active GTP-bound and inactive GDP-bound conformations, and are post-translationally modified for membrane attachment, as they are intrinsically soluble proteins and their activity is dependent upon association with the cytoplasmic leaflets of membranes (Pereira-Leal and Seabra, 2001; Pfeffer & Aivazian, 2004; Gutkowska & Swiezewska, 2012; Pylypenko et al., 2017). This modification of Rabs, termed Rab geranylgeranylation, is catalyzed by Rab geranylgeranyltransferase (Rab-GGT) and involves covalent attachment of a geranylgeranyl moiety (C20 isoprenoid group) to one

or (usually) two cysteine residues near the C-terminus, enabling stable membrane attachment (anchoring) with an increased affinity (Anant et al., 1998; Leung et al., 2006; Running, 2014). Rab-GGT consists of distinct α- and β-subunits, as well as an additional protein called the Rab escort protein (REP) (Leung et al., 2006). Erroneously single-geranylgeranylated or unmodified Rab proteins are mistargeted and unable to carry out their normal function (Gomes et al., 2003).

Rabs are evolutionarily conserved across the eukaryotic kingdom (Pereira-Leal and Seabra, 2001; Zerial and McBride, 2001; Vernoud et al., 2003). They comprise the largest number among the five principal families of small GTPases and their number varies extensively among species, with yeast, among the simplest eukaryotic organisms, having around 10 (7 Rabs identified in *Schizosaccharomyces pombe*; 11 Rabs identified in *Saccharomyces cerevisiae*) and mammalian and higher plant having roughly 60. This large number difference between the species reflects the greater complexity of membrane trafficking and the more demanding requirements in terms of diversification and specialization in higher eukaryotes compared to yeast (Bock et al., 2001; Pereira-Leal and Seabra, 2001; Zerial and McBride, 2001; Vernoud et al., 2003; Hutagalung & Novick, 2011). *S. cerevisiae*'s 11 Rabs are categorized into eight functionally distinct subfamilies, six of which have homologues with varying degrees of functional conservation in animals and *S. pombe*. This indicates that these six subfamilies are a minimal set of eukaryotic Rab function (Lazar et al., 1997; Pereira-Leal & Seabra, 2001; Zerial & McBride, 2001). Phylogenetic analyses show that 57 distinct Rabs present in *Arabidopsis thaliana* are grouped into only eight subfamilies and lack 80% of the predicted mammalian Rab subfamilies (about forty different functional subfamilies), suggesting the expansion of

each subfamily and possible high redundancy between members within a subfamily (Rutherford and Moore, 2002; Vernoud et al., 2003; Pinheiro et al., 2009). However, Rabs in the *Arabidopsis* lineage have undergone an 'adaptive radiation' generating a distinct composition of Rab families that may be capable of performing plant-specific functions (Rutherford and Moore, 2002).

As plants transitioned from an aquatic to a terrestrial mode of life, they have evolved complex molecular, physiological, and biochemical mechanisms to adapt to abiotic stress such as extreme environmental variations in light, temperature, salinity, and water availability (Rensing et al., 2008; Kramer, 2009). Due to the phylogenetic position of the moss *Physcomitrium patens* in one of the earliest groups of land plants (the non-vascular, multicellular terrestrial bryophytes) as a bridge between green algae and higher vascular plants, and its well-developed stress tolerance, *P. patens* became an excellent model system to understand the evolution of multicellularity, photosynthesis, and plant responses to various biotic and abiotic stresses that facilitated the colonization of the land (Bowman et al., 2007; Floyd & Bowman, 2007; Rensing et al., 2008; Khraiwesh et al., 2015; Rensing et al., 2020). *P. patens* displays a simple morphology with a small number of cell types that can absorb water and nutrients via the whole surface, which accelerates the elucidation of developmental processes and enables hormone application simultaneously to all cells (Cove et al., 2006; Decker et al., 2006; Strotbek et al., 2013). Moreover, *P. patens'* high frequency of homologous recombination-mediated gene targeting, comparable to that of yeast, makes it suitable to uncover gene function by reverse genetics (Schaefer & Zryd, 1997). As the dominant generation in the life cycle of mosses is the haploid gametophyte, the direct forward analysis of mutants is possible

through recessive loss-of-function phenotypes, facilitating stable, immediate, and rapid genetic studies without the need for further crosses (Cove, 2005; Cove et al., 2009). Like higher plants, growth and development in *P. patens* is regulated by sensing and responding to both external and internal signals, such as nutrient, light and phytohormones including auxins, cytokinins, and abscisic acid (Schumaker & Dietrich, 1997; Thelander et al., 2005; Decker et al., 2006). The *P. patens* life cycle begins with germination of a haploid spore followed by outgrowth of the protonema, filamentous networks of cells with apical growth and subapical branching (Cove & Knight, 1993; Cove et al., 2006; Prigge & Bezanilla, 2010). Spore germination and protonemal growth are influenced by light and water availability (Maciel da Silva et al., 2009). The protonema consists of two cell types, chloronemal and caulonemal cells, that are morphologically and functionally distinct. Initially emerged chloronemal cells are characterized by slow growth, numerous chloroplasts, and perpendicular cell walls, and are involved in photosynthesis, whereas caulonemal cells that are formed later are characterized by rapid radial growth, fewer chloroplasts, and oblique cell walls, and link to substrate colonization and nutrient acquisition (Menand et al., 2007). Within the protonemal filament, a chloronemal cell may have four developmentally distinct potential fates (Decker et al., 2006). It may retain a chloronemal identity and form a new chloronemal cell, or it may differentiate into a caulonemal cell under the effect of auxin and high energy growth conditions such as relatively high light intensity and exogenous sugar (glucose) supply (Thelander et al., 2005). Another possibility is that it may form a bud, a structure with an apical three-faced cell, which further develops into the leafy gametophore under the effect of cytokinin. Lastly, subapical chloronemal cells may form

spherical, thick-walled cells called brachycytes or brood cells and nearly cytoplasm-free tmema cells under the effect of ABA (Goode, et al., 1993). Both cell types enable plant survival in unfavorable environmental conditions such as desiccation and freezing (Arif et al., 2019).

The Rab geranylgeranylation machinery is known to be conserved among eukaryotic species. The complementation failure of yeast REP with recombinant *Arabidopsis thaliana* REP can be compensated for by the change of only a single amino acid from asparagine to arginine, demonstrating its close functional homology between two different species (Hála et al., 2005). Both *Arabidopsis* and *P. patens* contain two putative Rab-GGT β subunits, *RGTB1* and *RGTB2*, and a single copy of REP. Based on a phylogenetic tree of prenylation components in *Arabidopsis* and *P. patens* showing their evolutionary relationship, it appears that gene duplication of the Rab-GGT β subunit occurred independently in each lineage (Thole et al., 2014). Unlike *Arabidopsis*, which has two putative Rab-GGT α subunits, *P. patens* harbors only a single copy of Rab-GGT α subunit, *RGTA1*. Prior to this dissertation, no Rab-GGT α subunit phenotype has been reported in any plants. In both species, while mutations in the single copy of Rab-GGT β subunits are viable, the double *rgtb1 rgtb2* mutants are non-viable, indicating possible functional redundancy of these putatively duplicated genes (Shi et al., 2016). Among the Rab-GGT components, only Rab-GGT β subunits' function has been obtained, and only from *Arabidopsis* through loss-of-function genetic tools and consequent biological effects. Knockouts of *AtRGTB1* display pleiotropic phenotypic defects such as a dwarfing phenotype, loss of apical dominance and loss of gravitropic response (Hála et al., 2010), and knockouts of *AtRGTB2* are indistinguishable from wild-type plants in their overall

morphology and the time of flowering, but show abnormal tip growth, including root hair and pollen tube deformations (Gutkowska et al., 2015). These data suggest their important roles in regulating growth, developmental processes, and environmental responses and also indicate the partial redundancy of *AtRGTB1* and *AtRGTB2* because *AtRGTB2* could not fully compensate for the loss of function of *AtRGTB1* (Hála et al., 2010; Gutkowska et al., 2015, Shi et al., 2016). However, it is not yet known whether these roles are conserved among plants (Running, 2014; Hemsley, 2015).

Previously, the full disruption of *P. patens* Rab-GGT α subunit *PpRGTA1* or both two β subunits *PpRGTB1* and *PpRGTB2* by targeted gene replacement appeared to be lethal, while knockouts of either of the two β subunits resulted in no phenotype. These data only indicated a requirement of these genes for moss viability and potential complete functional redundancy of two β subunits (Thole et al., 2014). As describe in chapter II, we succeeded in generating viable *P. patens* Rab-GGT knockdown mutant lines using transient RNAi approaches and identified the importance of Rab-GGT in cell morphogenesis and cell polarity establishment through their pleiotropic developmental deviations, such as retarded growth, abnormally shaped cells by swelling and defective cell divisions, diminished rate of caulonemal filaments elongation, defective bud development, and defects in vesicle transport and cytokinesis with disruption in actin and microtubule assembly and organization (Chapter II).

In this chapter, the aim is focused on investigating the hypothesis that the roles of Rab-GGT in the stress-related biochemical and metabolic pathways are evolutionarily conserved at least partially in different plant species. Here, alterations in the phenotypes, sensitivity, and stress tolerance of Rab-GGT knockdown lines under various

environmental (phototropism, gravitropism) and hormonal (NAA, BAP, ABA) treatments are analyzed.

Materials and Methods

Phenotypic Analysis

The moss *Physcomitrium patens* was photographed using a Nikon Digital Slight DS-Fi1 camera mounted on (attached to) a Nikon SMZ1500 stereomicroscope for colony image and a Nikon TE-200 inverted brightfield microscope for filament image. All image analyses were performed using ImageJ (Abràmoff et al., 2004).

Sample Preparation for Compositional Analysis

The moss *Physcomitrium patens* was blended with autoclaved deionized water using a Polytron homogenizer (T20B.S1, IKA) and distributed onto BCDAT medium supplemented with or without 1 μM β-estradiol overlain with cellophane under continuous white light at 25℃ for 7~10 days (Cove et al., 2009; Thole et al., 2014). The collected samples were freeze-dried (FreeZone, Labconco™) and stored in -20℃ until needed.

Compositional Analysis

Compositional analysis of the WT and the Rab-GGT KD lines incubated with or without β-estradiol was performed by the NREL LAP procedure (Sluiter et al., 2008; Sluiter et al., 2011). 0.1 g of the freeze-dried sample was dissolved in 1 mL of 72% H_2SO_4 with a magnetic bar at 30°C for 1 hour in an incubator shaker. The dissolved sample was diluted

to 4% H_2SO_4 by adding 28 mL of deionized water and then autoclaved at 121°C, 15 psi for 1 hour (hydrolysis). The autoclaved sample was filtered by a ceramic crucible and part of the filtrate was neutralized with $CaCO_3$ at pH 7. Soluble sugars in the filtrate were analyzed by HPLC equipped with a refractive index detector (RID) and diode array detector (DAD). A Bio-Rad Aminex HPX-87P column (Richmond, CA, USA) was used with a rate of 0.6 mL/min of 4 mM H_2SO_4 as a mobile phase at 60°C. All sugars were calibrated against certified standards (Absolute Standards Inc., Hamden, CT, USA). Residual solids in the crucible were dried at 105°C overnight (moisture removal). The weight of the dehydrated solids corresponded to the amount of lignin and ash in the sample. The dried solids in the crucible were then calcined at 575°C for 8 hours. Lost weight and residual weight were consistent with the amount of lignin and ash in the sample, respectively (Hossain et al., 2019).

Phototropism Assay

Protonemal tissues (1-2 mm in diameter) were inoculated and grown on BCDAT medium supplemented with or without 1 μM β-estradiol in a petri dish under continuous white light at 25°C for 7~10 days. The dishes were then placed under unidirectional light that is generated by passing it through a red acrylic plastic plate in a light proof box at the same temperature for 2~4 weeks.

Gravitropism Assay

Protonemal tissues (1-2 mm in diameter) were inoculated and grown on BCDAT medium supplemented with or without 1 μM β-estradiol in a petri dish under continuous white

light at 25°C for 5 days. The dishes were vertically oriented for 5 days, then covered with aluminum foil, and grown in the dark at the same temperature for 2~4 weeks.

Hormone Sensitivity Assay (ABA, NAA, BAP)

Protonemal tissues (1-2 mm in diameter) were inoculated and grown on ammonium tartrate-free BCD medium supplemented with or without 1 μM β-estradiol, and with or without different concentrations of exogenous additives (phytohormones, sugars) in a petri dish under continuous white light at 25°C for 2~3 weeks. Exogenous additives included concentrations of 0.1, 1, and 10 μM BAP, NAA, or ABA, and concentrations of 150 mM glucose (metabolizable sugar) or mannitol (non-metabolizable sugar). For colony growth measurement (quantification), four independent colonies of each line for each concentration were photographed using a Nikon stereomicroscope (SMZ1500) and analyzed using ImageJ (https://imagej.nih.gov/ij/).

Desiccation Assay

Desiccation assay was adapted from Komatsu et al. (2013). Protonemal tissues were grown for 10 days on 4 cut cellophane-layered BCDAT medium. Mutant lines were grown on 4 cut cellophane-layered BCDAT medium for 5 days and then transferred to BCDAT medium with 1 μM β-estradiol and incubated for 5 days for the induction of knockdown. 4 cut cellophanes were transferred to BCDAT medium supplemented with ABA at concentration of 1, 10, or 50 μM for 24 hours. Control treatments lacked the addition of ABA. After the ABA treatment, the cellophanes were transferred to an empty petri dish and desiccated inside a laminar flow hood for 24 hours. The desiccated tissues were rehydrated (tissues grown on 1/4 cellophane were rehydrated with 1 mL of sterile

water) and then incubated under the standard growth conditions for 2 weeks. Recovery rate was quantified by chlorophyll content analysis.

Chlorophyll Content Analysis

Chlorophyll content of ABA-treated, desiccated & rehydrated plants was determined in three independent replicates, as previously described by Komatsu et al. (2013) and Frank et al. (2004). The chlorophyll of each plant was extracted by homogenizing protonemal tissue with 5 ml of 80% (v/v) acetone. To remove cell debris, the samples were centrifuged for 5 min at 14,000 g. For chlorophyll quantification, the absorbance values of the supernatants were measured at wavelengths of 645 and 663 nm using a spectrophotometer (SpectraMax® M2). After removing as much of the remaining supernatant as possible from the samples, the samples were dried in a laminar flow hood for 24 hours until a stable dry weight was obtained. The total chlorophyll was calculated as chlorophyll *a* + chlorophyll *b* (mg g^{-1} dry weight) using the following formula: mg chlorophyll / g dry weight = $[(A_{663})\ (0.00802) + (A_{645})\ (0.0202)] \times 5$ / dry weight. The data analysis included three independent experiments.

Statistical Analysis

Statistical analysis was performed using GraphPad Prism version 9.3.1 for Windows (GraphPad Software, San Diego, California USA, www.graphpad.com). The P-values were obtained with one-way or two-way analysis of variance (ANOVA) and GP P value style was used: 0.1234 (ns), 0.0332 (*), 0.0021 (**), 0.0002 (***), < 0.0001 (****).

Results and Discussion

Rab-GGT KD does not affect the carbohydrate composition of the cell wall

Plant cell expansion is crucial for cell morphogenesis during cellular growth. The expansion is achieved by the vacuolar turgor pressure (enlargement of vacuole) that pushes the plasma membrane against the cell wall (Green, 1962). The plant cell walls are mainly composed of polysaccharide polymers such as cellulose, hemicellulose, and pectin, but often also contain glycoproteins and lignin (Zhang et al., 2021). Cellulose is synthesized by cellulose synthase complexes (CSCs) in the plasma membrane and consists of β-1,4-linked glucan chains, which hydrogen bond with each other to form microfibrils. Cellulose microfibrils are the major load-bearing polymers of the cell wall and their organization is directed by cortical microtubules, which align perpendicular to the axis of growth, facilitating directional cell growth. (Paredez et al., 2006; Li et al., 2011; Bringmann et al., 2012). Perturbance of cortical microtubules disorganizes the orientation of cellulose microfibril deposition, constraining the pattern of cell expansion (Bashline et al., 2014). The cellulose microfibrils are bound together and extensively cross-linked by a matrix of hemicellulose and either pectin or lignin to form an organized cell wall (Fosket, 1994; Gibson, 2012). Hemicellulose and pectin are synthesized by glycosyltransferases in the Golgi apparatus. They are transported to the growing cell wall (expanding and maturing cell plate) via trans-Golgi derived vesicles, whose movement is dependent on actin filaments (in an actin-myosin-dependent fashion) (Chen et al., 2007; Sinclair et al., 2018). Disruption of actin filaments disrupts Golgi movement and delivery of CSCs to the plasma membrane, and perturbs vesicle trafficking, altering the configuration and distribution of cell wall components (Chen et al., 2007; Sampathkumar

et al., 2013). Therefore, the cytoskeleton plays a very important role in cell wall component trafficking.

Rab-GGT KD lines exhibited defects in polarized cell expansion and microtubule organization intimately related to the orientation of cellulose microfibrils and their deposition at the tip. To see whether the partial loss of Rab-GGT influences the process of production, transport, and deposition of cell wall components, we extracted carbohydrates from WT and β-estradiol-induced Rab-GGT KD lines and compositionally assessed the amount of glucan (cellulose), and xylan and arabinan (hemicellulose) using HPLC (Table 3-1, Figure 3-1). There was no significant difference in content weight (%) between WT and all Rab-GGT KD lines. This indicates that cellulose production by CSCs in the plasma membrane and hemicellulose production in the Golgi are not disturbed, but later targeting of secretory vesicles to the plasma membrane is disturbed based on the mis-localization of YFP-*At*RabA4d in Rab-GGT KD lines. However, it is not yet clear whether the cell wall components are functional and deposited in the correct region. In the future, we will immunolabel the cell wall components using antibodies such as BS-400-4 to detect mannan, BS-400-2 to detect callose, and LM2 to detect arabinogalactan protein (AGP), as we did to observe cytoskeleton indirectly. Previously, cell wall immunolabeling experiments were performed with WT and *Ppera1* and *Ppggb* knockout mutants that exhibited partial and complete loss of polarity, respectively, and a less and more severe phenotype than our Rab-GGT KD lines, respectively. Mannan (hemicellulose) was evenly distributed around the cells of WT and both mutants, demonstrating the presence of a functional cell wall (Thole et al., 2014); thus, the cell wall of our Rab-GGT KD lines is also expected to be functionally intact. Callose is

transiently accumulated at the cell plate at plasmodesmata during cell plate expansion and replaced by cellulose in mature stages (Jawaid et al., 2020). AGP is required for the extension of apical tip-growing cells and its presence is particularly abundant in the cell wall at the tip regions of growing protonemal cells (Lee et al., 2005). The presence of callose and AGP was restricted to cell boundaries and tips, respectively, in WT and *Ppera1,* whereas in *Ppggb,* callose was uniformly distributed around all cells and no AGP was detected, suggesting a lack of cell maturation and differentiation along with loss of tip growth (Thole et al., 2014). Since the phenotypic severity of Rab-GGT KD lines in tip growth lies between that of *Ppera1* and *Ppggb,* it will be interesting to see an altered localization of cell wall components during cell wall deposition.

Table 3-1

Cell wall carbohydrate composition analysis for WT and Rab-GGT KD lines.

Content wt (%)	WT	*PpRGTA1* KD (+ β-estradiol)	*PpRGTB1* KD in rgtb2 KO (+ β-estradiol)	*PpREP* KD (+ β-estradiol)
Glucan	24.26 ± 2.36	21.5 ± 1.23	24 ± 0.5	26.73 ± 1.8
Xylan	13.55 ± 4.9	12.53 ± 0.41	13.35 ± 2.74	11.07 ± 4.18
Arabinan	2.63 ± 1.49	3.16 ± 0.23	2.95 ± 1.17	2.21 ± 0.8
Lignin-like	21.2 ± 4.17	22.76 ± 2.21	20.37 ± 1.17	19.4 ± 4.21
Ash	4.23 ± 0.64	3.72 ± 3.73	3.24 ± 2.06	3.49 ± 3.18
Others	34.13 ± 9.87	36.33 ± 4.29	36.1 ± 4.47	37.1 ± 6.39

Values are mean ± SD, n = 3, P = ns (P > 0.9999).

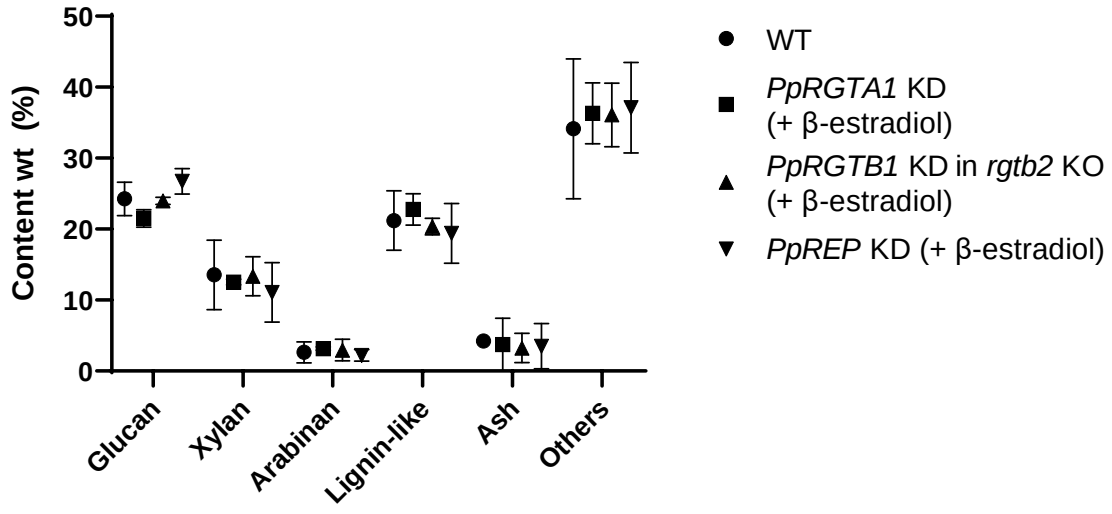

Figure 3-1: Cell wall carbohydrate composition analysis for WT and Rab-GGT KD lines.

Values are mean ± SD, n = 3, P = ns (P > 0.9999).

Knockdown of Rab-GGT β subunits or REP does not alter phototropic & gravitropic responses, showing normal protonemal positive phototropism & caulonemal negative gravitropism in the dark

In order to get acclimatized in a terrestrial environment, the stationary early land plants have evolved growth-driven movements to cope with the changing conditions. These directed growth movements guided by environmental stimuli (e.g., light, temperature, water, salinity, and gravity) are known as tropisms. The phytohormone auxin is a key mediator responsible for asymmetric tropic growth (Vandenbrink et al., 2014; Han et al., 2021). The directional auxin flow is established via polarly localized PIN auxin exporters that redirect auxin fluxes in response to various external cues, generating asymmetric auxin distribution to initiate bending (Han et al., 2021). In *P.*

patens tip-growing filamentous protonema, only the apical cells exhibit polarized growth and various tropic responses as they bend with respect to orienting vectors, such as unidirectional light and gravity (Cove et al., 1978; Perroud & Quatrano, 2006). Thus, both elongation and division are restricted to a single apical cell in the entire signaling pathway, from perception of the orienting vector to an altered growth response (Perroud & Quatrano, 2006; Menand et al., 2007). Since Rab-GGT KD lines displayed pleiotropic defects directly or indirectly linked to cell polarity regulation, such as retarded cell elongation and delayed differentiation of protonema, and because *Arabidopsis rgtb1* mutants showed tropism defects, whether the phototropic and gravitropic responses of mutant lines are also affected was investigated.

Phototropism enables plants to bend towards (positive, e.g., protonema) or move away from (negative, e.g., rhizoids) a light source. In *P. patens*, phototropic responses are controlled by a light receptor called phytochrome that acts as a molecular switch in response to red/far-red light. Protonemata respond differently to varying light quality and intensity; in unidirectional red light (665 nm), primary chloronemata show positive phototropism at low fluence rates and negative phototropism at high fluence rates; in unidirectional far-red light (730 nm), primary chloronemata display strong positive phototropism (Jenkins & Cove, 1983; Bao et al., 2015). In the case of *PpRGTA1* KD lines, it was difficult to clearly observe their tropic responses due to the extremely slow growth of the filaments and lack of caulonema differentiation. Except for *PpRGTA1* KD lines, protonemata of all other Rab-GGT KD lines (Figure 3-2A e–h), protruding from the colony edge, were significantly shorter than those of WT (Figure 3-2A a, d), but exhibited a normal positive phototropism, as did WT growing towards the unilateral light

source (Figure 3-2, A and B). We did not observe any differences between WT and *PpRGTB1* or *PpRGTB2* KO mutants, as both the protonemata and gametophores responded to the change in the direction of light by bending towards it (Figure 3-2A b, c). To analyze the ability to sense changes in light direction and quantify the phototropic responses, the plates were placed under unidirectional light for 1 week, rotated 90 degrees, and then incubated for 1 more week (Figure 3-2D). The curvature of bending filaments towards the light vector was measured and one-way ANOVA was used to determine whether there was a statistically significant difference. There was no significant difference in bending angles (P = ns) between mean WT (84.54°) and β-estradiol-induced WT (85.61°) or three Rab-GGT KD lines (82.06° in *PpRGTB1* KD in *rgtb2* KO, 79.55° in *PpRGTB2* KD in *rgtb1* KO, and 88.93° in *PpREP* KD) (Figure 3-2E). Hence, it seems clear that the knockdown of either of the *P. patens* Rab-GGT two β subunits *RGTB1* or *RGTB2* in *rgtb2* or *rgtb1* knockout background or REP do not have an impact on the phototrop ic growth. However, *PpRGTA1* KD lines exhibited both positive and negative tropic responses to light, though they had very few and tiny filaments by severely disrupted tip cell growth and differentiation. This may be because the ability of the mutants to adopt a positive phototropic response is impaired or the degree to which the mutants respond differently to different light qualities and intensities have been switched, resulting in positive phototropism only at specific fluence rates and wavelengths. The β-estradiol-dependent inducible RNAi system in *P. patens* mediated by an estrogen receptor-based transcriptional activator XVE allowed modulation of the induction level by controlling the β-estradiol concentration from 0.001 μM to 1 μM (Kubo et al., 2013). Therefore, a phototropic response of the *PpRGTA1* KD lines induced

with a lower β-estradiol concentration (0.01 μM) was also observed (Figure 3-2C). The lower induction level did not significantly affect the survival improvement of *PpRGTA1* KD lines, but the filaments were slightly longer due to the reduced knockdown level and consequently a slightly less severe phenotype than those at the high induction level (1 μM). The growth direction of filaments of *PpRGTA1* KD lines with 0.01 μM β-estradiol induction was still variable, showing both positive and negative phototropism, as with 1 μM β-estradiol induction. Some filaments tended to grow in a cascading (stepped or stepwise) fashion, possibly due to the random transition between positive and negative phototropism by either partial or complete impairment in phototropic cognition. However, since even a slight knockdown greatly affects the viability of *PpRGTA1* KD lines, it may be a defect due to an already debilitating health condition. In the future, it will be interesting to see the different phototropic responses of Rab-GGT KD lines upon unidirectional light treatment with different qualities and intensities.

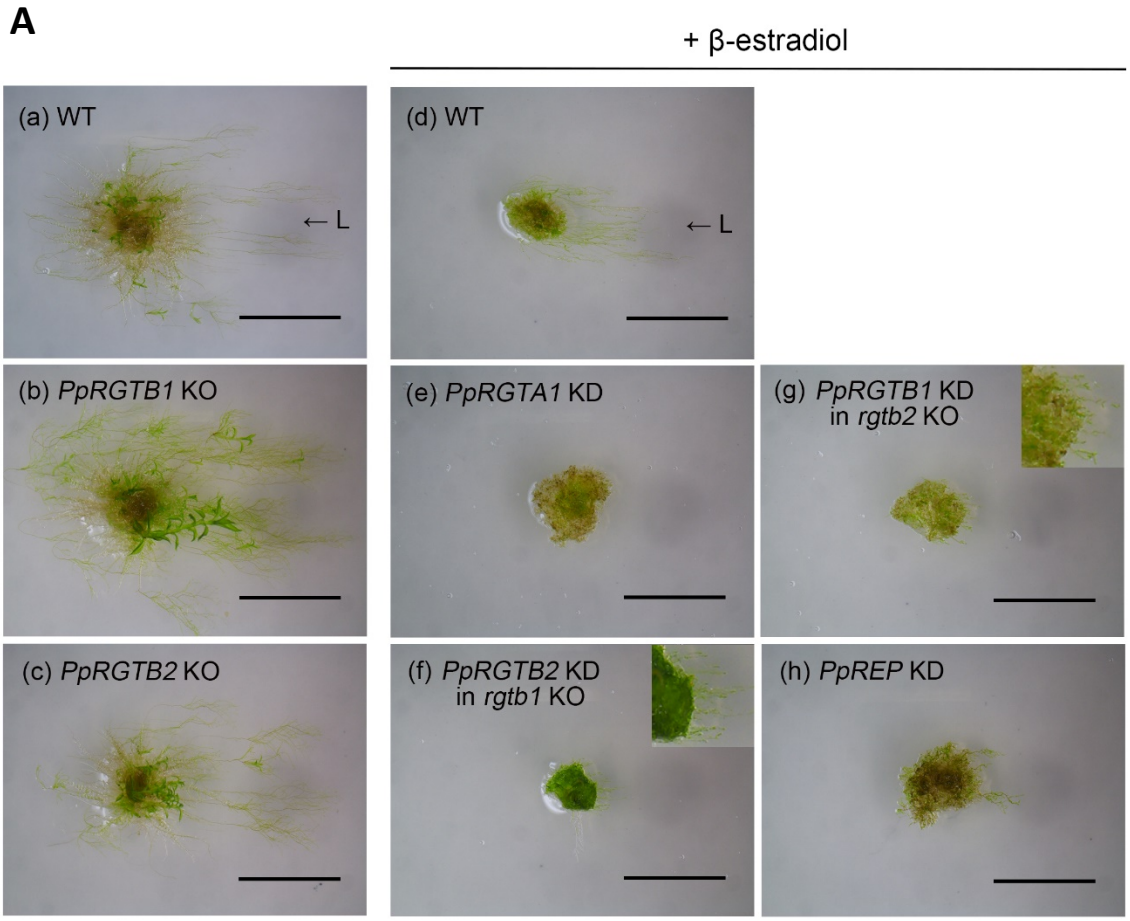
A
+ β-estradiol
(a) WT
← L
(d) WT
← L
(b) PpRGTB1 KO
(e) PpRGTA1 KD
(g) PpRGTB1 KD in rgtb2 KO
(c) PpRGTB2 KO
(f) PpRGTB2 KD in rgtb1 KO
(h) PpREP KD

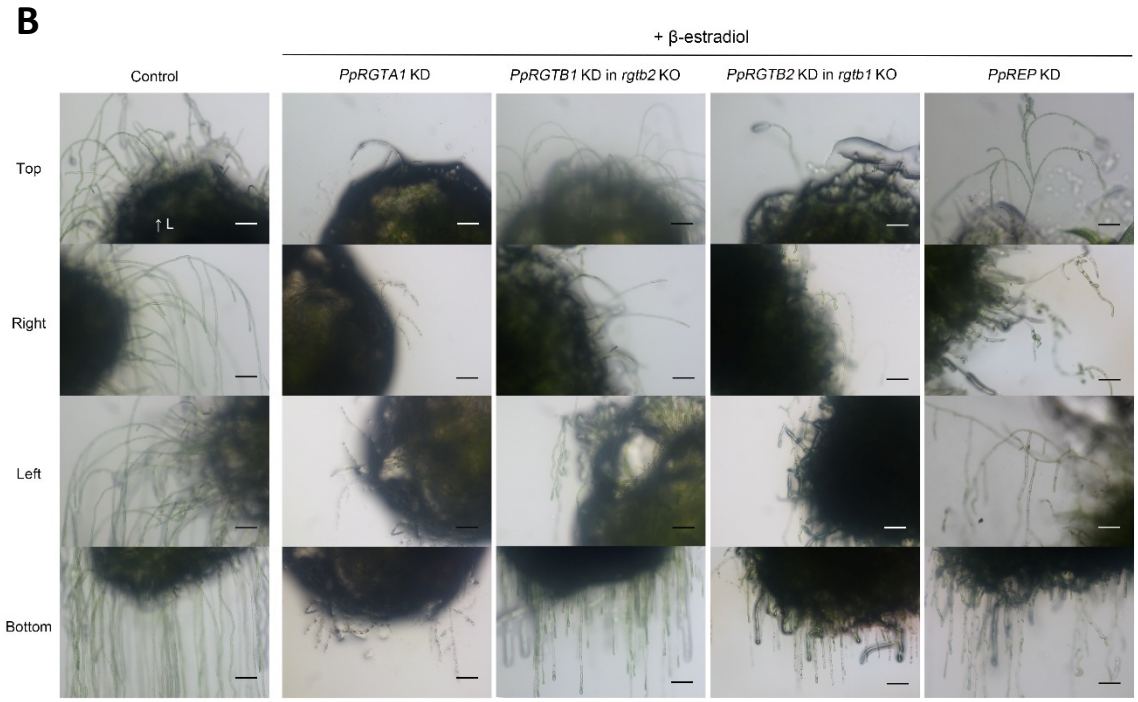
B
+ β-estradiol
Control
PpRGTA1 KD
PpRGTB1 KD in rgtb2 KO
PpRGTB2 KD in rgtb1 KO
PpREP KD
Top
Right
Left
Bottom
↑ L

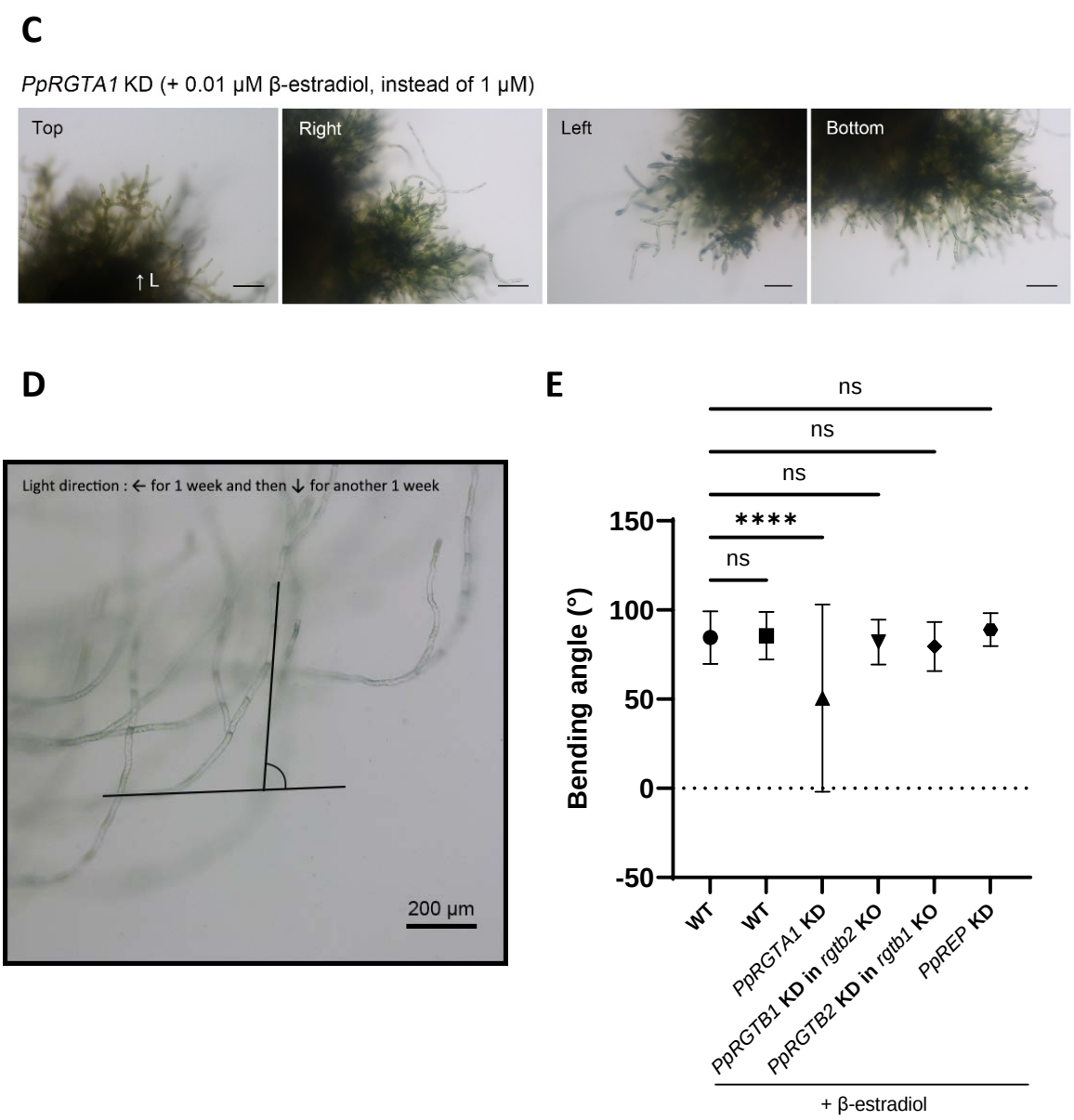

Figure 3-2: Phototropism assay.

(A) Phototropic phenotype of colony of WT and Rab-GGT mutants grown under unidirectional light for 4 weeks (a–c) and 2 weeks (d–h). Scale bars = 5 mm. '↑ L' indicates the direction of light. (B) Phototropic phenotypes of protonemata of WT and Rab-GGT mutants grown under unidirectional light for 2 weeks. Scale bars = 200 μm. (C) Phototropic phenotypes of protonemata of *PpRGTA1* KD lines under lower induction

level (0.01 μM β-estradiol). Scale bars = 200 μm. (D) Protonemata were grown under unilateral red light for 1 week and then for another 1 week with a 90-degree rotation around the light direction. The figure represents how the curvature of bending filaments were measured. A filament not bent towards the final light direction was measured as 0 degrees and a filament bent parallel to the final light direction was measured as 90 degrees. Due to the viability issue, *PpRGTA1* KD lines (+ β-estradiol) were placed under unilateral red light for 10 days and the bending angles were measured. A filament growing perpendicular to the light direction was measured as 0 degrees and a filament bent towards or against the light direction was measured as 90 degrees or –90 degrees, respectively. (E) Quantification of bending angles of protonemata. Data shown are Mean ± SD (WT n = 35, Rab-GGT KD lines n > 15).

Gravitropism orients plants parallel to (positive, e.g., rhizoids) or against (negative, e.g., gametophores) the gravity vector. Among two cell types of the *P. patens* protonema, chloronema and caulonema, only caulonema are differentiated in the dark and dark-grown caulonema and gametophores display negative gravitropism (Jenkins et al., 1986). Gravitropic responses of the *PpRGTA1* KD lines could not be analyzed because they were unable to survive in the absence of light even at lower induction levels (0.001, 0.01, and 0.1 μM β-estradiol) and no caulonema was formed even on growth medium supplemented with sucrose, an exogenous glucose that stimulates caulonema formation (Thelander et al., 2005) (data not shown). Except *PpRGTA1* KD lines, caulonemal filaments of all other Rab-GGT KD lines (Figure 3-3A e–h), mostly protruding from the top of the colony edge, were drastically shorter than those of WT (Figure 3-3A a, d), but

exhibited a normal negative gravitropism as did WT growing in a direction away from the gravity vector (Figure 3-3, A and B). As in the phototropism assay, we did not observe any differences between WT and *PpRGTB1* or *PpRGTB2* KO mutants (Figure 3-3A b, c). To analyze the ability to perceive shifts in gravity and quantify the gravitropic responses, the plates were vertically oriented, covered with aluminum foil, incubated for 2 weeks, rotated 90 degrees, and then incubated for 2 more weeks (Figure 3-3C). The curvature of bending caulonemal filaments against the gravity vector was measured and statistically compared with one-way ANOVA. There was no significant difference in bending angles (P = ns) between mean WT (87.90°) and β-estradiol-induced WT (85.41°) or three Rab-GGT KD lines (86.57° in *PpRGTB1* KD in *rgtb2* KO, 87.32° in *PpRGTB2* KD in *rgtb1* KO, and 87.47° in *PpREP* KD) (Figure 3-3D), showing that *P. patens* Rab-GGT two β subunits *RGTB1* or *RGTB2* in *rgtb2* or *rgtb1* knockout background or REP may not be required for sensing the gravity vector and responding to it.

Because mutations in *Arabidopsis RGTB1* lead to de-etiolated or constitutively photomorphogenic phenotypes, loss of apical dominance, and defective shoot growth and gravitropism (Hála et al., 2010), due to impaired phototropic and gravitropic responses, disruption of *P. patens RGTB1* was also expected to lead to alterations in phototropism and/or gravitropism. In contrast to results with *Arabidopsis RGTB1* mutants, *PpRGTB1* KD in *rgtb2* KO lines displayed normal protonemal positive phototropism and caulonemal negative gravitropism, suggesting that the role of this gene is not conserved between *Arabidopsis* and *P. patens* and at least contributes differently to PIN cargo trafficking and associated auxin-mediated plant development. Since the two copies of Rab-GGT β subunits underwent independent gene duplication in the *Arabidopsis* and *P.*

patens (Thole et al., 2014), they may have diverged in function and evolved independently, acquiring different functions. Alternatively, although Rab-GGT KD lines, except *PpRGTA1* KD lines, exhibited normal tropic responses, due to different expression levels in each cell, there may be a threshold for the mutations where only sufficient knockdown impairs the ability to respond to environmental stimuli. Therefore, our data may not have shown an association of loss of Rab-GGT with phototropism or gravitropism defects because of relatively insufficient knockdown levels.

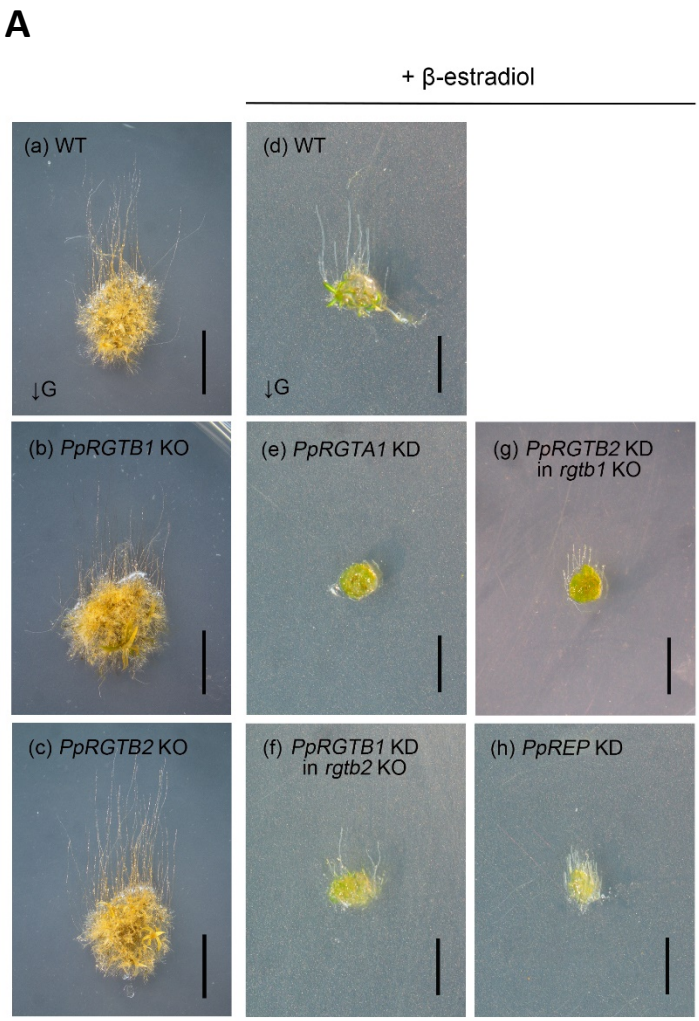

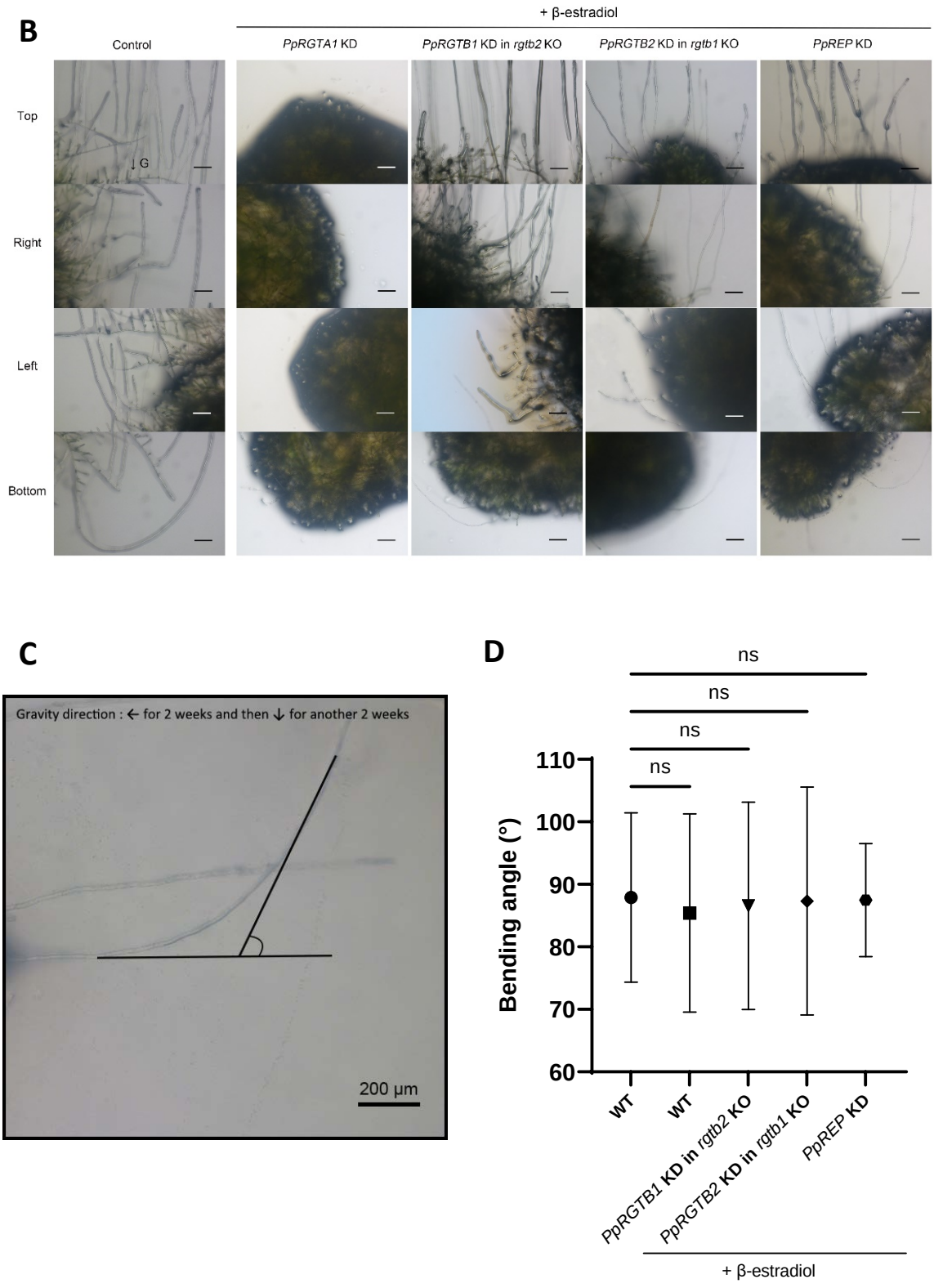

Figure 3-3: Gravitropism assay.

(A) Gravitropic phenotype of colony of WT and Rab-GGT mutants vertically grown in the dark for 4 weeks (a–c) and 2 weeks (d–h). Scale bars = 5 mm. '↓ G' indicates the direction of gravity. (B) Gravitropic phenotypes of caulonemal filaments of WT and Rab-GGT mutants vertically grown in the dark for 2 weeks. Scale bars = 200 μm. (C) Caulonemal filaments were vertically grown in the dark for 2 weeks and then for another 2 weeks with a 90-degree rotation around the gravity direction. The figure represents how the curvature of bending filaments were measured. A filament not bent after a change in the gravity direction was measured as 0 degrees and a filament bent against or towards the final gravity direction was measured as 90 degrees or –90 degrees, respectively. (D) Quantification of bending angles of caulonemal filaments. Data shown are Mean ± SD (n ≥ 25).

Response of Rab-GGT KD lines to exogenous abiotic stress hormones.

Plant growth and development are regulated by crosstalk and a fine balance between phytohormones in response to biotic and abiotic stresses (Schumaker & Dietrich, 1997; Thelander et al., 2005; Decker et al., 2006; Wang & Irving, 2011). An example is the dynamic and complementary actions of the auxin and cytokinin pathways. The antagonistic interactions of auxin and cytokinin control the balance of proliferation and differentiation of meristem cells to maintain apical meristem activity and define branching patterns in shoots and roots (Ioio et al., 2008; Müller & Leyser, 2011; Su et al., 2011). Conversely, auxin and cytokinin act synergically in cell division and growth in plant tissue culture or rapid elongation growth of roots (Yang et al., 2017; Hurný et al., 2020). In *P. patens*, auxin promotes the differentiation of caulonema and rhizoid and the

elongation of stem, and enhances the formation of shoot bud in a cytokinin-dependent manner (Ashton et al., 1979; Decker et al., 2006; Thelander et al., 2017). We examined the responses of the Rab-GGT KD lines to various phytohormones using 1-naphthaleneacetic acid (NAA) as an auxin and 6-benzylaminopurine (BAP) as a cytokinin with varying concentrations (0, 0.1, 1, and 10 μM) to determine if the phenotypic and developmental deviations described in chapter II are the result of hormonal imbalances.

Exogenously applied auxin (NAA) cannot stimulate caulonema differentiation in Rab-GGT KD lines, indicating that their response towards the auxin is altered

Auxin, one of the classical phytohormones, is a key signaling molecule that controls numerous developmental decisions and environmental responses, such as cell division, cell expansion, vascular tissue differentiation, root initiation, phototropic and gravitropic responses, apical dominance, leaf senescence and abscission, fruit development including fruit set and growth, ripening and abscission, parthenocarpy, flowering and sex expression, etc. (Davies, 2010; Wang & Irving, 2011). The establishment and maintenance of the cellular optimal concentrations of indole-3-acetic acid (IAA), the most studied auxin in plants, are regulated throughout plant development at multiple levels including biosynthesis, transport, perception, and signal transduction. There are several regulation pathways that contribute to different spatiotemporal patterns of auxin within tissues at different developmental stages, for different purposes and in response to different stimuli (Eklund et al., 2010; Su et al., 2011).

For IAA biosynthesis, two major pathways have been proposed in *Arabidopsis*: the tryptophan (Trp)-independent and Trp-dependent pathways. In the Trp-independent

pathways, probable precursors are indole-3-glycerol phosphate or indole, but not much is known about the biochemical pathway to IAA. The Trp-dependent pathways include the indole-3-acetamide (IAM) pathway, the indole-3-pyruvic acid (IPA) pathway, the tryptamine (TAM) pathway, and the indole-3-acetaldoxime (IAOx) pathway. Several studies have demonstrated that the TRYPTOPHAN AMINOTRANSFERASE OF ARABIDOPSIS (TAA) family of aminotransferases catalyzes the conversion of L-Trp to IPA, and then the YUCCA (YUC) flavin-containing monooxygenase family functions in the conversion of IPA to IAA (Mashiguchi et al., 2011; Stepanova et al., 2011). The SHI/STY family proteins have been shown to induce the activity of the auxin biosynthesis gene YUC4 in lateral organs of *Arabidopsis* (Eklund et al., 2010).

Auxin polar transport is required for the formation of auxin concentration gradients and directional auxin flows, which are essential for developmental pattern formation, morphogenesis, and directional growth in response to vectorial cues in plants. In *Arabidopsis*, this process is mediated by several families of auxin carriers including PIN-FORMD (PIN) proteins (PINs, auxin efflux carriers), AUXIN RESISTANT 1 (AUX1)/LIKE AUX1 (LAX) proteins (auxin influx facilitators), and MULTIDRUG RESISTANCE (MDR)-p-glycoprotein (PGP) proteins (Gao et al., 2008).

As for auxin signaling, when the cellular auxin concentration is low, the AUXIN/INDOLE-3-ACETIC ACID (Aux/IAA) transcriptional repressor binds to the AUXIN RESPONSE FACTOR (ARF) protein, repressing transcription of auxin responsive genes. When the auxin concentration is increased to a certain level, IAA binds to the TRANSPORT INHIBITOR REPONSE 1 (TIR1, or auxin-related F-box (AFB); TIR1/AFB) auxin receptor and acts as a “molecular glue” between TRI1/AFB and

Aux/IAA proteins. The ubiquitin ligase SCF binds to this complex and the ubiquitinated Aux/IAA is degraded, releasing the ARF proteins to activate the transcription of a plethora of auxin-induced genes (Su et al., 2011; Kou et al., 2022).

Genes involved in auxin biosynthesis, transport, perception, and signal transduction in *Arabidopsis* have been demonstrated to be present also in *P. patens*, implying the emergence of this machinery during the early colonization of land by plants (Rensing et al., 2008; Eklund et al., 2010; Zhao, 2010). In *P. patens*, auxin is important not only for the induction of chloronema to caulonema transition but also for maintenance of caulonemal characteristics, retaining its increased concentration after the identity switch (Ashton et al., 1979; Thelander et al., 2017). It has been shown through loss-of-function and gain-of-function analyses that the accelerated effect of auxin on the chloronema-to-caulonema transition is dependent on SHI/STY proteins involved in auxin biosynthesis (Eklund et al., 2010), PIN auxin efflux carriers involved in auxin transport (Viaene et al., 2014), and the TIR1/AFB–Aux/IAA–ARF complex involved in auxin perception and signaling (Prigge et al., 2010). Auxin levels and the chloronem-to-caulonema transition are suppressed in either of two *PpSHI* genes (*PpSHI1, PpSHI2*) knockout (KO) lines but accelerated in *PpSHI1* overexpression (OE) lines (Eklund et al., 2010). Long *PpPIN* KO shows increased cellular auxin levels and earlier transition to caulonema identity following the protonemal regeneration of protoplasts, whereas its OE shows increased auxin export to the surrounding medium and maintenance of choloronema identity. In addition, *PpPIN* genes are highly expressed in the apical tip cells, suggesting an acropetal auxin transport and its accumulation in and drainage from tip cells. These data together indicate the function of PpPIN as auxin trapping and the

need for acropetal PpPIN-mediated auxin transport in generating auxin levels for initiating proper caulonema differentiation (Viaene et al., 2014). *Ppaux/iaa* KO becomes completely insensitive to auxin (constitutive auxin response) and is unable to develop caulonema. Also, *Pp*ARFb4 OE in an *aux/iaa* KO background suppresses the constitutive auxin phenotype of *Ppaux/iaa* KO but still cannot undergo caulonema differentiation even when treated with exogenous auxin. *At*ARF1 OE in an *aux/iaa* KO background exhibits similar effects. These results suggest ARF's independent activity as a repressor, its conserved role between *Arabidopsis* and *P. patens,* and the requirement of Aux/IAA function for developmental transition (Lavy et al., 2016).

Additionally, the auxin-induced genes *ROOT HAIR DEFECTIVE SIX-LIKE (RSL)*, encoding basic helix–loop–helix (bHLH) transcription factors, positively regulates the development of root-hair in *Arabidopsis* and both rhizoid and caulonema in *P. patens* (Tam et al., 2015). Caulonema differentiation is enhanced in *PpRSL1* and *PpRSL2* OE lines but inhibited even in the presence of exogenous auxin in *Pprsl1/rsl2* double KO lines, suggesting the need for these genes for proper auxin induction and cell fate shift (Jang & Dolan, 2011). *LOTUS JAPONICUS ROOTHAIRLESS1-LIKE (LRL)* genes, encoding another type of bHLH transcription factors, are also known to be involved in caulonema development (Tam et al., 2015).

Mutations in *Arabidopsis RGTB1*, the β-subunit of Rab-GGT, lead to auxin-related phenotypic abnormalities, such as loss of apical dominance, severely disrupted shoot growth, and gravitropic defects, as a potential consequence of defective auxin gradient formation in the developing tissues and organs (Hála et al., 2010; Rojek et al., 2021). In contrast to *AtRGTB1* KO, *PpRGTB1* KD showed normal tropic responses,

indicating (Figure 3-2A f, g and 3-3A f, g) that the effects of insufficient prenylation of Rab-GTPases may differ between *Arabidopsis* and *P. patens*. Since the auxin-mediated differentiation of chloronema into caulonema was greatly reduced in the Rab-GGT KD lines, we applied varying concentrations of auxin (0.1, 1, and 10 μM) in an attempt to artificially induce caulonemal formation to examine whether the response towards auxin is altered (Figure 3-4).

Without β-estradiol induction, all lines grown on BCD supplemented with NAA for 3 weeks exhibited similar morphological changes, such as inhibition of colony growth, reduced number of emerging gametophores, stimulation of bud formation, and loss of green color (Figure 3-4, A and C). The inhibitory effect was dose-dependent (Figure 3-4B-1), indicating toxicity of NAA. NAA-induced caulonema-like or rhizoid-like protonema differentiation was clearly observed at 0.1 μM in WT (Figure 3-4C left red box) and all un-induced Rab-GGT KD lines (data not shown), but its proliferation was decreased with increasing NAA concentration. All lines including WT and KD lines at 10 μM appeared to be dead or dying.

When with β-estradiol induction, NAA-induced caulonema formation was observed in WT at 0.1 μM NAA (Figure 3-4C right red box), but the effect was reduced compared to that without β-estradiol induction. However, in the case of Rab-GGT KD lines at 0.1 and 1 μM NAA, little effect of NAA on colony growth inhibition and caulonema differentiation was observed, as there was no significant morphological difference in colony diameter (Figure 3-4B-2) and amount of protruding caulonemal filaments (Figure 3-4C) between auxin-treated and untreated ones. Since 10 μM NAA resulted in complete growth inhibition, there was no significant difference between WT

and all induced Rab-GGT KD lines (P = ns), except for *PpRGTA1* KD lines. *PpRGTA1* KD lines could not withstand 3 weeks of β-estradiol induction. Low response or resistance to the effects of NAA of Rab-GGT KD lines may be due to impaired polar auxin transport, and thus auxin accumulation resulting from blocked export may have rendered the mutants insensitive to additional exogenous auxins.

However, when comparing the colony diameter according to different concentrations of NAA with β-estradiol induction between WT and each Rab-GGT KD line, there was a significant difference at 0 μM NAA (****P < 0.0001) but no significant difference at all NAA concentrations compared with WT (P = ns). This suggests that although the colony growth of the Rab-GGT KD lines was suppressed to some extent similar to WT by NAA, it may seem less sensitive to NAA due to their colony growth at 0 μM NAA greatly inhibited by β-estradiol treatment, which was used as a comparison to examine sensitivity. It is not clear whether the inhibition of colony growth is caused by β-estradiol or NAA, but the green color is lost as the concentration of NAA increases, indicating that they are responding to NAA. Since NAA-treated Rab-GGT KD lines except for *PpRGTA1* KD lines displayed inhibited colony growth, bud formation, and normal tropic responses, this suggests that the overall auxin machinery was not disrupted, but a sufficient level of auxin to activate caulonema differentiation may not be produced or accumulated in the correct sites. Another possibility is that, like the *RSL* and *LRL* genes (Tam et al., 2015), the activity of the genes encoding Rab-GGT may be required for auxin-induced caulonema differentiation, therefore insufficient expression levels may have blocked the transition from chloronema to caulonema. Future studies will focus on the measurement of endogenous auxin levels in the protonemal tissue of the Rab-GGT

KD lines to investigate whether the perturbed caulonema differentiation is due in part to the effect by altered cellular auxin levels, and the quantification of auxin levels exported to the medium by growing them in liquid BCD medium (as described in Viaene et al., 2014) to assess their auxin transport capabilities.

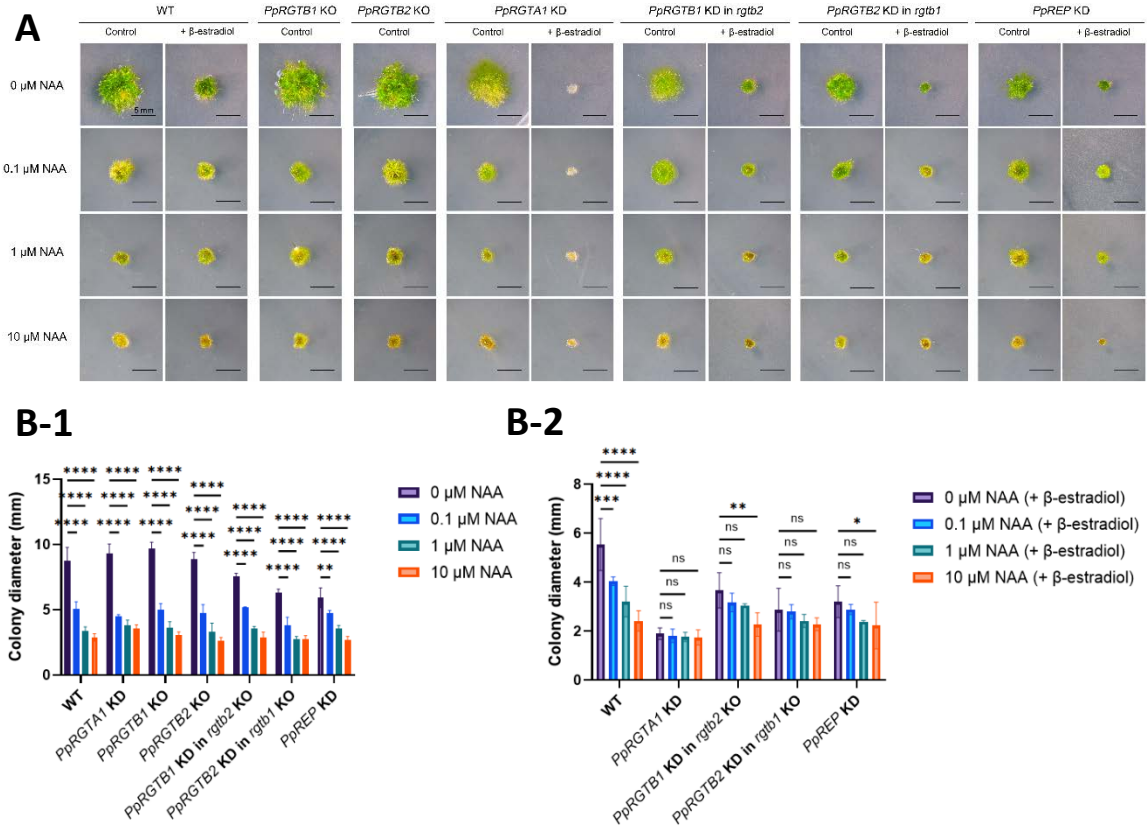

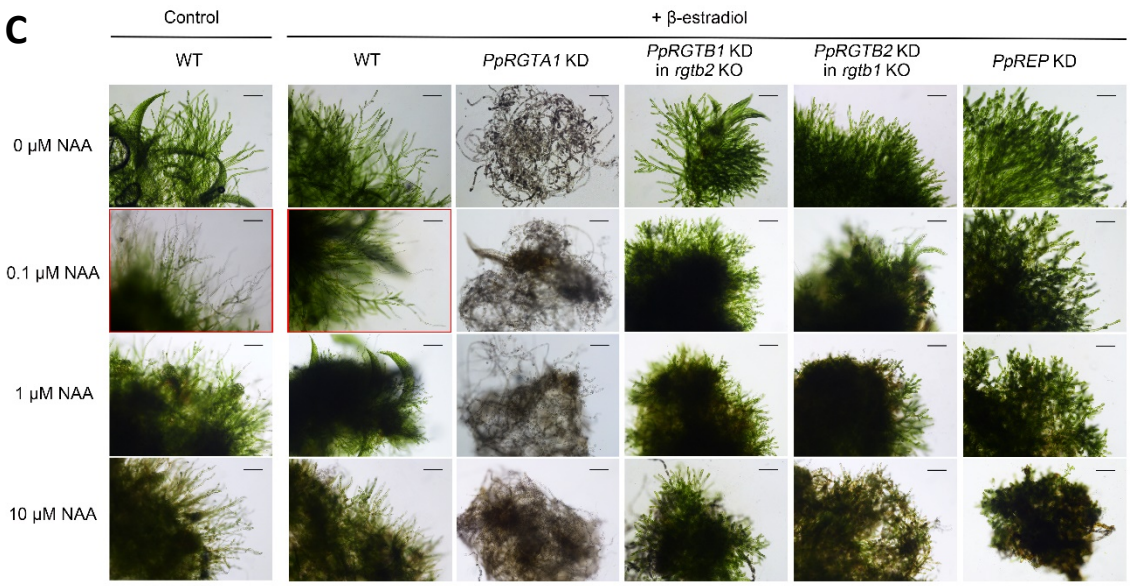

Figure 3-4: NAA treatment assay.

(A) Representative colony morphology of WT and Rab-GGT KD lines on BCD medium supplemented with different concentrations of NAA for 3 weeks. Scale bars = 5 mm. (B) Size of colonies of each β-estradiol un-induced (B-1) & induced (B-2) strain measured as diameter in millimeters. The data shown are the Mean ± SD of 4 individual colonies per line. (C) Magnification of filament of WT and knockdown lines treated with NAA for 3 weeks. Red boxes indicate NAA-induced caulonema-like or rhizoid-like protonema differentiation. Scale bars = 200 μm.

Rab-GGT may be not involved in cytokinin signaling

Like auxin, cytokinin is also a critical hormone responsible for controlling crucial aspects of plant growth and development. For instance, cytokinins regulate cell division mainly in shoots and roots, axillary bud differentiation and outgrowth (apical dominance), delay of leaf senescence (plant aging) and chlorophyll degradation, seed germination and dormancy, nutrition mobilization, plant-pathogen-interactions, etc.

(Skoog & Tsui, 1948; Inoue et al., 2001; Sakakibara, 2006; Akhtar et al., 2020). In *P. patens*, exogenously applied cytokinin inhibits growth by suppressing both the formation of chloronema and caulonema in a concentration-dependent manner, with a greater effect as the concentration increases. Cytokinins at low concentrations accelerate bud induction, while those at higher concentrations provoke the formation of a callus-like bud, unorganized cell masses (Ashton et al., 1979).

As expected, after 3 weeks of BAP treatment without β-estradiol induction, the colonies of both WT and all Rab-GGT mutants were significantly smaller and less filamentous compared to those without BAP treatment with the greatest inhibition at 10 μM ($P < 0.0001$) (Figure 3-5). In the WT with or without β-estradiol induction, BAP reduced the sizes of colonies, and no significant difference was found between different concentrations (P = ns between 0.1 and 1 μM, 1 and 10 μM, and 0.1 and 10 μM) (Figure 3-5B-1 and 3-5B-2). Not surprisingly, BAP promoted the formation of callus-like buds, thus no or abnormal gametophores were observed (Figure 3-5C). Except for *PpRGTA1* KD lines, with unstable viability upon β-estradiol induction, all other Rab-GGT KD lines reacted similarly, showing inhibited growth of the colonies and callus-like structures. Therefore, high levels of Rab-GGT are not required for cytokinin signaling.

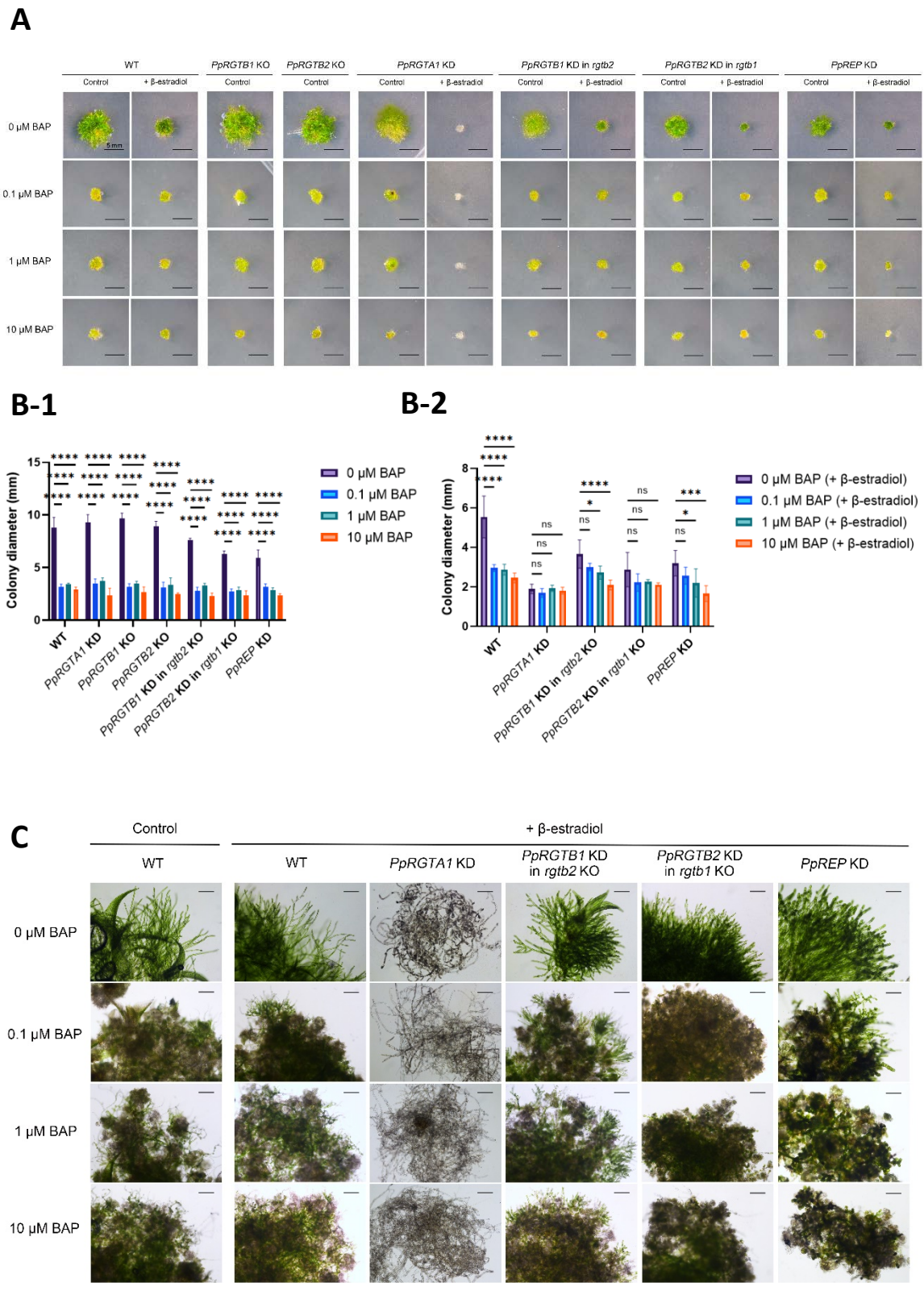

Figure 3-5: BAP treatment assay.

(A) Representative colony morphology of WT and Rab-GGT KD lines on BCD medium supplemented with different concentrations of BAP for 3 weeks. Scale bars = 5 mm. (B) Size of colonies of each β-estradiol un-induced (B-1) & induced (B-2) strain measured as diameter in millimeters. The data shown are the Mean ± SD of 4 individual colonies per line. (C) Magnification of filament of WT and knockdown lines treated with BAP for 3 weeks. Scale bars = 200 μm.

Rab-GGT KD lines are hypersensitive to exogenously applied ABA

ABA is a ubiquitous plant hormone that plays critical roles in the regulation of plant response and tolerance to various abiotic stresses. Due to plants' immobile nature, the ability to respond to environmental stresses such as desiccation, salt, and cold, UV radiation, and pathogen attack may have had a pivotal role in the colonization of land (Wang et al., 2010; Sun et al., 2020). ABA is integrated into a complex signaling network that modulates embryogenesis, germination, cell division, seed maturation and dormancy, root development, stomatal aperture, and stress-responsive gene expression leading to improved plant adaptation (Brock et al., 2010; Cutler et al., 2010; Yang et al., 2016). The ABA signal transduction pathway is comprised of PYRABACTIN RESISTANCE 1 (PYR1)/PYR1-LIKE (PYL)/REGULATORY COMPONENT OF ABA RECEPTOR (RCAR), SNF1-RELATED PROTEIN KINASE 2 (SnRK2), and Clade A TYPE 2C PROTEIN PHOSPHATASE (PP2C). In the presence of ABA, ABA signals are perceived by a PYL/PYL/PCAR receptor, which negatively regulates PP2C. PP2C normally represses ABA signaling by binding to SnRK2; thus, bunding of ABA results in the release of SnRK2. The activated SnRK2 phosphorylates substrate proteins such as ion

channels, transcription factors (bZIP factors, MYB, and WRKY, etc.), and enzymes (NADPH oxidases), triggering ABA responses. Physiological and molecular perception and responses to ABA appear to be conserved in *P. patens* and *Arabidopsis* (Wang et al., 2010; Sun et al., 2020; Lohani et al., 2022). For instance, significantly attenuated ABA response (complete ABA insensitivity) of *P. patens* lacking PpSnRK2A/PpOST1 (ABA-regulatory protein kinase OPEN STOMATA 1) or snrk2a/b/c/d (subclass III four SnRK2 genes) is similar to *Arabidopsis* lacking homologous single snrk2.6/ost1 or triple snrk2.2/2.3/2.6, respectively. The disruption of OST1 in *Arabidopsis* is complemented by (is rescued by substitution with) a *P. patens* homolog, PpOST1-1, and the disruption of *P. patens* SnRK2 is complemented by *Arabidopsis* subclass III SnRK2s, showing functional conservation of SnRK2 in ABA signaling (Chater et al., 2011; Shinozawa et al., 2019). In addition to SnRK2 itself, its phosphorylation targets and regulatory proteins are also known to be highly conserved (Sun et al., 2020).

Since the deletion of the β-subunit of two other known protein prenyltransferases in *Arabidopsis*, protein farnesyl transferase (PFT) *era1* mutants or protein geranylgeranyl transferase I (PGT) *ggb* mutants, results in ABA hypersensitivity (Pei et al., 1998; Johnson et al., 2005), we examined whether the sensitivity of *P. patens* Rab-GGT mutants to ABA is altered to determine whether the role of prenylation in ABA responses is conserved between different enzymes and among land plants. In *P. patens,* exogenous application of ABA causes growth retardation associated with protonemal morphological changes leading to the formation of brachycytes and tmema cells, acquiring an increased freezing, hyperosmosis, and dehydration tolerance (Goode, et al., 1993; Arif et al., 2019). Therefore, we also investigated the morphology of *P. patens* Rab-GGT mutants to see if

they still form such cells upon ABA treatment, and examined their survival rate after ABA pretreatment, complete drying, and rehydration to see if the acquisition of desiccation tolerance is impaired or enhanced.

All *P. patens* Rab-GGT mutants, with or without β-estradiol induction, reacted to ABA, as after 2 weeks of treatments with 1, 10, 50 μM ABA, they displayed reduced colony size at all concentrations and formed brachycytes in the protonemal tissue from 10 μM treatment (Figure 3-6). The number of brachycytes formed increased with increasing concentration and duration of ABA application (Figure 3-6A). At 50 μM ABA, the highest concentration tested, almost complete growth inhibition was observed in all samples due to cell division cessation but showed the most brachycytes out of all treatments. Compared to WT, the Rab-GGT β subunit KO mutants did not differ statistically in colony size (Figure 3-6B-1) and morphologically in the formation of brachycytes (Figure 3-6A). Since brachychytes develop from chloronema (Arif et al., 2019), the Rab-GGT KD lines that had relatively more chloronema than WT due to impaired chloronema to caulonema conversion resulted in more brachycytes. Upon induction of β-estradiol (Figure 3-6B-2), colony size of all Rab-GGT KD lines was reduced at 1 μM ABA, the lowest concentration tested, but this appears to be the effect of knockdown and not of ABA, because the protonemal morphology was indistinguishable from 0 μM ABA, without forming brachycytes. Therefore, we focused on comparisons between WT and Rab-GGT KD lines at 10 and 50 μM ABA. At 10 μM ABA, there was statistically no significant difference in colony size (P = ns), but more, larger, spherical brachycytes were observed in Rab-GGT KD lines, suggesting a hypersensitivity to the effects of ABA possibly due to changes in endogenous ABA levels. At 50 μM ABA, no

difference was seen since both WT and Rab-GGT mutants exhibited fully inhibited growth and numerous brachycytes. Our next aim is to determine endogenous ABA levels in Rab-GGT KD lines to investigate whether altered (possibly elevated?) ABA levels contribute partially to the swollen cellular phenotype that appears even in the absence of ABA and are responsible for having more pronounced brachycytes at relatively low concentrations.

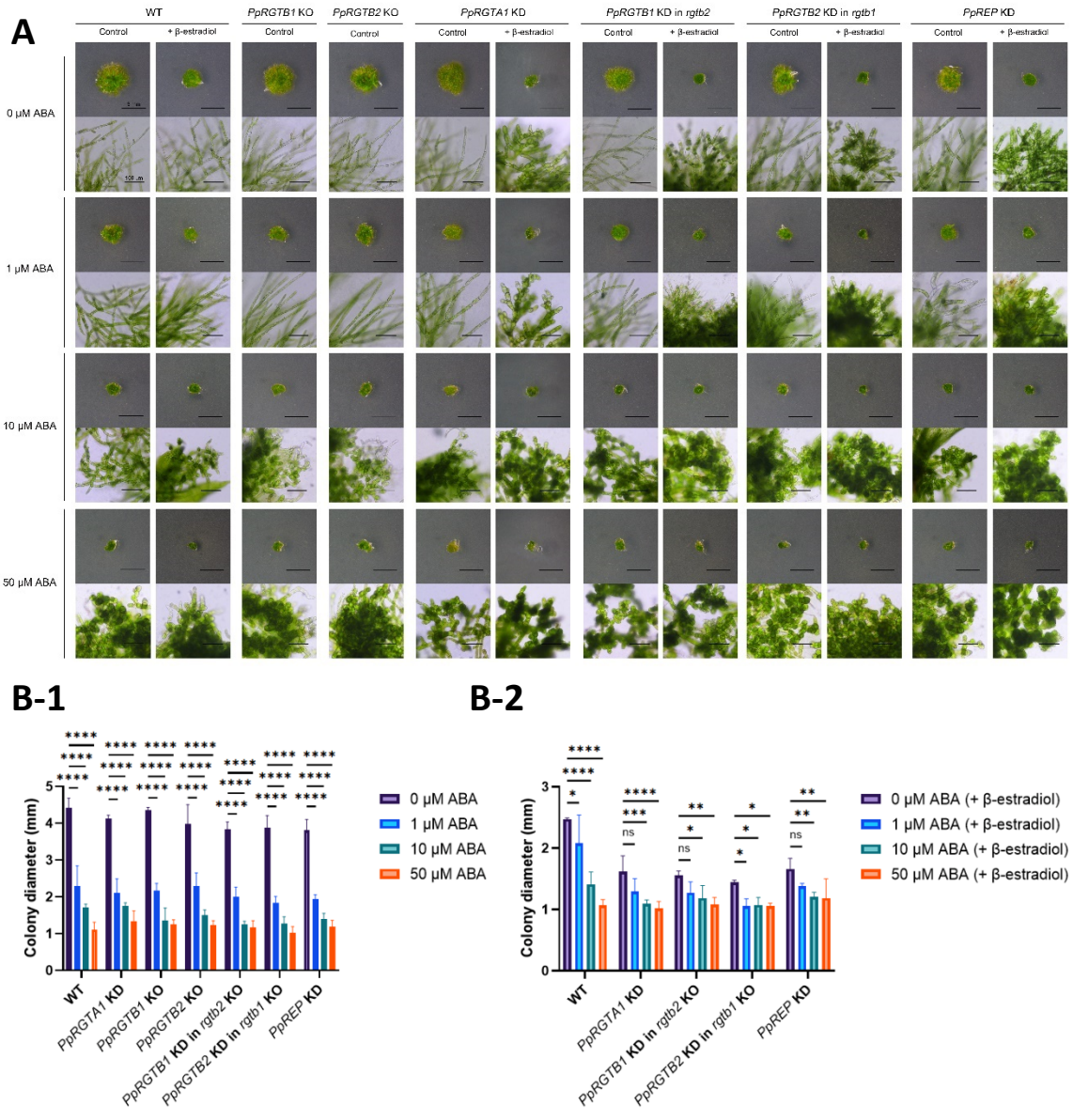

Figure 3-6: ABA treatment assay.

(A) Representative colony (scale bars = 3 mm) & filament (scale bars = 100 μm.) morphology of WT and Rab-GGT KD lines on BCD medium supplemented with different concentrations of ABA for 2 weeks. (B) Size of colonies of each β-estradiol un-induced (B-1) & induced (B-2) strain measured as diameter in millimeters. The data shown are the Mean ± SD of 4 individual colonies per line.

Survivability of Rab-GGT KD lines exposed to desiccation is enhanced compared to wild type after pretreatment with only 1 μM ABA, but their recovery rates are lower after pretreatment with 50 μM ABA

In contrast to homeohydric vascular plants, which have a cuticularized epidermis to maintain water content, roots to acquire water, and vascular tissue to distribute water internally, *P. patens* are poikilohydric, where water content is dependent upon its environmental availability, and have aerial surfaces adapted to absorb and diffuse water rapidly and directly from the surrounding habitat across the cell membrane. (Proctor & Tuba, 2002; Mishler & Oliver, 2018). Consequently, *P. patens* has evolved to possess cellular protection strategies for considerable tolerance to dehydration, ranging from moderate short-term dehydration to long-term complete desiccation (Oliver, 2005; Holzinger & Karsten, 2013). *P. patens* protonemal tissue can endure water loss up to 92% on a fresh weight basis, but ABA pretreatment enables it to survive complete desiccation that it would not normally tolerate (Arif et al., 2019).

Rab-GGT KD lines were pretreated with varying concentrations (0, 1, 10, and 50 μM) of ABA for 24 hours, dehydrated for 24 hours, and rehydrated by placing back on

regular growth medium and their recovery rate was measured after 2 weeks by analyzing chlorophyll content. All Rab-GGT mutants were able to form brachycytes upon ABA treatments, and the four KD lines were hypersensitive to ABA as more brachycytes were observed at 10 μM, although there was no significant difference in colony diameter compared to WT (Figure 3-6). Since brachycytes act as vegetative diaspores that are resistant to desiccation and freezing (Arif et al., 2019), we expected that the enhanced response to ABA of the Rab-GGT KD lines would increase survivability from complete desiccation after 24-hour ABA pretreatment. When without β-estradiol induction, overall, none with 0 μM ABA pretreatment, very few or no cells with 1 μM ABA pretreatment, and many or most cells with 10 and 50 μM ABA pretreatment survived (Figure 3-7A). The survival rate of Rab-GGT β subunit KO mutants were statistically indistinguishable from that of WT at all concentrations (Figure 3-7B). When with β-estradiol induction, pretreatment with 10 and 50 μM ABA was also sufficient to enable all Rab-GGT KD lines to resume growth upon rehydration; however, unexpectedly their survival rate was reduced at 50 μM ABA compared to WT (Figure 3-7B). This insensitivity may be due to the already weakened viability caused by the knockdown effect induced by β-estradiol or 24-hour of ABA pretreatment may not be sufficient to acquire desiccation tolerance. Interestingly, all Rab-GGT KD lines show a higher survival rate after only a 1 μM ABA pretreatment compared to WT and Rab-GGT β subunit KO mutants. This assay will be repeated with a wider range of pretreatment concentrations and periods.

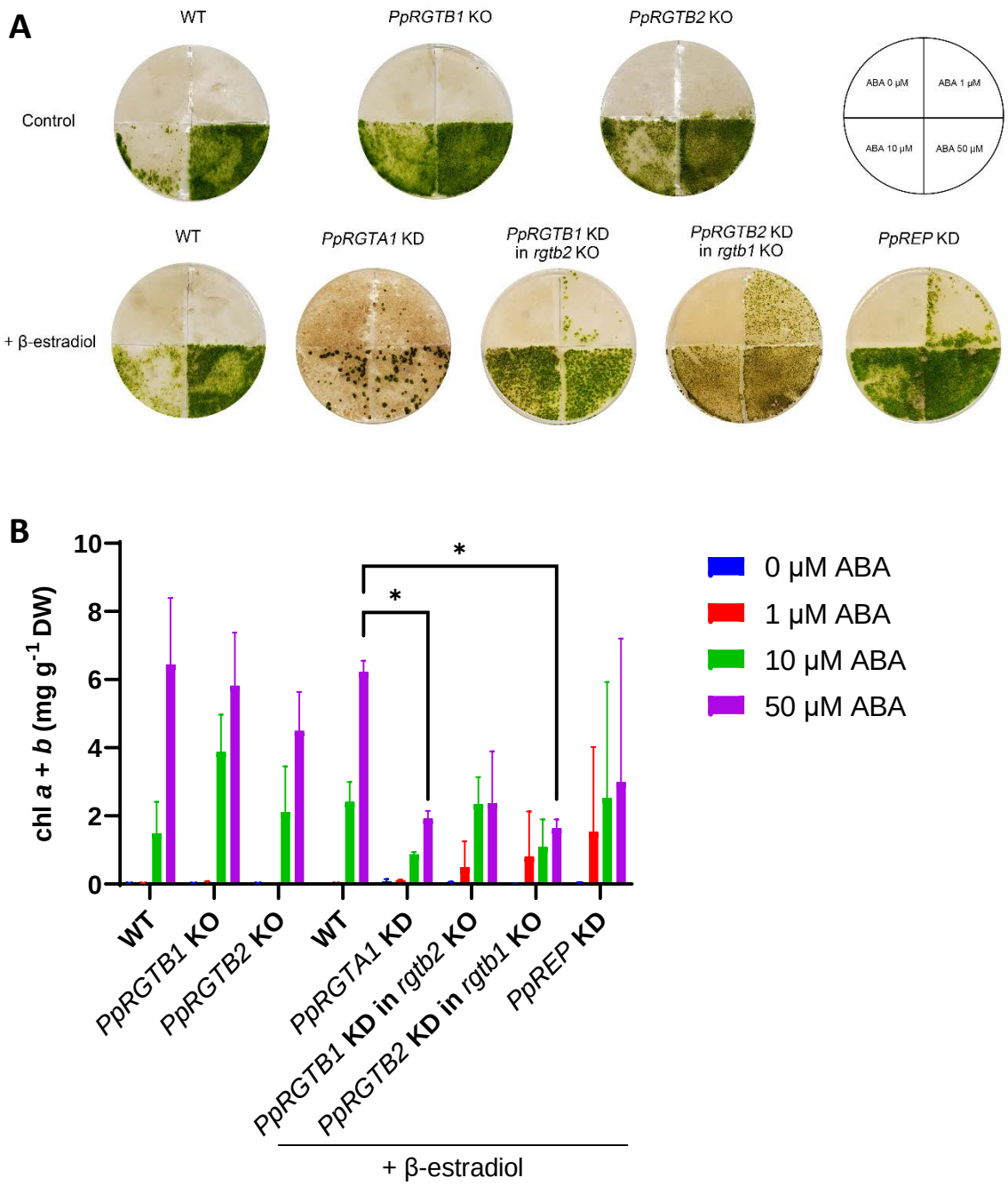

Figure 3-7: Desiccation tolerance assay.

(A) Representative images of recovered ABA-treated, dehydrated, and rehydrated WT and Rab-GGT mutants. (B) Chlorophyll content (mg chorophyll / g dry weight) after 2 weeks of recovery.

CHAPTER IV

CONCLUSIONS

Prenylation is a key post-translational modification involved in a variety of plant growth and developmental processes, such as cell fate specification, cell differentiation, polar cell elongation, and hormonal and environmental responses (Thole et al., 2014). Research on prenylation in plants so far has been focused primarily on the angiosperm *Arabidopsis*, which exhibits a relatively mild phenotype upon prenylation deficiency. Our initial results with *P. patens* showed many conserved prenylation mechanisms and functions between disparate species, as well as additional roles for cell adhesion and viability. The purpose of this study was to carry out the molecular and functional characterization of Rab-GGT, whose function has not yet been reported in non-angiosperm plant lineages, using *P. patens*, a model system of superior utility for extensive comparative and evo-devo studies.

Of the Rab-GGT components in plants, only mutations in β subunits, *RGTB1* and *RGTB2*, have been reported, and only in *Arabidopsis*, and mutations in either of the two α subunits, *RGTA1* or *RGTA2*, have not been reported in any plant. Non-viable double *RGTB* mutants with total RGTB deficiency in both *Arabidopsis* and *P. patens* showed overlapping function in that Rab-GGT function is an absolute requirement for plant viability (Shi et al., 2016). In *P. patens*, the complete loss of Rab-GGT activity appeared

to be lethal (Thole et al., 2014), thus viable knockdown mutants that partially lost Rab-GGT activity were generated, and their morphology and development were analyzed.

Since the functional Rab proteins geranylgeranylated by Rab-GGT are engaged in intracellular vesicle transport and membrane trafficking (Pereira-Leal and Seabra, 2001; Leung et al., 2006), it was not surprising that alterations in the enzymatic activity of Rab-GGT resulted in Rab geranylgeranylation deficiency, causing many phenotypic deviations and interfering with physiological processes. The major phenotypic defect of *P. patens* Rab-GGT KD lines was compromised cell morphogenesis and polarity establishment and maintenance defects, resulting in retarded growth lacking proper elongation of apical cells, reduced colony diameter and emerging gametophore number resulting from reduced or incomplete caulonema differentiation, abnormally shaped cells by swelling and disoriented cell division, defective bud development, and defects in vesicle transport and cytokinesis. The importance of Rab-dependent vesicle trafficking in tip-growing cells in *P. patens* demonstrated by these morphological aberrations was consistent with the roles of Rab proteins and *RGTB1* and *RGTB2* genes in polarized cell (e.g., pollen tubes and root hairs) growth in *Arabidopsis* (Gutkowska et al., 2015). Based on these results, we could confirm that the Rab-GGT activity in tip growth is conserved in two different species.

However, there were some differences: although single *RGTB* mutants with partial RGTB deficiency are viable in both species, exhibiting functional redundancy, the functions of *RGTB1* and *RGTB2* compensate for each other partially in *Arabidopsis* and fully in *P. patens* (Hála et al., 2010; Gutkowska et al., 2015, Shi et al., 2016). The *PpRGTB1* and *PpRGTB2* KO mutants were indistinguishable from WT not only in terms

of morphology and development, but also in environmental and hormonal responses. In contrast to the *AtRGTB1* KO mutants that showed loss of apical dominance and photomorphogenic and gravitropic defects (Hála et al., 2010), processes facilitated by auxin, knockdown of *PpRGTB1* in a *rgtb2* knockout background (or vice versa) or *PpREP* displayed both normal phototropic and gravitropic responses, but exhibited altered response towards exogenously applied auxin, as exogenous auxin-induced chloronema-to-caulonema transition was not observed. These results indicate that, although there may be possible auxin transport defects in both species, Rab-GGT may work differently in different species. Interestingly, *P. patens* Rab-GGT KD lines were hypersensitive to exogenously applied ABA, like *PLP* and *ERA1* mutants in *Arabidopsis* (Cutler et al., 1996; Running et al., 2004), and showed enhanced ABA-induced desiccation tolerance after pretreatment with relatively low ABA. In the future, determination of endogenous levels of auxin and ABA in Rab-GGT KD lines will provide a great opportunity to clarify the involvement of biological function of Rab-GGT in various molecular mechanisms related to plant stress responses.

In addition, Rab-GGT KD in *P. patens* did not affect the carbohydrate composition of the cell wall, revealing an intact mechanism involved in the production of cell wall components. Since *P. patens* Rab-GGT KD lines displayed disrupted polarized cell expansion and defective cytoskeletal organization, the status of differentiation and polarity will be traced indirectly by immunolabeling cell wall components using antibodies and detecting their subcellular localization to determine if the transport or deposition process of cell wall components is affected.

As all Rab-GGT components are essential for *P. patens* survival, there were some limitations in the experiment, such as unstable viability, inconsistent growth rates, and changes in phenotype severity, due to the significantly attenuated health condition upon β-estradiol-induced knockdown compared to WT and un-induced lines. In particular, *PpRGTA1*, a single copy of the Rab-GGT α subunit in *P. patens*, appeared to have a greater contribution to viability than other components. In *Arabidopsis*, the α subunit duplicated independently, after the split in the two lineages, leading to the presence of an additional α subunit (Thole et al., 2014), though RGTA2 does not show prenylation activity *in vitro* (Shi et al., 2016). It will be interesting if RGTA1 from *Arabidopsis* can complement the *PpRGTA1* KD and restore the WT phenotype, indicating functional conservation.

This dissertation reported some functional similarities and differences of Rab-GGT between two evolutionary distant species *P. patens* and *Arabidopsis.* The partially overlapping functions may be due to the roles of Rab-GGT in plant development, which, like other prenyltransferase enzymes, may have arisen early in the plant lineage as a result of evolutionary changes that occurred during terrestrial colonization. However, as the genes of *P. patens* have evolved and duplicated independently of those of *Arabidopsis* as in the case of RGTB (Thole et al., 2014), *P. patens* may acquire extra independent tissue-specific roles that we have not yet elucidated. Further investigation needs to be performed to support this hypothesis.

CHAPTER V

STERILIZATION SYSTEMS VIA SIMULATED ROBOTIC UV-C IRRADIATION AND DNS SURFACES ARE HIGHLY EFFECTIVE IN INACTIVATION OF MICROORGANISMS AND SHOW PROMISE IN EXTENSIVE APPLICATIONS

Introduction

Severe acute respiratory syndrome coronavirus 2 (SARS-CoV-2) is a novel virus that was first reported in Wuhan, China, and is the causative agent of the COVID-19 global pandemic (Gorbalenya, et al., 2020; Lai et al., 2020). The pandemic disrupted nearly all aspects of life, including scientific research. Because of the university-mandated limitations on non-pandemic related research beginning in March 2020 and lasting for several months, and in an effort to contribute to the global response to the pandemic, I undertook COVID-19 related projects reported here.

SARS-CoV-2 belongs to the genus of β coronavirus; it is an enveloped positive-sense single-stranded RNA virus with four structural proteins, spike (S), envelope (E), membrane (M), and nucleocapsid (N) proteins, and nonstructural proteins, that include 3-chymotrypsin-like protease, papain-like protease, and RNA-dependent RNA polymerase (Chan et al., 2020; Naqvi et al., 2020). The S protein, the distinctive spike structure on the surface of the virus, plays a key role in the attachment of the virus to the host cell receptor angiotensin-converting enzyme 2 (ACE2), facilitating viral cell entry into the host cell (Huang et al., 2020). The E protein mediates virus assembly, budding,

morphogenesis, and trafficking (Ruch & Machamer, 2012; Verdiá-Báguena et al., 2012). The M protein is the core membrane protein responsible for the shape of the virus envelope and promotes the completion of viral assembly (Schoeman & Fielding, 2019). The N protein binds to the viral RNA and constitutes the nucleocapsid, providing protection to the viral genome (McBride et al., 2014). When the S protein binds to the host cell receptor ACE2, access of the viral RNA genome to the host cell cytosol is accomplished by transmembrane protease serine 2 (TMPRSS2) located on the host cell membrane, followed by fusion of the viral and cellular membranes. After the viral entry via receptor-mediated endocytosis, the translation of the replicase gene from the virion genomic RNA and assembly of the viral replicase complexes occur. Viral RNA synthesis then follows, including viral genomic replication and transcription of sub-genomic RNA, which serves as mRNAs encoding the four structural proteins, as well as several accessory proteins. The viral structural proteins are translated and translocated into the endoplasmic reticulum (ER) and transit through the ER-to-Golgi intermediate compartment (ERGIC), where viral genomic RNA encapsidated by N protein results in budding into the lumen of secretory vesicular compartments. After viral assembly, mature virions are transported to the cell surface and then released from the infected cell via exocytosis (Wang et al., 2020; V'kovski et al., 2020). Damage to these viral proteins and genome results in SARS-CoV-2 inactivation and loss of infectivity (Lo et al., 2021; Matsuura et al., 2021).

Recent studies have shown that SARS-CoV-2 is transmitted rapidly through aerosols and contaminated surfaces and remains infectious from hours to days after being applied on different materials, such as stainless steel, plastic, and copper, emphasizing the

importance of environmental disinfection to limit the spread of SARS-CoV-2 (van Doremalen et al., 2020). Because of its strong contagious ability and surface stability, non-contact disinfection technology through ultraviolet (UV) radiation and antimicrobial surfaces have been in the spotlight. Exposure to UV light is a commonly used direct antimicrobial approach for pathogenic microorganisms (Chang et al., 1985). Particular UV light at a wavelength of 254 nm (UV-C) is a known powerful disinfectant for inactivating enveloped viruses such as SARS-CoV-2 (Lo et al., 2020; Heilingloh et al., 2021). The mechanism of UV-C inactivation of microorganisms is to trigger the formation of dimers in RNA (uracil and cytosine) and DNA (thymine and cytosine), which cause a malfunction in transcription, translation, and replication of DNA and lead to bacterial cell death and viral inactivation (Pfeifer et al., 2005; utler & Zimmerman, 2011; Dai et al., 2012). However, due to the serious health hazards that UV-C presents from direct exposure to human eyes and skin, the UV-C disinfection process can only be employed in absence of humans by well-instructed and trained operators (Trevisan et al., 2006; Zaffina et al., 2012). Therefore, the use of UV-C sanitizing robots is an attractive solution for contactless immediate disinfection and for the cost-saving automatic and remote capabilities. In addition, considering the cleaning frequency that varies depending on the type of surface and how often the surface is used, and neglected surfaces that may occur due to the blocked UV-C light path by other objects, the use of an active surface with long-lasting antimicrobial properties has been proposed as another appealing option for sterilization. One promising approach is the use of biomimetic Topographically Mediated Surfaces (TMSs) covered with densely packed nanopillars (needle-like structures). These TMSs are inspired by micro/nanotexture of naturally occurring

surfaces such as cicada wings and dragonfly wings, etc., which achieve a biocidal effect only with the surface structure possibly due to the destruction of the bacterial cells upon the mechanical interaction between the nanopillars and the bacterium exopolysaccharides (EPS) layer when movement on the surface occurs (Ivanova et al., 2012; Bandara et al., 2017; Cheng et al., 2019). In this project, by taking advantage of diamond's many material superiorities such as chemical inertness, hardness, corrosion resistance, and ability to deposit with countless morphologies, an attempt was made to develop a diamond-based antimicrobial surface as-deposited that does not require any pre-treatment or post-processing (Tang et al., 1995; Roy & Lee, 2007).

Our collaborators in the University of Louisville Speed School of Engineering have developed the Adaptive Robotic Nursing Assistant (ARNA) with a UV-C source to automate the disinfection process, as well as diamond nanospike (DNS) surfaces for the self-sterilization mechanism (Paxton et al., 2021). The objectives of the ARNA project are to 1) precisely define the UV dose and duration of radiation exposure required to inactivate human pathogens, including SARS-CoV-2, and 2) evaluate the feasibility of an automated disinfection process using the ARNA. The efficacy of UV-C against human pathogens was established using a handheld laboratory-grade UVC source (Spectroline™ ENF280C at 254 nm) with various test organisms such as *Escherichia coli* (*E. coli)* competent cells (Strain DH5 Alpha) and microorganisms collected from contaminated high-touch environmental surfaces on campus. For safety reasons, the use of Eilat virus (EILV) was proposed as a safe alternative model system in lieu of SARS-CoV-2 due to its structural similarity to SARS-CoV-2 and its narrow host range restricted to insects (Nasar et al., 2012). Like SARS-CoV-2, EILV is a small, spherical, enveloped virus with

a single-strand, positive-sense RNA genome, but, unlike SARS-CoV-2, is unable to infect and replicate in vertebrate cells, thus its use does not require a biosafety level 3 (BSL-3) facility (Nasar et al., 2012; Nasar et al., 2015). Here UV exposure with various doses, either by varying the distance of the source lamp from the target sample or by varying the duration of the exposure has been studied to determine the appropriate log reduction. Viral genome integrity inspection was conducted using quantitative real-time polymerase chain reaction (qRT-PCR) to determine the dose response. The objectives of the DNS surface project were to 1) accurately quantify bacterial growth on different surfaces to determine how they differ contingent on the structure and material of the surface and bacterial strain, and 2) image the morphology and behavior of bacteria following its adhesion to nanopillars through SEM to confirm the antimicrobial effect of the DNS surface. Experiments were conducted using *E. coli* competent cells (Strain DH5 Alpha), a gram-negative bacterium frequently used in previously reported work studying similar TMSs (Bandara et al., 2017; Cheng et al., 2019). Microbial growth was assessed by optical density measurement using a spectrophotometer.

Materials and Methods

UV-C Treatment

To examine the inactivation efficacy of UV-C on microorganisms, test organisms were exposed to UV radiation using a handheld laboratory-grade UVC source (Spectroline™ ENF280C at 254 nm) for varying amounts of time ranging from 1 to 3 min, from a one-inch distance.

UV-C Radiation on Bacteria Samples

NEB® 5-alpha Competent *E.coli* (DH5α) was inoculated in a liquid Lysogeny Broth (LB) medium at 37℃ for 24 hours under continuous shaking for sufficient growth. The *E.coli* culture was placed on a sterilized 2×2-inch stainless steel plate in 100 μL droplets and treated with UV-C for 90 seconds, from a one-inch distance. Samples were harvested off the plate with 1 mL of sterile liquid LB medium and transferred to test tubes. Dilutions of the harvested samples were made at 1:10 and 1:100 and spread onto solid LB-agar plates using an L-spreader. Plates were incubated at 37℃ for 24 hours to allow for bacterial growth and the resulting colonies after incubation were counted. Autoclaved deionized water and non-UV-treated bacteria samples were used for comparison.

Environmental Sampling and SARS-CoV-2 Detection

Sterile polyester swabs (cat no: 68310-282, CONSTIX®) were placed into 15 ml Falcon tubes filled with 1 ml viral transport medium (VTM) and stored at 4℃ until needed. Tubes were placed into a Styrofoam 15 ml tube holder and then into a styrofoam cooler that had dry ice. The Styrofoam cooler was sealed with tape and placed into a plastic storage bin for secure transport. For extra precaution, 70% ethanol was used during handling, transfer, and packing/unpacking samples. At the sample collection location (UofL Health Hospital), clinical samples were collected by swabbing the surfaces with swabs in the VTM. Unpacking and all sample manipulations were done in the BSL-2 laboratory. Viral RNA was extracted to quantify the genomic RNA levels by qRT-PCR as described below for potential SARS-CoV-2 detection.

Microorganisms were collected at various locations on campus before and after UV-C

treatment (e.g., elevator buttons, door handles of restrooms, and main building entrance) where large and frequent human traffic was observed, suggesting a high probability of contamination, by swabbing the surfaces with swabs moistened with deionized water placed in tubes. The tubes with samples were filled with 1 mL of sterile liquid LB medium and spread onto solid LB-agar plates using an L-spreader. The number of visible colonies was counted after 24 hours of incubation at 37℃.

Cell Line Maintenance and Experimental Infection with EILV

C7/10 cell line, an *A. albopictus* mosquito cell line, was propagated at 28℃ with 5% CO_2 in Dulbecco's minimal essential medium (DMEM) containing 10% (v/v) fetal bovine serum (FBS), 1 mM sodium pyruvate, 100 U/mL penicillin, 100 μg/mL streptomycin, and 1% (v/v) tryptose phosphate broth (TPB). The media was changed every 3-4 days by aspirating the media, washing the cells with 1X PBS, aspirating the PBS, and adding fresh culture media. Passaging cells was performed once every week to maintain a density of 2×10^4–5×10^4 cells/cm^2 (1,500,000–3,750,000 cells for a 75 cm^2 flask). EILV was amplified by infection of C7/10 cells and stored at -80°C. The C7/10 cells were grown to 80% confluence in a 75 cm^2 flask and subsequently infected with EILV at a multiplicity of infection (MOI) of ~0.1 PFU/cell.

RNA Extraction, Reverse Transcriptase (RT)-Dependent Conversion of RNA into cDNA, and qRT-PCR

Total RNA was extracted from 3 min UV-C irradiated and nonirradiated EILV using QIAamp Viral RNA Kits (cat no: 52906, QIAGEN) and RT^2 First Strand Kit (cat no: 330404, QIAGEN) was used for cDNA synthesis. qRT-PCR was subsequently carried

out in 20 µl reaction containing FastStart Universal SYBR Green Master (cat no: 4913850001, Milipore SIGMA), 20 µM each primer, nuclease-free water, CDC-2019-nCoV-Control-Plasmid, and EILV RT products for 3 reactions per sample. Oligonucleotides specific to control plasmid N gene and viral RNA-Polymerase gene were obtained using the information provided by the CDC (https://www.cdc.gov/coronavirus/2019-ncov/lab/rt-pcr-panel-primer-probes.html) and those specific to EILV N gene were designed using Primer3 (Rozen & Skaletsky, 2000, https://bioinfo.ut.ee/primer3-0.4.0/). Primer sequences are indicated in Table 5-1. The amplification system consisted of 10 min at 95°C, followed by 30 cycles of 15 sec at 95°C, 30 sec at 56°C, and 30 sec at 72°C. The product was held at 4°C at the end of the cycle. Relative quantification relies on the comparison between the expression of a target N gene in UV-treated EILV samples versus that in non-UV-treated EILV samples, relative to the expression of a reference gene (N in CDC-2019-nCoV-Control-Plasmid).

Table 5-1

List of primers used for qRT-PCR.

Primers	Sequence
2019-nCoV_N1-F	GAC CCC AAA ATC AGC GAA AT
2019-nCoV_N1-R	TCT GGT TAC TGC CAG TTG AAT CTG
2019-nCoV_N2-F	TTA CAA ACA TTG GCC GCA AA
2019-nCoV_N2-R	GCG CGA CAT TCC GAA GAA
2019-nCoV_N3-F	GGG AGC CTT GAA TAC ACC AAA A
2019-nCoV_N3-R	TGT AGC ACG ATT GCA GCA TTG
RNA-Polymerase-F	AGA TTT GGA CCT GCG AGC G

RNA-Polymerase-R	GAG CGG CTG TCT CCA CAA GT
Eilat Virus_N1-F	ACACTCATTCTACCGCCCAC
Eilat Virus_N1-R	GCTTCTTTGCCATCGCCATC
Eilat Virus_N2-F	CCTTCCCAACATTCACACTC
Eilat Virus_N2-R	CTATGTCTGTTTCCAGCACG

Spectrophotometry

NEB® 5-alpha Competent *E.coli* (DH5α) was inoculated in a liquid Lysogeny Broth (LB) medium at 37℃ overnight under continuous shaking for sufficient growth. 10 µL of *E.coli* culture was placed on each testing material including diamond nanospike surface and common commercially available surfaces (silicon, polycrystalline diamond, polyethylene plastic, and copper) and dried in a laminar flow hood for ~15 min. The materials were then incubated at 37℃ for 24 hours. After incubation, *E. coli* on the materials was harvested with 1 mL of pure sterile LB medium and loaded onto a Microplate, 96 well (Greiner Bio-One) optical density plate with a ten-fold dilution. The optical density (OD) of bacterial culture growth was measured using a spectrophotometer (SpectraMax® M2) set at 600-nm wavelength every 30 minutes for 14 hours with the software SoftMax Pro 7.0.

Scanning Electron Microscopy (SEM)

The *E.coli* culture was placed on silicon as a control and diamond nanospike surface, dried in a laminar flow hood for 24 hours, and then incubated at 37℃ for 24 hours. The *E. coli*-exposed samples were sputtered with gold and the morphology of interaction of *E. coli* with the surfaces was imaged using a scanning electron microscope (TESCAN

VEGA3 SBEASYPROBE and Nova NanoSEM 600 FEI) with an acceleration voltage of 15-20 kV.

Results and Discussion

Simulated Robotic UV-C irradiation causes a significant reduction in bacterial count on common surfaces

UV-C with a peak wavelength of 254 nm is known to be highly germicidal. The mechanism of action of UV-C on bacteria inactivation is based on the formation of dimers in RNA (uracil and cytosine) and DNA (thymine and cytosine) that inhibits transcription and replication, causing bacterial death (Cutler & Zimmerman, 2011). The efficacy of UV-C irradiation was first tested with DH5α *E. coli*. Bacterial suspensions were plated on a stainless-steel plate, one of the most widely used surface finishing types, and then exposed to UV-C irradiation for 90 sec, from a one-inch distance. The corresponding exposure dose was equivalent to 100 mJ/cm^2. The UV-treated bacterial suspensions were harvested with sterile LB, plated on a nutrient agar plate, and then incubated at 37℃ for 24 hours for observation and quantification of bacterial survival (Figure 5-1A). Surviving bacterial cells reproduced and formed a colony, which was then counted. The average bacterial colony forming units (CFU) was significantly reduced by 94.64% compared with non-treated bacterial culture ($n = 3$; $P < 0.0001$) (Figure 5-1B), confirming that a UV-C dose of 100 mJ/cm^2 at 254 nm is bactericidal. In addition, the experiment was conducted in the field (i.e., real-life) setting. Our target locations were Swain Student Activities Center and Shumaker Research Building at UofL, and target surfaces were frequently touched (i.e., potentially contaminated) surfaces (wood, metal,

glass, stainless steel, etc.) such as door, door handles, and elevator buttons, etc. Microorganisms were collected by surface swabbing and their growth before and after UV-C exposure was visually compared in the microbial growth media. Only flat surfaces have been tested for consistent and even delivery of UV dose. A UV-C dose of 100 mJ/cm^2 at 254 nm was also effective in killing random microorganisms regardless of the surface material as no growth was observed after UV-C exposure (Figure 5-2).

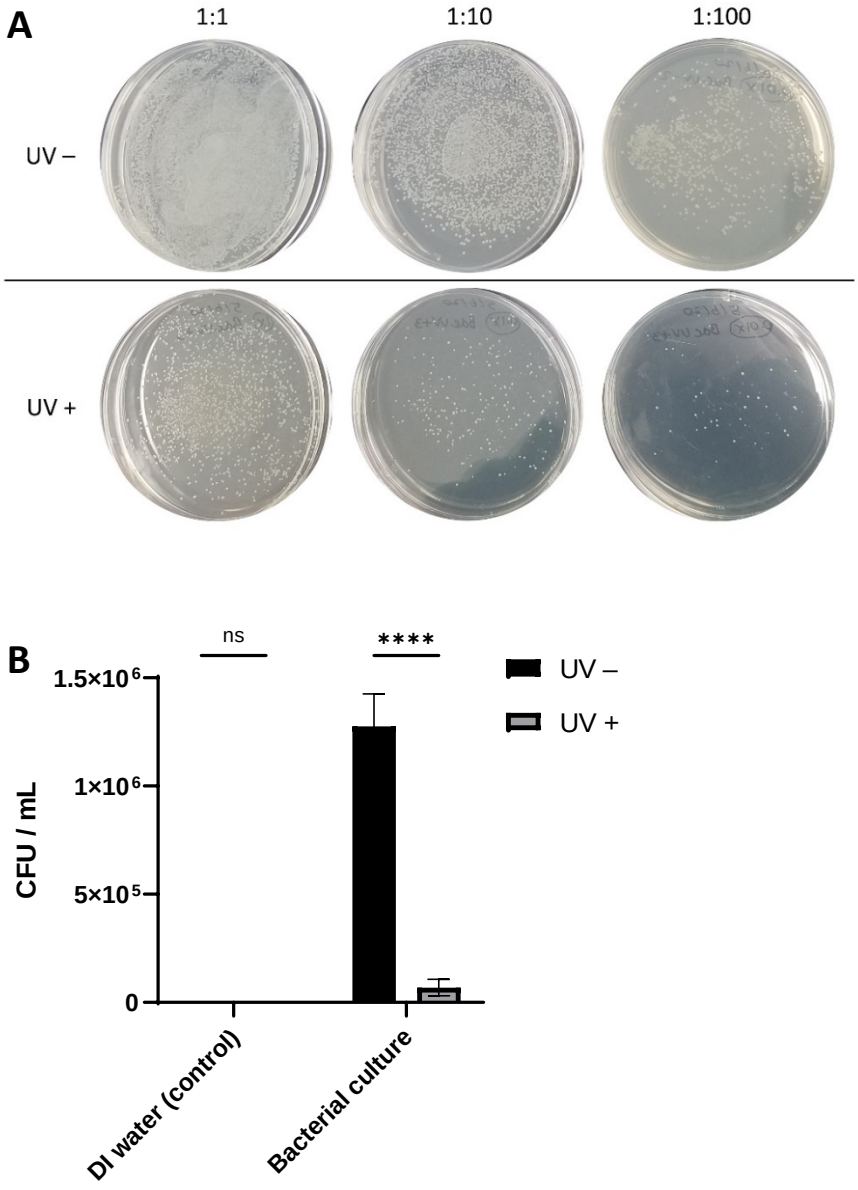

Figure 5-1: Colony forming units (CFU) analysis upon UV-C exposure.

(A) Representative images of bacterial growth with and without UV-C exposure. 1:1, 1:10, and 1:100 indicate the dilution factor. (B) Calculation of the number of surviving bacteria (CFU) per mL. Deionized (DI) water was used as a control (n = 3; DI water $P > 0.9999$, Bacterial culture $P < 0.0001$).

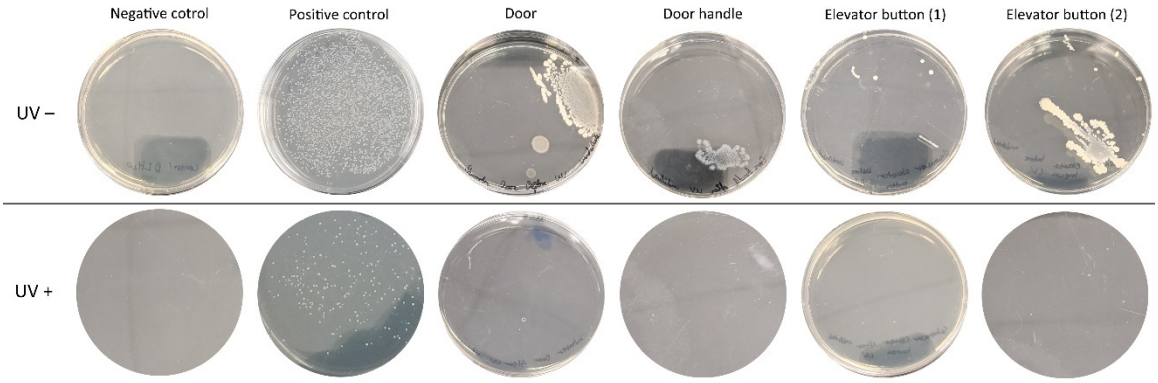

Figure 5-2: The growth of microorganisms collected from environmental surfaces upon UV-C exposure.

DI water and DH5α *E. coli* were used as negative and positive controls, respectively.

Simulated Robotic UV-C irradiation is highly effective in inactivating EILV

Since the COVID-19 pandemic that started in early 2020, global attention has focused on solving the problem of viral transmission, thus we examined whether disinfection using UV-C radiation is as effective in preventing viral transmission as inactivating bacteria. We focused on the inactivation of positive-sense single-stranded RNA (+ssRNA) viruses EILV, a safe alternative model system for SARS-CoV-2. qRT-PCR was used to identify EILV infectivity by detecting the target nucleocapsid protein

(N) gene, because the N gene of SARS-CoV-2 is a major positive component present in samples from positive patients and has been used as a target for the molecular diagnosis of COVID-19 (Klein et al., 2020).

The expression levels of a target N gene in UV-treated and un-treated EILV samples were compared by normalizing them to the expression level of a reference N gene of SARS-CoV-2 by running either UV-treated or un-treated EILV RT products and CDC-2019-nCoV-Control-Plasmid together with each of 2 sets of N primers (2019-nCoV_N1 and EILV_N). The average Ct values of the N gene in UV-treated EILV were 38.62, while those in un-treated EILV were 23.15, indicating that UV-treated EILV contains a relatively lower concentration of viral RNA compared to un-treated EILV (Figure 5-3A). UV-C treatment caused a significant reduction of fold change by 99.96%, representing a reduced expression level of the target N gene in EILV (n = 3; ****P < 0.0001) (Figure 5-3B).

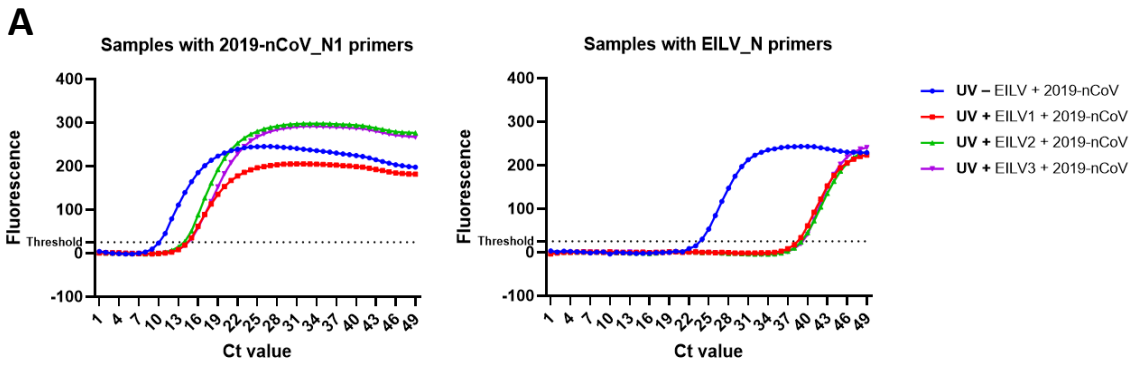

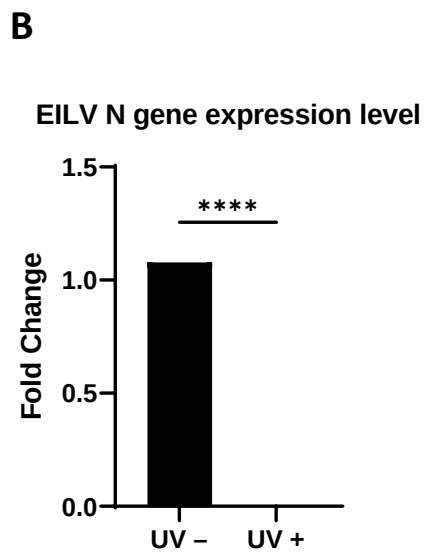

Figure 5-3: Quantification of virus inactivation upon UV-C exposure using qRT-PCR.

(A) Amplification curves of positive control (2019-nCoV) and three technical replicates of EILV with or without UV-C exposure. All values are the mean of each of the triplicates. (B) Average fold change (log2) expression of a target N gene in UV-treated EILV samples relative to expression of un-treated EILV samples, relative to expression of a reference N gene in 2019-nCoV ($n = 3$; $P < 0.0001$).

Conventional disinfection methods have the potential to inactivate SARS-CoV-2

Conventional disinfection methods include routine cleaning by spraying or physically wiping down with disinfectants containing soap, detergent, or bleach that have been proven to be effective against microorganisms. However, human errors such as missing spots and missed cleaning intervals can occur during hand disinfection procedures. To confirm that disinfection procedures at UofL Health (530 S Jackson St, Louisville, KY 40202) were conducted properly and to validate our technique, the SARS-

CoV-2 detection experiment was performed using clinical samples taken by swabbing the surfaces of the routinely cleaned rooms where patients who tested positive were admitted. While the positive control (CDC-2019-nCoV-Control-Plasmid) had a Ct value of 9.03 with 2019-nCoV_N1 primers and 8.9 with 2019-nCoV_N3 primers, all clinical samples had Ct values > 35 with either of two N primers, indicating a low viral load (Figure 5-4). Although Ct value is often used as a surrogate parameter for the amount of infectious particles in clinical specimens and hence infectivity, several studies state that there is no fixed Ct threshold for determining positivity, and, that Ct values should not be considered as reliable markers for viral infectivity (Walker et al., 2020; Platten et al., 2021).

However, it is undeniable that there is a strong relationship between the Ct values and the ability of the infectious virus to recover and the hazards of mortality (Singanayagam et al., 2020; Waudby-West et al., 2021). For example, only 8.2% (95% CI [Confidence Interval]: 2.8–18.4%) of the infectious virus with a Ct value > 35 was recovered from samples in the Public Health England (PHE) Schools study (Singanayagam et al., 2020), and lower initial Ct values (< 20) were associated with an increased risk of death compared to higher initial Ct values (> 30) (95% CI: 1.23–3.60%, P = 0.0069) (Waudby-West et al., 2021). Furthermore, studies analyzing the relationship between Ct values and viability of live SARS-CoV-2 viral culture reported no growth from specimens with a Ct value > 32 with the N gene target (Jefferson et al., 2020), thus we defined our clinical samples as a negative test result. Although more repeated experiments (replicates) are required due to the small sample size, these data demonstrate the potential effect of conventional disinfection methods on SARS-CoV-2 inactivation.

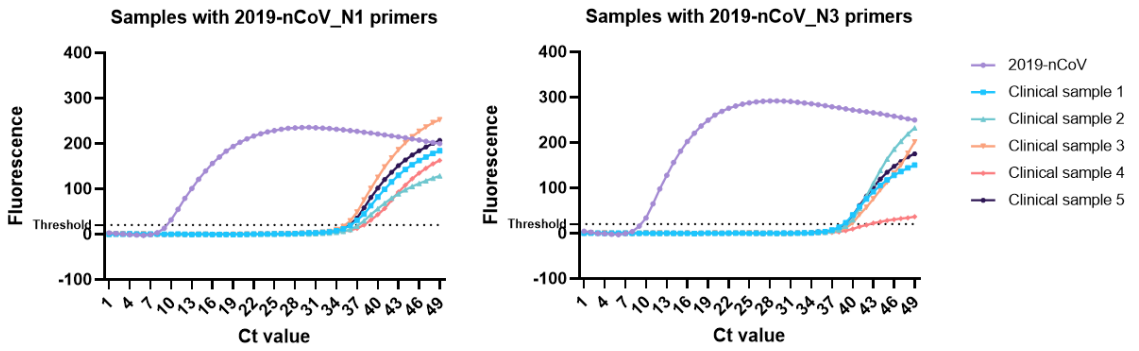

Figure 5-4: SARS-CoV-2 detection testing using clinical environmental surface samples.

Amplification curves of positive control (2019-nCoV) and five different clinical samples. All values are the mean of each of the triplicates.

Diamond nanospike (DNS) surfaces show highly effective biocidal properties against *E. coli* with the mechanism of nanopillar-mediated contact killing, inducing envelope deformation and eventually cell death

The limitation of conventional cleaning methods is that they are performed by a human operator. Many microbiological studies have shown that despite routine terminal disinfection, surfaces in hospital rooms vacated by patients remain contaminated with contagious pathogens, including vancomycin-resistant *Enterococci* (VRE), *Acinetobacter baumannii* complex (ABC), and methicillin-resistant *Staphylococcus aureus* (MRSA) (Byers et al., 1998; French et al., 2004; Manian et al., 2011; Otter et al., 2014). Since poorly disinfected surfaces can lead to the spreading of pathogens, “self-disinfecting” surfaces with coatings that retain antimicrobial activity for long periods of time have been suggested as the most effective solution (Humphreys, 2013; Weber & Rutala, 2013).

One novel strategy is to use biomimetic Topographically Mediated Surfaces (TMSs) covered with nano-sized pillars whose length scales are comparable to bacterial dimensions, enabling cell-surface interactions. The TMSs are inspired by the nanostructure of different unique surfaces found in nature, such as cicada wings (Figure 5-5) and dragonfly wings, etc. Such a structure helps them repel water and dirt with superhydrophobic properties, minimize the reflection of light to prevent detection by predators, and kill bacteria on contact solely through its physical structure by puncturing the bacterium exopolysaccharides (EPS) layer (Ivanova et al., 2012; Bandara et al., 2017; Cheng et al., 2019; Román-Kustas et al., 2020). The nanostructure covering cicada wings is known to be effective in killing Gram-negative cells (i.e., *Branhamella catarrhalis*, *Escherichia coli*, and *Pseudomonas fluorescens*) due to the envelope stretching to the point of physical rupture upon adherence, whereas Gram-positive cells (*Bacillus subtilis*, *Pseudococcus maritimus*, and *Staphylococcus aureus*) are less susceptible to nanopillar deformation and rupture due to the higher proportion of peptidoglycan present in the cell wall, making the cells more rigid and lowering maximum stretching capacity (Hasan et al., 2012; Pogodin et al., 2013).

However, the bactericidal efficiency could be enhanced by changing the tip sharpness and feature spacing (Kelleher et al., 2015; Xue et al., 2015). Xue et al. (2015) recommended that sharp nanostructures with large spacing were effective in increasing the killing efficiency, while Kelleher et al. (2015) proposed denser nanotexture packing. Diamond nanospike (DNS) surfaces, TMSs with diamond-based nanostructured coatings, developed by our collaborators in the University of Louisville Speed School of Engineering were tested for their antimicrobial properties against standard materials

including coppers known to be and silicon, and other diamond surfaces, including polycrystalline diamond without the nanostructuring (Paxton et al., 2021). In contrast to the cicada wing nanopillars arranged hexagonally and spaced around 170 nm from center to center, the DNS surface consists of the randomly oriented and densely packed sharp needle or spike-like structures with a high aspect ratio, taller (1 μm) in height and narrower (50 nm) in diameter compared to cicada wing nanopillars (200 nm in height, 100 nm at the base and 60 nm at the tip in diameter) (Ivanova et al., 2012; Paxton et al., 2021). The mechanical side of this project is described in detail in Paxton et al. (2021).

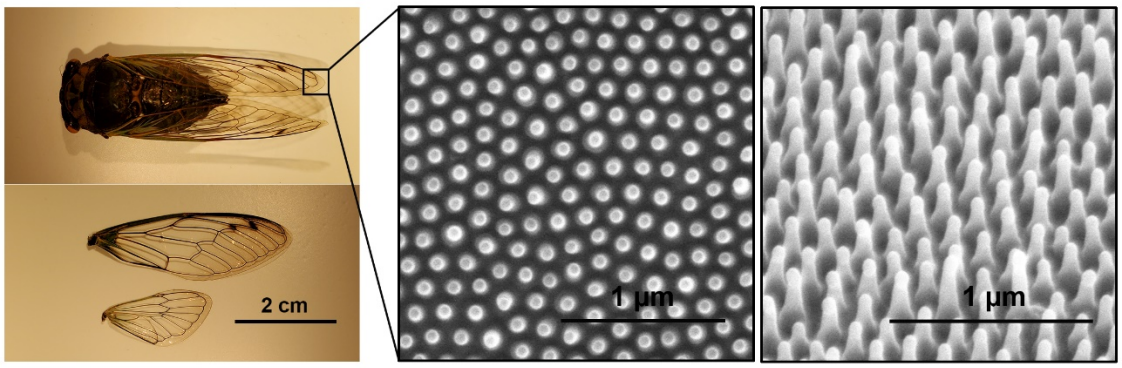

Figure 5-5: Cicada wing surface topography.

SEM microscopy images of nanopillar structures (top and side views) on cicada wing (kindly provided by Dr. Qu).

Unlike typical TMSs, which require extensive microfabrication, our samples are all in the as-deposited state, eliminating the need for specific pre-treatment or post-deposition fabrication methods, and are therefore very cost-effective. Since silicon was used as the substrate for the DNS surface, it was used as a contrasting control against the DNS surface, which was expected to have an antimicrobial effect, and was also used to

demonstrate that silicone does not contribute to its antimicrobial properties. The DH5α *E. coli* culture suspension was placed on the control silicon substrate, artificial DNS surface, and natural cicada wing surface, incubated at 37°C for 24 hours, and then SEM was performed to image the features of each surface and qualitatively analyze changes in bacterial morphology (Figure 5-6).

As shown in previous studies, *E. coli* cells on the cicada wing were observed to sink and spread between the nanopillars, reducing the viability of the adhered cells (Ivanova et al., 2012; Kelleher et al., 2015; Xue et al., 2015; Román-Kustas et al., 2020) (Figure 5-6 a). While the cells on the flat surface of the control silicon substrate were maintained in the healthy state (Figure 5-6 b), those on the DNS surfaces were destroyed in a manner similar to the cicada wing and remained in the damaged state, demonstrating their antibacterial properties (Figure 5-6 c).

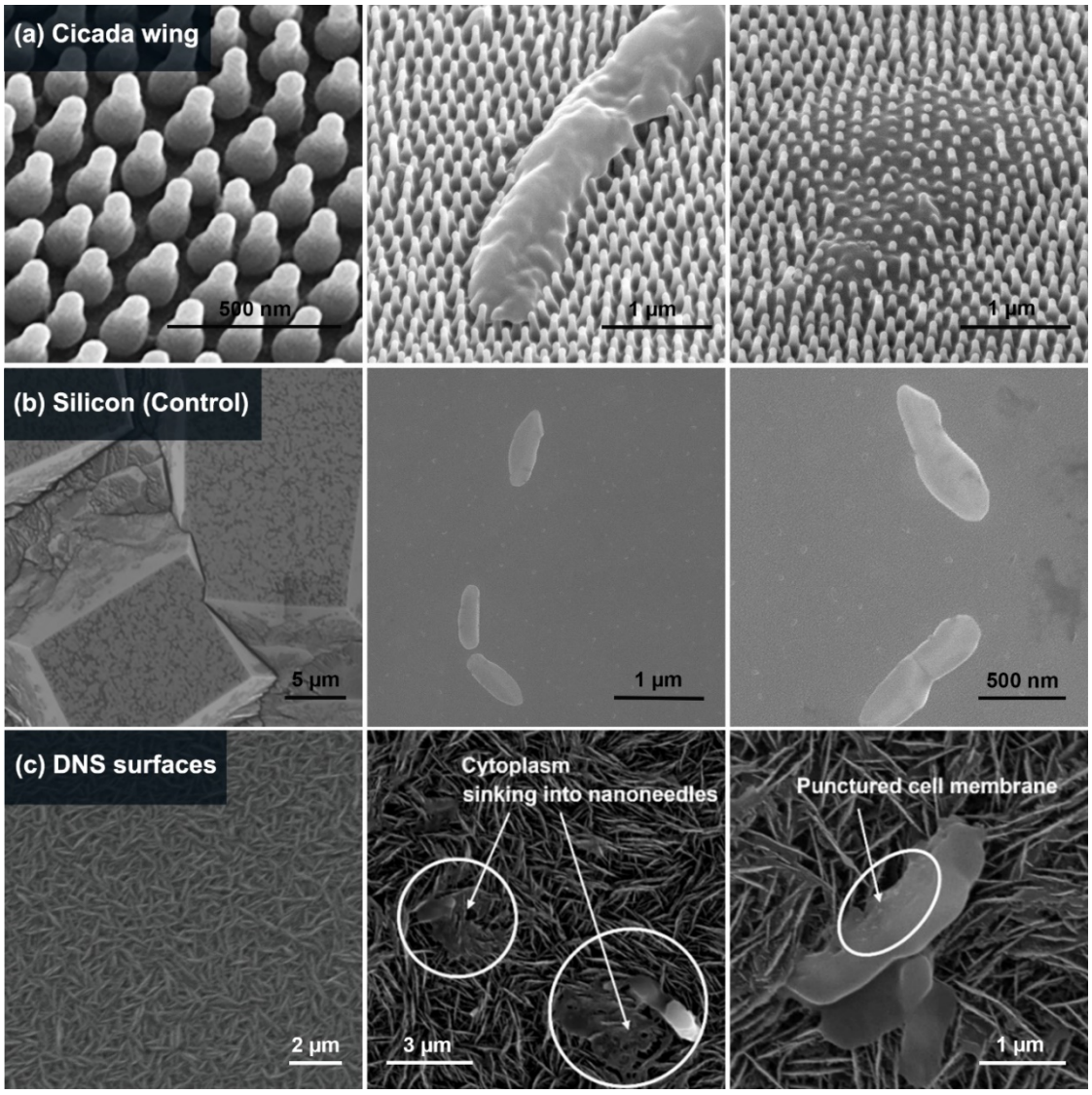

Figure 5-6: SEM analysis for observation of bacterial morphology on different surfaces.

SEM images of (a) cicada wing, (b) silicon and (c) DNS surfaces (kindly provided by Dr. Qu and Dr. Paxton, respectively).

The antibacterial properties of the DNS surfaces were validated by spectrophotometer analysis

Surface antibacterial properties were quantitatively investigated by assessing bacterial growth on the different surfaces over time using a spectrophotometer. In addition to the control silicon substrate, several other surfaces were tested, such as: polycrystalline diamond, in order not to exclude the effect of diamond, the same material used for making nanospikes, on the bactericidal properties; polypropylene plastic, a widely used material; and copper, a known natural antimicrobial material. Polycrystalline diamond is a deposited free-standing sample like the DNS surfaces, but differs significantly in morphology as it contains large grains >10 μm with a wide base, rounded top, and low aspect ratio (Paxton et al., 2021). Therefore, the probability of mechanical rupture of the cell by the structure itself was expected to be relatively low (less capacity to penetrate cells), allowing us to examine the effect of the diamond component itself. Copper has an intrinsic antimicrobial effect. Its capacity to release ions triggers oxidative stress through the production of reactive oxygen species (ROS), resulting in the loss of membrane integrity and eventually cell death by destroying all genetic material (Vincent et al., 2018; Salah et al., 2021). By including copper in the test surfaces, we investigated whether different contact-mediated killing mechanisms between the DNS surfaces and copper have any difference in the antibacterial activity efficiency. The DH5α *E. coli* culture suspension was placed on the different surfaces mentioned above, incubated at 37°C for 24 hours, and harvested off the surfaces. The optical density at 600 nm (OD600) of the harvested bacterial culture was measured every 30 minutes for 14 hours to monitor bacterial growth (Figure 5-7). The negative control, sterile bacteria growth medium, constantly showed no growth, ensuring that there were no external factors affecting the test results, such as cross-contamination and technical errors. The silicon and the

polycrystalline diamond did not exhibit antibacterial activity, displaying a consistent bacterial growth pattern over time, thus eliminating the possibility of the contribution of diamond and silicon components themselves to the antibacterial properties. While polypropylene plastic, the material we tested for its widespread use and popularity, showed the greatest bacterial growth, copper, not surprisingly, had the least bacterial growth of the four tested common materials. The results of the DNS surfaces were consistent with the SEM imaging results, as there was very little to no bacterial growth potentially due to physical disruption of the membrane upon bacterial attachment on the surface, consequently strongly supported the idea that it has antibacterial properties.

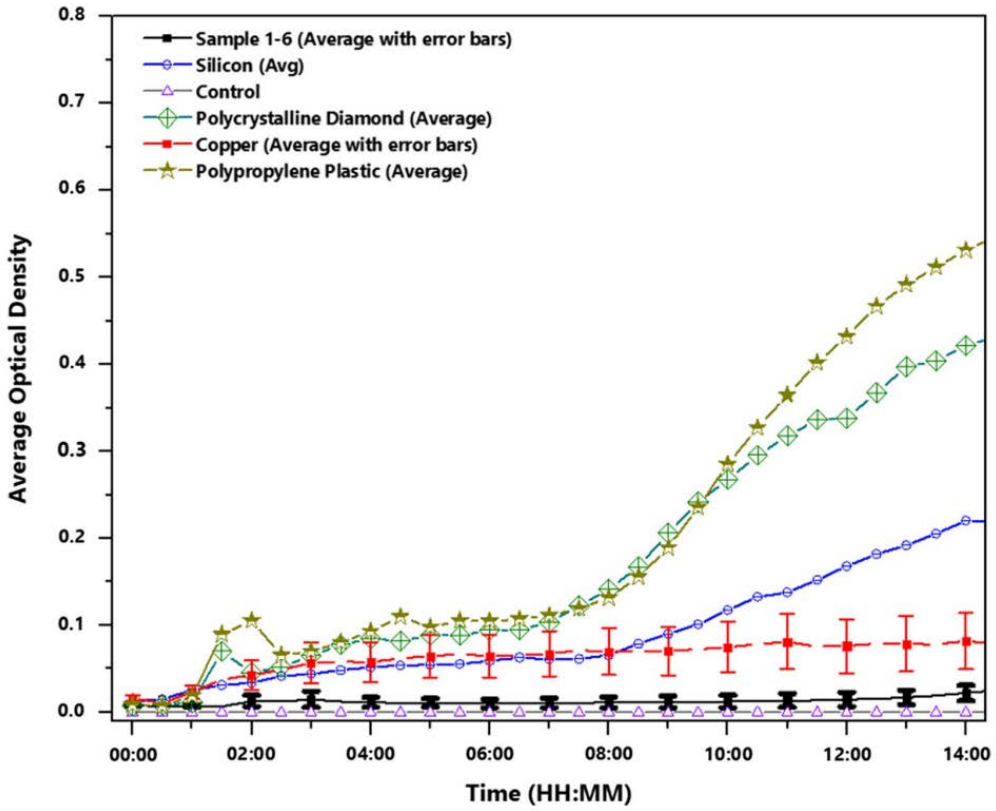

Figure 5-7: Spectrophotometer analysis.

Values are mean OD600 of DNS surfaces (6 samples, 11 trials), copper (5 trials), and silicon, polycrystalline diamond, polypropylene plastic, and a control (3 trials each). Sterile liquid LB medium was used as a negative control.

Conclusions and Future Directions

The rapid emergence of new or replacement strains of microorganisms (bacteria, fungi, and viruses) that have become resistant to antibiotics is occurring worldwide, increasing the risk of severe illness and even death (Prestinaci et al., 2015). In the face of this reality, there is an urgent need for action to avoid a developing global crisis, and surface disinfection has emerged as a crucial key to preventing environmental microorganisms' propagation (Querido et al., 2019; Ghedini et al., 2021). This project was additionally carried out in response to the global COVID-19 pandemic that occurred as the Rab-GGT project was taken place, as non-COVID-19 related projects were suspended, resulting in the lengthy interruption of the Rab-GGT project.

We focused on the development of innovative and effective disinfection approaches, such as the development of ARNA with the application of UV light and bio-mimicked self-cleaning surfaces with the application of superficial nanostructures. These approaches not only have excellent antimicrobial effects, but also minimize many of the issues that may arise during the process of application, implementation, and commercialization. Two major limitations of the application of UV light are that it poses a potential hazard to human health and only works in areas directly reached by the UV light (Trevisan et al., 2006; Zaffina et al., 2012). This could be addressed by an automated system with ARNA and by modifying the design of the UV source (e.g., using

multiple UV bulbs to generate UV irradiation from different angles) or by appropriately programming the robot to expose the curved or uneven areas that are out of the line of sight of a flat UV-C source. Furthermore, ARNA has many advantages such as labor cost-saving, free control of cleaning frequency, freely adjustable UV dose and exposure time, and being applicable to any place where a robot can access, including healthcare facilities. The issue with using previously developed self-disinfecting surfaces was the decreased efficacy of activity over time, the toxicity of the materials, and high cost of production and implementation in large areas (Vimbela et al., 2017; Querido et al., 2019; Ghedini et al., 2021). The DNS surfaces offer many advantages over no-touch strategies (e.g., UV light) or conventional disinfection techniques by enabling a constant process of activity with long-term stability and lowering toxicity. In addition, diamond-based nanostructured coatings are commercially attractive as they are synthesized in a single-step fabrication process, allowing a wide range of applications in both daily life and medical field.

In this study, the antimicrobial properties of UV light and DNS surfaces were demonstrated to be strongly effective in inactivating the ability of microorganisms to survive over surfaces and materials. Future studies will target a broad range of microorganisms, such as different bacterial or viral strains or fungal pathogens, including Gram-positive bacteria *Staphylococcus aureus,* non-enveloped virus Tobacco mosaic virus (TMV), which is environmentally more stable than enveloped viruses such as SARS-CoV-2, *Saccharomyces cerevisiae,* etc. With a variety of targets, the effectiveness of the disinfection process will be explored through the surface swabbing techniques that

have been proven effective for monitoring and assessing hygiene levels in this study using the actual ARNA robot.

Concluding, the ARNA with UV-C radiation and the DNS surfaces with self-sterilizing features are very powerful and promising approaches to mitigate the risk of infection resulting from the transmission of microorganisms through contaminated surfaces and show great potential for their extensive applications.

REFERENCES

Abràmoff, M. D., Magalhães, P. J., & Ram, S. J. (2004). Image processing with ImageJ. *Biophotonics International* 11: 36– 42.

Akhtar, S. S., Mekureyaw, M. F., Pandey, C., & Roitsch, T. (2020). Role of cytokinins for interactions of plants with microbial pathogens and pest insects. *Frontiers in Plant Science*, *10*.

Allen, G. J., Murata, Y., Chu, S. P., Nafisi, M., & Schroeder, J. I. (2002). Hypersensitivity of abscisic acid-induced cytosolic calcium increases in the Arabidopsis farnesyltransferase mutant era1-2. Plant Cell *14*, 1649-1662.

Anant, J. S., Desnoyers, L., Machius, M., Demeler, B., Hansen, J. C., Westover, K. D., Deisenhofer, J., & Seabra, M. C. (1998) Mechanism of Rab geranylgeranylation: formation of the catalytic ternary complex. Biochemistry 37:12559–12568.

Andrews, M., Huizinga, D. H., & Crowell, D. N. (2010). The CAAX specificities of Arabidopsis protein prenyltransferases explain ERA1 and GGB phenotypes. *BMC Plant Biology*, *10*(1).

Antimisiaris, M. F., & Running, M. P. (2014). Turning moss into algae: prenylation targets in Physcomitrella patens. *Plant Signal Behavior, 9*(7), 441-451.

Aoyama, T., Hiwatashi, Y., Shigyo, M., Kofuji, R., Kubo, M., Ito, M., & Hasebe, M. (2012). AP2-type transcription factors determine stem cell identity in the Moss Physcomitrella Patens. *Development, 139*(17), 3120–3129.

Arif, M. A., Hiss, M., Tomek, M., Busch, H., Meyberg, R., Tintelnot, S., Reski, R., Rensing, S. A., & Frank, W. (2019). ABA-induced vegetative diaspore formation in Physcomitrella patens. *Frontiers in Plant Science*, *10*.

Ashton, N. W., Grimsley, N. H., & Cove, D. J. (1979). Analysis of gametophytic development in the moss, Physcomitrella patens, using auxin and cytokinin resistant mutants. *Planta, 144*(5), 427–435.

Audagnotto, M., & Dal Peraro, M. (2017). Protein post-translational modifications: In silico prediction tools and molecular modeling. *Computational and Structural Biotechnology Journal*, *15*, 307–319.

Augustine, R. C., Pattavina, K. A., Tüzel, E., Vidali, L., & Bezanilla, M. (2011). Actin interacting Protein1 and actin depolymerizing factor drive rapid actin dynamics in*physcomitrella patens*. *The Plant Cell*, *23*(10), 3696–3710.

Bandara, C. D., Singh, S., Afara, I. O., Wolff, A., Tesfamichael, T., Ostrikov, K., & Oloyede, A. (2017). Bactericidal effects of natural nanotopography of dragonfly wing on escherichia coli. *ACS Applied Materials & Interfaces*, *9*(8), 6746–6760.

Banworth, M. J., & Li, G. (2017). Consequences of rab gtpase dysfunction in genetic or acquired human diseases. *Small GTPases*, *9*(1-2), 158–181.

Bao, L., Yamamoto, K. T., & Fujita, T. (2015). Phototropism in gametophytic shoots of the Moss*physcomitrella patens*. *Plant Signaling & Behavior*, *10*(3).

Bashline, L., Lei, L., Li, S., & Gu, Y. (2014). Cell wall, cytoskeleton, and cell expansion in higher plants. *Molecular Plant*, *7*(4), 586–600.

Batistič, O. (2012). Genomics and localization of the arabidopsis DHHC-cysteine-rich domain *s*-acyltransferase protein family. *Plant Physiology*, *160*(3), 1597–1612.

Byers, K. E., Durbin, L. J., Simonton, B. M., Anglim, A. M., Adal, K. A., & Farr, B. M. (1998). Disinfection of hospital rooms contaminated with vancomycin-resistant enterococcus faecium. *Infection Control and Hospital Epidemiology*, *19*(4), 261–264.

Bennett, T. A., Liu, M. M., Aoyama, T., Bierfreund, N. M., Braun, M., Coudert, Y., Dennis, R. J., O'Connor, D., Wang, X. Y., White, C. D., Decker, E. L., Reski, R., & Harrison, C. J. (2014). Plasma membrane-targeted pin proteins drive shoot development in a Moss. *Current Biology*, *24*(23), 2776–2785.

Bezanilla, M., Pan, A., & Quatrano, R. S. (2003). RNA interference in the moss Physcomitrella patens. *Plant Physiology*, *133*(2), 470-474.

Bezanilla, M., Perroud, P. F., Pan, A., Klueh, P., & Quatrano, R. S. (2005). An rnai system in *physcomitrella patens* with an internal marker for silencing allows for rapid identification of loss of function phenotypes. *Plant Biology*, *7*(3), 251–257.

Bhuin, T., & Roy, J. K. (2014). Rab proteins: The key regulators of intracellular vesicle transport. *Experimental Cell Research*, *328*(1), 1–19.

Bock, J. B., Matern, H. T., Peden, A. A. & Scheller, R. H. (2001). A genomic perspective on membrane compartment organization. Nature 409, 839-841.

Boisson, B., Giglione, C., & Meinnel, T. (2003). Unexpected protein families including cell defense components feature in the N-myristoylome of a higher eukaryote. *Journal of Biological Chemistry*, *278*(44), 43418–43429.

Bonetta, D., Bayliss, P., Sun, S., Sage, T., & McCourt, P. (2000). Farnesylation is involved in meristem organization in Arabidopsis. Planta *211*, 182-190.

Bowman, J. L., Floyd, S. K., & Sakakibara, K. (2007). Green genes—comparative genomics of the Green Branch of Life. *Cell*, *129*(2), 229–234.

Brady, S. M., Sarkar, S. F., Bonetta, D., & McCourt, P. (2003). The*abscisic acid insensitive 3*(*abi3*) gene is modulated by farnesylation and is involved in auxin signaling and lateral root development in*arabidopsis*. *The Plant Journal*, *34*(1), 67–75.

Bringmann, M., Li, E., Sampathkumar, A., Kocabek, T., Hauser, M.-T., & Persson, S. (2012). Pom-pom2/cellulose synthase INTERACTING1 is essential for the functional association of cellulose synthase and microtubules in *arabidopsis*. *The Plant Cell*, *24*(1), 163–177.

Brock, A. K., Willmann, R., Kolb, D., Grefen, L., Lajunen, H. M., Bethke, G., Lee, J., Nürnberger, T., & Gust, A. A. (2010). The Arabidopsis mitogen-activated protein kinase phosphatase PP2C5 affects seed germination, stomatal aperture, and abscisic acid-inducible gene expression. *Plant Physiology*, *153*(3), 1098–1111.

Campanoni, P., & Blatt, M. R. (2006). Membrane trafficking and polar growth in root hairs and pollen tubes. *Journal of Experimental Botany*, *58*(1), 65–74.

Casey, P. J. (1992). Biochemistry of protein prenylation. *J. Lipid Res.* 33, 1731-1740.

Chan, J. F.-W., Kok, K.-H., Zhu, Z., Chu, H., To, K. K.-W., Yuan, S., & Yuen, K.-Y. (2020). Genomic characterization of the 2019 NOVEL Human-pathogenic CORONAVIRUS isolated from a patient with atypical pneumonia after Visiting wuhan. *Emerging Microbes & Infections*, *9*(1), 221–236.

Chang, J. C., Ossoff, S. F., Lobe, D. C., Dorfman, M. H., Dumais, C. M., Qualls, R. G., & Johnson, J. D. (1985). UV inactivation of pathogenic and indicator microorganisms. *Applied and Environmental Microbiology*, *49*(6), 1361–1365.

Chater, C., Kamisugi, Y., Movahedi, M., Fleming, A., Cuming, A. C., Gray, J. E., & Beerling, D. J. (2011). Regulatory mechanism controlling stomatal behavior conserved across 400 million years of land plant evolution. *Current Biology*, *21*(12), 1025–1029.

Cheng, Y., Feng, G., & Moraru, C. I. (2019). Micro- and nanotopography sensitive bacterial attachment mechanisms: A Review. *Frontiers in Microbiology*, *10*.

Cheung, A. Y., & Wu, H.-M. (2008). Structural and signaling networks for the polar cell growth machinery in pollen tubes. *Annual Review of Plant Biology*, *59*(1), 547–572.

Coudert, Y., Palubicki, W., Ljung, K., Novak, O., Leyser, O., & Harrison, C. J. (2015). Author response: Three ancient hormonal cues co-ordinate shoot branching in a Moss. *eLife* 4: e06808.

Cove, D. J., Schild, A., Ashton, N. W., & Hartmann, E. (1978). Genetic and physiological studies of the effect of light on the development of the Moss, Physcomitrella Patens. *Photochemistry and Photobiology*, *27*(2), 249–254.

Cove, D. J., & Knight, C. D. (1993). The Moss PHYSCOMITRELLA patens, a model system with potential for the study of Plant Reproduction. *The Plant Cell*, 1483-1488.

Cove, D. (2005). The moss Physcomitrella patens. *Annu Rev Genet.*, *39*(39), 339-358.

Cove, D., Bezanilla, M., Harries, P., & Quatrano, R. (2006). Mosses as model systems for the study of metabolism and development. *Annual Review of Plant Biology*, *57*(1), 497–520.

Cove, D. J., Perroud, P., Charron, A. J., McDaniel, S. F., Khandelwal, A., & Quatrano, R. S. (2009). The Moss Physcomitrella PATENS: A novel model system for plant development and genomic studies. *Cold Spring Harbor Protocols, 2009*(2).

Cremers, F. P. M., Molloy, C. M., van de Pol, D. J. R., Hurk, J. A. J. M., Bach, I., Kessel, A. H. M. G., & Ropers, H.-H. (1992). An autosomal homologue of the choroideremia gene colocalizes with the Usher syndrome type II locus on the distal part of chromosome 1q. *Human Molecular Genetics*, *1*(2), 71–75.

Crowell, D. N., & Huizinga, D. H. (2009). Protein isoprenylation: The fat of the matter. *Trends in Plant Science*, *14*(3), 163–170.

Cutler, S., Ghassemian, M., Bonetta, D., Cooney, S., & McCourt, P. (1996). A protein farnesyl transferase involved in abscisic acid signal transduction in *arabidopsis*. *Science*, *273*(5279), 1239–1241.

Cutler, S. R., Rodriguez, P. L., Finkelstein, R. R., & Abrams, S. R. (2010). Abscisic acid: Emergence of a core signaling network. *Annual Review of Plant Biology*, *61*(1), 651–679.

Cutler, T. D., & Zimmerman, J. J. (2011). Ultraviolet irradiation and the mechanisms underlying its inactivation of infectious agents. *Animal Health Research Reviews*, *12*(1), 15–23.

Dai, T., Vrahas, M. S., Murray, C. K., & Hamblin, M. R. (2012). Ultraviolet C irradiation: An alternative antimicrobial approach to localized infections? *Expert Review of Anti-Infective Therapy*, *10*(2), 185–195.

Davies, P. J. (2010). The plant hormones: Their nature, occurrence, and functions. *Plant Hormones*, 1–15.

Decker, E. L., Frank, W., Sarnighausen, E., & Reski, R. (2006). Moss Systems Biology en route: Phytohormones in Physcomitrella Development. *Plant Biology*, *8*(3), 397–406.

Delwiche, C., & Cooper, E. (2015). The evolutionary origin of a Terrestrial Flora. *Current Biology*, *25*(19).

Deribe, Y. L., Pawson, T., Dikic, I. (2010) Post-translational modifications in signal integration. *Nat Struct Mol Biol*., 17, 666–72.

Díaz, M., Sanchez, Y., Bennett, T., Sun, C. R., Godoy, C., Tamanoi, F., Duran, A., & Perez, P. (1993). The schizosaccharomyces pombe CWG2+ gene codes for the beta subunit of a geranylgeranyltransferase type I required for beta-glucan synthesis. *The EMBO Journal*, *12*(13), 5245–5254.

Doonan, J. H., Cove, D. J., & Lloyd, C. W. (1988). Microtubules and microfilaments in tip growth: Evidence that microtubules impose polarity on protonemal growth in *physcomitrella patens*. *Journal of Cell Science*, *89*(4), 533–540.

Eklund, D. M., Thelander, M., Landberg, K., Ståldal, V., Nilsson, A., Johansson, M., Valsecchi, I., Pederson, E. R., Kowalczyk, M., Ljung, K., Ronne, H., & Sundberg, E. (2010). Homologues of the *arabidopsis thaliana shi/sty/lrp1* genes control auxin biosynthesis and affect growth and development in the Moss *physcomitrella patens*. *Development*, *137*(8), 1275–1284.

Farazi, T. A., Waksman, G., & Gordon, J. I. (2001). The biology and enzymology of proteinn-myristoylation. *Journal of Biological Chemistry*, *276*(43), 39501–39504.

Floyd, S. K., & Bowman, J. L. (2007). The ancestral developmental tool kit of Land Plants. *International Journal of Plant Sciences*, *168*(1), 1–35.

Fowler, J. E., & Quatrano, R. S. (1997). Plant cell morphogenesis: Plasma membrane interactions with the cytoskeleton and cell wall. *Annual Review of Cell and Developmental Biology*, *13*(1), 697–743.

Frank, W., Ratnadewi, D., & Reski, R. (2004). Physcomitrella patens is highly tolerant against drought, salt and osmotic stress. *Planta*, *220*(3), 384–394.

French, G. L., Otter, J. A., Shannon, K. P., Adams, N. M. T., Watling, D., & Parks, M. J. (2004). Tackling contamination of the hospital environment by Methicillin-resistant Staphylococcus aureus (MRSA): A comparison between conventional terminal cleaning and hydrogen peroxide vapour decontamination. *Journal of Hospital Infection*, *57*(1), 31–37.

Furt, F., Liu, Y.-C., Bibeau, J. P., Tüzel, E., & Vidali, L. (2012). Apical myosin XI anticipates F-actin during polarized growth of *physcomitrella patens*cells. *The Plant Journal*, *73*(3), 417–428.

Fujita, T., Sakaguchi, H., Hiwatashi, Y., Wagstaff, S. J., Ito, M., Deguchi, H., Sato, T., & Hasebe, M. (2008). Convergent evolution of shoots in land plants: Lack of auxin polar transport in Moss shoots. *Evolution & Development*, *10*(2), 176–186.

Galichet, A., & Gruissem, W. (2003). Protein farnesylation in plants–conserved mechanisms but different targets. *Current opinion in plant biology*, *6*(6), 530-535.

Gao, X., Nagawa, S., Wang, G., & Yang, Z. (2008). Cell polarity signaling: Focus on Polar Auxin Transport. *Molecular Plant*, *1*(6), 899–909.

Gelb, M. H. (1995). Chapter 14 Modification of Proteins by Prenyl Groups. *Cell Chemistry and Physiology: Part 1 Principles of Medical Biology*, 323–333.

Ghedini, E., Pizzolato, M., Longo, L., Menegazzo, F., Zanardo, D., & Signoretto, M. (2021). Which are the main surface disinfection approaches at the time of SARS-COV-2? *Frontiers in Chemical Engineering*, *2*.

Gomes, A. Q., Ali, B. R., Ramalho, J. S., Godfrey, R. F., Barral, D. C., Hume, A. N., & Seabra, M. C. (2003). Membrane Targeting of Rab GTPases Is Influenced by the Prenylation Motif. Molecular Biology of the Cell, 14(5), 1882–1899.

Goode, J. A., Stead, A. D., & Duckett, J. G. (1993). Redifferentiation of moss protonemata: An experimental and immunofluorescence study of brood cell formation. *Canadian Journal of Botany*, *71*(11), 1510-1519.

Goodstein, D., Shu, S., Howson, R., Neupane, R., Hayes, R., Fazo, J., Mitros, T., Dirks, W., Hellsten, U., Putnam, N., & Rokhsar, D. (2012). Phytozome: A comparative platform for green plant genomics. *Nucleic Acids Research*, *40*(D1), D1178–D1186.

Gorbalenya, A. E. *et al.* The species severe acute Respiratory syndrome-related coronavirus: Classifying 2019-ncov and naming It sars-cov-2. (2020). *Nature Microbiology*, *5*(4), 536–544.

Gordon, J. I., Duronio, R. J., Rudnick, D. A., Adams, S. P., & Gokel, G. W. (1991). Protein N-myristoylation. *Journal of Biological Chemistry*, *266*(14), 8647-8650.

Green, P. B. (1962). Mechanism for plant cellular morphogenesis. *Science*, *138*(3548), 1404–1405.

Grosshans, B. L., Ortiz, D., & Novick, P. (2006) Rabs and their effectors: achieving specificity in membrane traffic. *Proc. Natl. Acad. Sci. U.S.A.* 103, 11821–11827

Guo, Z., Wu, Y.-W., Das, D., Delon, C., Cramer, J., Yu, S., Thuns, S., Lupilova, N., Waldmann, H., Brunsveld, L., Goody, R. S., Alexandrov, K., & Blankenfeldt, W. (2008). Structures of rabggtase–substrate/product complexes provide insights into the evolution of protein prenylation. *The EMBO Journal*, *27*(18), 2444–2456.

Gutkowska, M., Wnuk, M., Nowakowska, J., Lichocka, M., Stronkowski, M. M., & Swiezewska, E. (2014). Rab geranylgeranyl transferase β subunit is essential for male fertility and tip growth in Arabidopsis. *Journal of Experimental Botany*, *66*(1), 213-224.

Gutkowska, M., & Swiezewska, E. (2012). Structure, regulation and cellular functions of Rab geranylgeranyl transferase and its cellular partner Rab Escort Protein. *Molecular Membrane Biology*, *29*(7), 243–256.

Hála, M., Eliáš, M., & Žárský, V. (2005). A specific feature of the Angiosperm Rab Escort Protein (Rep) and evolution of the REP/GDI superfamily. *Journal of Molecular Biology*, *348*(5), 1299–1313.

Hála, M., Soukupová, H., Synek, L., & Žárský, V. (2010). Arabidopsis rab geranylgeranyl transferase β-subunit mutant is constitutively photomorphogenic, and has shoot growth and gravitropic defects. *The Plant Journal*, *62*(4), 615–627.

Hallak, H., Muszbek, L., Laposata, M., Belmonte, E., Brass, L. F., & Manning, D. R. (1994). Covalent binding of arachidonate to G protein alpha subunits of human platelets. *Journal of Biological Chemistry*, *269*(7), 4713–4716.

Han, H., Adamowski, M., Qi, L., Alotaibi, S. S., & Friml, J. (2021). Pin-mediated polar auxin transport regulations in plant tropic responses. *New Phytologist*, *232*(2), 510–522.

Hasan, J., Webb, H. K., Truong, V. K., Pogodin, S., Baulin, V. A., Watson, G. S., Watson, J. A., Crawford, R. J., & Ivanova, E. P. (2012). Selective bactericidal activity of nanopatterned superhydrophobic cicada psaltoda claripennis wing surfaces. *Applied Microbiology and Biotechnology*, *97*(20), 9257–9262.

He, B., Chen, P., Chen, S. Y., Vancura, K. L., Michaelis, S., & Powers, S. (1991). Ram2, an essential gene of yeast, and RAM1 encode the two polypeptide components of the farnesyltransferase that prenylates A-factor and Ras proteins. *Proceedings of the National Academy of Sciences*, *88*(24), 11373–11377.

Heilingloh, C. S., Aufderhorst, U. W., Schipper, L., Dittmer, U., Witzke, O., Yang, D., Zheng, X., Sutter, K., Trilling, M., Alt, M., Steinmann, E., & Krawczyk, A. (2020). Susceptibility of sars-cov-2 to uv irradiation. *American Journal of Infection Control*, *48*(10), 1273–1275.

Hemsley, P. A. (2014). The importance of lipid modified proteins in plants. *New Phytologist*, *205*(2), 476–489.

Hemsley, P. A., Kemp, A. C., & Grierson, C. S. (2005) The TIPGROWTHDEFECTIVE1 S-acyl transferase regulates plant cell growth in *Arabidopsis. Plant Cell* 17: 2554–2563

Hemsley, P. A., Weimar, T., Lilley, K., Dupree, P., & Grierson, C. (2013). Palmitoylation in plants. *Plant Signaling & Behavior*, *8*(8).

Hemsley, P. A., Weimar, T., Lilley, K. S., Dupree, P., & Grierson, C. S. (2013). A proteomic approach identifies many novel palmitoylated proteins in Arabidopsis. *New Phytologist* 197: 805–814.

Hiwatashi, Y., Sato, Y., & Doonan, J. H. (2014). Kinesins have a dual function in organizing microtubules during both tip growth and cytokinesis in *physcomitrella patens*. *The Plant Cell*, *26*(3), 1256–1266.

Holzinger, A., & Karsten, U. (2013). Desiccation stress and tolerance in green algae: Consequences for ultrastructure, physiological and molecular mechanisms. *Frontiers in Plant Science*, *4*.

Hossain, A., Rahaman, M. S., Lee, D., Phung, T. K., Canlas, C. G., Simmons, B. A., Renneckar, S., Reynolds, W., George, A., Tulaphol, S., & Sathitsuksanoh, N. (2019). Enhanced Softwood Cellulose Accessibility by H3PO4 pretreatment: High sugar yield without compromising lignin integrity. *Industrial & Engineering Chemistry Research*, *59*(2), 1010–1024.

Huang, Y., Yang, C., Xu, X.-feng, Xu, W., & Liu, S.-wen. (2020). Structural and functional properties of SARS-COV-2 spike protein: Potential antivirus drug development for covid-19. *Acta Pharmacologica Sinica*, *41*(9), 1141–1149.

Humphreys, H. (2013). Self-disinfecting and microbiocide-impregnated surfaces and fabrics: What potential in interrupting the spread of healthcare-associated infection? *Clinical Infectious Diseases*, *58*(6), 848–853.

Hutagalung, A. H., & Novick, P. J. (2011). Role of Rab GTPases in membrane traffic and Cell Physiology. *Physiological Reviews*, *91*(1), 119–149.

Inoue, T., Higuchi, M., Hashimoto, Y., Seki, M., Kobayashi, M., Kato, T., Tabata, S., Shinozaki, K., & Kakimoto, T. (2001). Identification of CRE1 as a cytokinin receptor from Arabidopsis. *Nature*, *409*(6823), 1060–1063.

Ivanova, E. P., Hasan, J., Webb, H. K., Truong, V. K., Watson, G. S., Watson, J. A., Baulin, V. A., Pogodin, S., Wang, J. Y., Tobin, M. J., Löbbe, C., & Crawford, R. J. (2012). Natural bactericidal surfaces: Mechanical rupture of pseudomonas aeruginosa cells by cicada wings. *Small*, *8*(16), 2489–2494.

Jang, G., & Dolan, L. (2011). Auxin promotes the transition from Chloronema to Caulonema in Moss Protonema by positively regulating PpRSL1and PPRSL2 in Physcomitrella patens. *New Phytologist*, *192*(2), 319–327.

Jawaid, M. Z., Sinclair, R., Cox, D., & Drakakaki, G. (2020). A biophysical model for Plant Cell Plate Development.

Jefferson, T., Spencer, E. A., Brassey, J., & Heneghan, C. (2020). Viral cultures for coronavirus disease 2019 infectivity assessment: A systematic review. *Clinical Infectious Diseases*, *73*(11).

Jenkins, G. I., & Cove, D. J. (1983). Phototropism and polarotropism of primary chloronemata of the Moss Physcomitrella patens: Responses of mutant strains. *Planta*, *159*(5), 432–438.

Jenkins, G. I., Courtice, G. R., & Cove, D. J. (1986). Gravitropic responses of wild-type and mutant strains of the Moss Physcomitrella patens. *Plant, Cell and Environment*, *9*(8), 637–644.

Johnson, C. D., Chary, S. N., Chernoff, E. A., Zeng, Q., Running, M. P., & Crowell, D. N. (2005). Protein geranylgeranyltransferase I is involved in specific aspects of abscisic acid and auxin signaling in Arabidopsis. *Plant Physiology*, *139*(2), 722–733.

Johnson, D Russell, Bhatnagar, Rajiv S, Knoll, Laura J, & Gordon, Jeffrey I. (1994). Genetic and biochemical studies of protein N-myristoylation. *Annual review of biochemistry*, *63*(1), 869-914.

Kamisugi, Y. (2005). Parameters determining the efficiency of gene targeting in the moss Physcomitrella patens. *Nucleic Acids Research*, *33*(19).

Kamisugi, Y., von Stackelberg, M., Lang, D., Care, M., Reski, R., Rensing, S. A., & Cuming, A. C. (2008). A SEQUENCE-ANCHORED genetic linkage map for THE Moss, physcomitrella patens. *The Plant Journal*, *56*(5), 855–866.

Kampf, G (2018). Efficacy of ethanol against viruses in hand disinfection. J Hosp Infect, 98, pp. 331-338.

Kelleher, S. M., Habimana, O., Lawler, J., O' Reilly, B., Daniels, S., Casey, E., & Cowley, A. (2015). Cicada wing surface topography: An investigation into the bactericidal properties of Nanostructural features. *ACS Applied Materials & Interfaces*, *8*(24), 14966–14974.

Khraiwesh, B., Qudeimat, E., Thimma, M., Chaiboonchoe, A., Jijakli, K., Alzahmi, A., Arnoux, M., & Salehi-Ashtiani, K. (2015). Genome-wide expression analysis offers new insights into the origin and evolution of Physcomitrella Patens Stress response. *Scientific Reports*, *5*(1).

Khraiwesh, B., Ossowski, S., Weigel, D., Reski, R., & Frank, W. (2008). Specific gene silencing by artificial micrornas in *physcomitrella patens*: An alternative to targeted Gene Knockouts. *Plant Physiology*, *148*(2), 684–693.

Kim, S.-J., & Brandizzi, F. (2014). The plant secretory pathway: An essential factory for building the Plant Cell Wall. *Plant and Cell Physiology*, *55*(4), 687–693.

Klein, R. C., Klein, M. H., Barbosa, L. G., Knnup, L. V., Venâncio, L. P., Lima, J. B., & Araújo-Santos, T. (2020). Optimizing SARS-COV-2 molecular diagnostic using N gene target: Insights about reinfection.

Komatsu, K., Suzuki, N., Kuwamura, M., Nishikawa, Y., Nakatani, M., Ohtawa, H., Takezawa, D., Seki, M., Tanaka, M., Taji, T., Hayashi, T., & Sakata, Y. (2013). Group A PP2Cs evolved in land plants as key regulators of intrinsic desiccation tolerance. *Nature Communications*, *4*(1).

Kou, X., Zhao, X., Wu, B., Wang, C., Wu, C., Yang, S., Zhou, J., & Xue, Z. (2022). Auxin response factors are ubiquitous in plant growth and development, and involved in crosstalk between Plant Hormones: A Review. *Applied Sciences*, *12*(3), 1360.

Kramer, E. M. (2009). Chapter 4 new model systems for the study of Developmental Evolution in plants. *Current Topics in Developmental Biology*, 67–105.

Kubo, M., Imai, A., Nishiyama, T., Ishikawa, M., Sato, Y., Kurata, T., Hiwatashi, Y., Reski, R., & Hasebe, M. (2013). System for stable β-estradiol-inducible gene expression in the Moss Physcomitrella patens. *PLoS ONE*, *8*(9).

Lai, C.-C., Shih, T.-P., Ko, W.-C., Tang, H.-J., & Hsueh, P.-R. (2020). Severe acute respiratory syndrome CORONAVIRUS 2 (SARS-CoV-2) and CORONAVIRUS disease-2019 (COVID-19): The epidemic and the challenges. *International Journal of Antimicrobial Agents*, *55*(3), 105924.

Landberg, K., Šimura, J., Ljung, K., Sundberg, E., & Thelander, M. (2020). Studies of moss reproductive development indicate that auxin biosynthesis in apical stem cells

may constitute an ancestral function for focal growth control. *New Phytologist*, *229*(2), 845-860.

Lavy, M., Prigge, M., Tao, S., Shain, S., Kuo, A., Kirchsteiger, K., & Estelle, M. (2016). Author response: Constitutive Auxin response in Physcomitrella reveals complex interactions between aux/IAA and Arf Proteins. *ELife*, 5: e13325.

Lazar, T., Götte, M., & Gallwitz, D. (1997). Vesicular transport: How many YPT/Rab-GTPases make a eukaryotic cell? *Trends in Biochemical Sciences*, *22*(12), 468–472.

Le Bail, A., Scholz, S., & Kost, B. (2013). Evaluation of reference genes for RT qPCR analyses of structure-specific and hormone regulated gene expression in physcomitrella patens gametophytes. *PLoS ONE*, *8*(8).

Lee, K. J. D., Sakata, Y., Mau, S.-L., Pettolino, F., Bacic, A., Quatrano, R. S., Knight, C. D., & Knox, J. P. (2005). Arabinogalactan proteins are required for apical cell extension in the moss *physcomitrella patens*. *The Plant Cell*, *17*(11), 3051–3065.

Leung, K. F., Baron, R., & Seabra, M. C. (2006). Thematic Review series: Lipid Posttranslational Modifications. geranylgeranylation of rab gtpases. *Journal of Lipid Research*, *47*(3), 467–475.

Li, S., Lei, L., Somerville, C. R., & Gu, Y. (2011). Cellulose synthase interactive protein 1 (CSI1) links microtubules and cellulose synthase complexes. *Proceedings of the National Academy of Sciences*, *109*(1), 185–190.

Lo, C.-W., Matsuura, R., Iimura, K., Wada, S., Shinjo, A., Benno, Y., Nakagawa, M., Takei, M., & Aida, Y. (2021). UVC disinfects SARS-COV-2 by induction of viral Genome damage without apparent effects on VIRAL morphology and proteins. *Scientific Reports*, *11*(1).

Lohani, N., Singh, M. B., & Bhalla, P. L. (2022). Biological parts for engineering abiotic stress tolerance in plants. *BioDesign Research*, *2022*, 1–41.

Loraine, A. E., Yalovsky, S., Fabry, S., & Gruissem, W. (1996) Tomato Rab1A homologs as molecular tools for studying Rab geranylgeranyltransferase in plant cells. *Plant Physiol*. 110, 1337–1347.

Maciel da Silva, A. S., Simabukuro, E. A., & Pôrto, K. C. (2009). Effect of water availability on spore germination of the Moss*octoblepharum albidum*from Brazilian Atlantic Forest. *Journal of Bryology*, *31*(3), 169–173.

Maltese, W. A. (1990). Posttranslational modification of proteins by isoprenoids in mammalian cells. *The FASEB Journal*, *4*(15), 3319–3328.

Manian, F. A., Griesenauer, S., Senkel, D., Setzer, J. M., Doll, S. A., Perry, A. M., & Wiechens, M. (2011). Isolation of*acinetobacter baumannii*complex and methicillin-resistant*staphylococcus aureus*from hospital rooms following terminal cleaning and disinfection: Can we do better? *Infection Control & Hospital Epidemiology*, *32*(7), 667–672.

Mashiguchi, K., Tanaka, K., Sakai, T., Sugawara, S., Kawaide, H., Natsume, M., Hanada, A., Yaeno, T., Shirasu, K., Yao, H., McSteen, P., Zhao, Y., Hayashi, K.-ichiro, Kamiya, Y., & Kasahara, H. (2011). The main auxin biosynthesis pathway in *arabidopsis. Proceedings of the National Academy of Sciences*, *108*(45), 18512–18517.

Matsuura, R., Lo, C.-W., Wada, S., Somei, J., Ochiai, H., Murakami, T., Saito, N., Ogawa, T., Shinjo, A., Benno, Y., Nakagawa, M., Takei, M., & Aida, Y. (2021). SARS-COV-2 disinfection of air and surface contamination by TIO2 photocatalyst-mediated damage to viral morphology, RNA, and protein. *Viruses*, *13*(5), 942.

Maurer-Stroh, S., Washietl, S., and Eisenhaber, F. (2003). Protein prenyltransferases. *Genome Biology*, *4*(4), 212.

Maurer-Stroh, S., & Eisenhaber, F. (2005). Refinement and prediction of protein prenylation motifs. . *Genome Biology*, *6*(6), 1–15.

Maurer-Stroh, S., Koranda, M., Benetka, W., Schneider, G., Sirota, F. L., & Eisenhaber, F. (2007). Towards complete sets of farnesylated and geranylgeranylated proteins. *PLoS Computational Biology*, *3*(4).

McBride, R., van Zyl, M., & Fielding, B. (2014). The coronavirus nucleocapsid is a multifunctional protein. *Viruses*, *6*(8), 2991–3018.

McTaggart, S. J. (2006). Isoprenylated proteins. *Cellular and Molecular Life Sciences*, *63*(3), 255–267.

Menand, B., Calder, G., & Dolan, L. (2007). Both chloronemal and caulonemal cells expand by tip growth in the moss Physcomitrella patens. *Journal of Experimental Botany*, *58*(7), 1843-1849.

Merry, D. E., Jänne, P. A., Landers, J. E., Lewis, R. A., & Nussbaum, R. L. (1992). Isolation of a candidate gene for choroideremia. *Proceedings of the National Academy of Sciences*, *89*(6), 2135–2139.

Mishler, B. D., & Oliver, M. J. (2018). Putting *physcomitrella patens* on the Tree of Life: The Evolution and ecology of Mosses. *Annual Plant Reviews Online*, 1–15.

Nasar, F., Palacios, G., Gorchakov, R. V., Guzman, H., Da Rosa, A. P., Savji, N., Popov, V. L., Sherman, M. B., Lipkin, W. I., Tesh, R. B., & Weaver, S. C. (2012). Eilat

virus, a unique alphavirus with host range restricted to insects by RNA replication. *Proceedings of the National Academy of Sciences*, *109*(36), 14622–14627.

Nasar, F., Gorchakov, R. V., Tesh, R. B., & Weaver, S. C. (2015). Eilat virus host range restriction is present at multiple levels of the virus life cycle. *Journal of Virology*, *89*(2), 1404–1418.

Naqvi, A. A., Fatima, K., Mohammad, T., Fatima, U., Singh, I. K., Singh, A., Atif, S. M., Hariprasad, G., Hasan, G. M., & Hassan, M. I. (2020). Insights into sars-cov-2 genome, structure, evolution, pathogenesis and therapies: Structural genomics approach. *Biochimica Et Biophysica Acta (BBA) - Molecular Basis of Disease*, *1866*(10), 165878.

Nguyen, U. T., Goody, R. S., & Alexandrov, K. (2010). Understanding and exploiting protein prenyltransferases. *ChemBioChem*, *11*(9), 1194–1201.

Oliver, M. J. (2005). Desiccation tolerance in bryophytes: A reflection of the primitive strategy for plant survival in dehydrating habitats? *Integrative and Comparative Biology*, *45*(5), 788–799.

Otter, J. A., Yezli, S., Perl, T. M., Barbut, F., & French, G. L. (2014). A guide to no-touch automated room disinfection (NTD) systems. *Decontamination in Hospitals and Healthcare*, 413–460.

Paredez, A. R., Somerville, C. R., & Ehrhardt, D. W. (2006). Visualization of cellulose synthase demonstrates functional association with microtubules. *Science*, *312*(5779), 1491–1495.

Paxton, W. F., Rozsa, J. L., Brooks, M. M., Running, M. P., Schultz, D. J., Jasinski, J. B., Jung, H. J., & Akram, M. Z. (2021). A scalable approach to topographically mediated antimicrobial surfaces based on Diamond. *Journal of Nanobiotechnology*, *19*(1).

Pei, Z. M., Ghassemian, M., Kwak, C. M., McCourt, P., & Schroeder, J. I. (1998). Role of farnesyltransferase in ABA regulation of guard cell anion channels and plant water loss. Science *282*, 287-290.

Pereira-Leal, J. B., Hume, A. N., & Seabra, M. C. (2001) Prenylation of Rab GTPases: molecular mechanisms and involvement in genetic disease. *FEBS Lett.* 498, 197–200.

Pereira-Leal, J. B., & Seabra, M. C. (2001). Evolution of the Rab family of small GTP-binding proteins. *Journal of Molecular Biology*, *313*(4), 889–901.

Pfeffer, S., & Aivazian, D. (2004). Targeting rab GTPases to distinct membrane compartments. *Nature Reviews Molecular Cell Biology*, *5*(11), 886–896.

Pfeifer, G. P., You, Y.-H., & Besaratinia, A. (2005). Mutations induced by ultraviolet light. *Mutation Research/Fundamental and Molecular Mechanisms of Mutagenesis*, *571*(1-2), 19–31.

PHYSCObase. http://moss.nibb.ac.jp/

Pinheiro, H., Samalova, M., Geldner, N., Chory, J., Martinez, A., & Moore, I. (2009). Genetic evidence that the higher plant Rab-D1 and Rab-D2 GTPases exhibit distinct but overlapping interactions in the early secretory pathway. *Journal of Cell Science*, *122*(20), 3749–3758.

Platten, M., Hoffmann, D., Grosser, R., Wisplinghoff, F., Wisplinghoff, H., Wiesmüller, G., Schildgen, O., & Schildgen, V. (2021). SARS-COV-2, CT-values, and infectivity—conclusions to be drawn from Side Observations. *Viruses*, *13*(8), 1459.

Pogodin, S., Hasan, J., Baulin, V. A., Webb, H. K., Truong, V. K., Phong Nguyen, T. H., Boshkovikj, V., Fluke, C. J., Watson, G. S., Watson, J. A., Crawford, R. J., & Ivanova, E. P. (2013). Biophysical model of bacterial cell interactions with nanopatterned cicada wing surfaces. *Biophysical Journal*, *104*(4), 835–840.

Prestinaci, F., Pezzotti, P., & Pantosti, A. (2015). Antimicrobial resistance: A global multifaceted phenomenon. *Pathogens and Global Health*, *109*(7), 309–318.

Prigge, M. J., Lavy, M., Ashton, N. W., & Estelle, M. (2010). Physcomitrella patens auxin-resistant mutants affect conserved elements of an auxin-signaling pathway. *Current Biology*, *20*(21), 1907–1912.

Prigge, M. J., & Bezanilla, M. (2010). Evolutionary crossroads in developmental biology: Physcomitrella patens. *Development*, *137*(21), 3535-3543.

Proctor, M. C., & Tuba, Z. (2002). Poikilohydry and homoihydry: Antithesis or spectrum of possibilities? *New Phytologist*, *156*(3), 327–349.

Pylypenko, O., Hammich, H., Yu, I.-M., & Houdusse, A. (2017). Rab GTPases and their interacting protein partners: Structural insights into RAB functional diversity. *Small GTPases*, *9*(1-2), 22–48.

Querido, M. M., Aguiar, L., Neves, P., Pereira, C. C., & Teixeira, J. P. (2019). Self-disinfecting surfaces and Infection Control. *Colloids and Surfaces B: Biointerfaces*, *178*, 8–21.

Rensing, S. A., Lang, D., Zimmer, A. D., Terry, A., Salamov, A., Shapiro, H., Nishiyama, T., Perroud Pierre-François, Lindquist, E. A., Kamisugi, Y., Tanahashi, T., Sakakibara, K., Fujita, T., Oishi, K., Shin-I, T., Kuroki, Y., Toyoda, A., Suzuki, Y., Hashimoto, S.-ichi, … Boore, J. L. (2008). The *physcomitrella* genome reveals

evolutionary insights into the conquest of land by plants. *Science*, *319*(5859), 64–69.

Rensing, S. A., Goffinet, B., Meyberg, R., Wu, S.-Z., & Bezanilla, M. (2020). The moss *physcomitrium* (*physcomitrella*) *patens*: A model organism for Non-Seed plants. *The Plant Cell*, *32*(5), 1361–1376.

Resh, M. D. (2006). Trafficking and signaling by fatty-acylated and prenylated proteins. *Nature Chemical Biology*. *2*(11), 584–90.

Resh, M. D. (2006). Palmitoylation of ligands, receptors, and intracellular signaling molecules. *Science's STKE*, *2006*(359).

Reski, R., & Abel, W. O. (1985). Induction of budding on chloronemata and Caulonemata of the moss, Physcomitrella patens, using isopentenyladenine. *Planta*, *165*(3), 354–358.

Reski, R., Bae, H., & Simonsen, H. T. (2018). Physcomitrella patens, a versatile synthetic biology chassis. *Plant Cell Reports*, *37*(10), 1409–1417.

Rojek, J., Tucker, M. R., Pinto, S. C., Rychłowski, M., Lichocka, M., Soukupova, H., Nowakowska, J., Bohdanowicz, J., Surmacz, G., & Gutkowska, M. (2021). Rab-dependent vesicular traffic affects female gametophyte development in Arabidopsis. *Journal of Experimental Botany*, *72*(2), 320–340.

Pereira-Leal, J. B., & Seabra, M. C. (2001). Evolution of the Rab family of small GTP-binding proteins. *Journal of Molecular Biology*, *313*(4), 889–901.

Perroud, P.-F., & Quatrano, R. S. (2006). The role of ARPC4 in tip growth and alignment of the polar axis in filaments of *physcomitrella patens*. *Cell Motility and the Cytoskeleton*, *63*(3), 162–171.

Perroud, P.-F., & Quatrano, R. S. (2008). BRICK1 is required for apical cell growth in filaments of the Moss *physcomitrella patens* but not for gametophore morphology. *The Plant Cell*, *20*(2), 411–422.

Pierre, M., Traverso, J. A., Boisson, B., Domenichini, S., Bouchez, D., Giglione, C., & Meinnel, T. (2007). N-myristoylation regulates the SnRK1 pathway in Arabidopsis. *Plant Cell* 19: 2804–2821.

Prigge, M. J., Lavy, M., Ashton, N. W., & Estelle, M. (2010). Physcomitrella patens auxin-resistant mutants affect conserved elements of an auxin-signaling pathway. *Current Biology*, *20*(21), 1907–1912.

Román-Kustas, J., Hoffman, J. B., Reed, J. H., Gonsalves, A. E., Oh, J., Li, L., Hong, S., Jo, K. D., Dana, C. E., Miljkovic, N., Cropek, D. M., & Alleyne, M. (2020).

Molecular and topographical organization: Influence on Cicada Wing Wettability and bactericidal properties. *Advanced Materials Interfaces*, *7*(10), 2000112.

Roth, A. F., Wan, J., Bailey, A. O., Sun, B., Kuchar, J. A., Green, W. N., Phinney, B. S., Yates, J. R., & Davis, N. G. (2006). Global analysis of protein palmitoylation in yeast. *Cell*, *125*(5), 1003–1013.

Roy, R. K., & Lee, K.-R. (2007). Biomedical applications of diamond-like carbon coatings: A Review. *Journal of Biomedical Materials Research Part B: Applied Biomaterials*, *83B*(1), 72–84.

Rozen, S., & Skaletsky, H. (2000). Primer3 on the WWW for general users and for biologist programmers. *Bioinformatics Methods and Protocols*, 365–386.

Ruch, T. R., & Machamer, C. E. (2012). The coronavirus E protein: Assembly and beyond. *Viruses*, *4*(3), 363–382.

Running, M. P., Fletcher, J. C., & Meyerowitz, E. M. (1998). The Wiggum gene is required for proper regulation of floral meristem size in Arabidopsis. *Development*, *125*(14), 2545–2553.

Running, M. P., Lavy, M., Sternberg, H., Galichet, A., Gruissem, W., Hake, S., Ori, N., & Yalovsky, S. (2004). Enlarged meristems and delayed growth in *plp* mutants result from lack of Caax Prenyltransferases. *Proceedings of the National Academy of Sciences*, *101*(20), 7815–7820. https://doi.org/10.1073/pnas.0402385101

Running, M. P. (2014). The role of lipid post–translational modification in plant developmental processes. *Frontiers in plant science*, *5*, 50.

Rutherford, S., & Moore, I. (2002). The arabidopsis rab gtpase family: Another Enigma variation. *Current Opinion in Plant Biology*, *5*(6), 518–528.

Sakakibara, K., Nishiyama, T., Sumikawa, N., Kofuji, R., Murata, T., & Hasebe, M. (2003). Involvement of Auxin and a homeodomain-leucine zipper I gene in rhizoid development of the Moss *physcomitrella patens*. *Development*, *130*(20), 4835–4846.

Sakakibara, H. (2006). Cytokinins: Activity, biosynthesis, and translocation. *Annual Review of Plant Biology*, *57*(1), 431–449.

Salah, I., Parkin, I. P., & Allan, E. (2021). Copper as an antimicrobial agent: Recent advances. *RSC Advances*, *11*(30), 18179–18186.

Sampathkumar, A., Gutierrez, R., McFarlane, H. E., Bringmann, M., Lindeboom, J., Emons, A.-M., Samuels, L., Ketelaar, T., Ehrhardt, D. W., & Persson, S. (2013). Patterning and lifetime of plasma membrane-localized cellulose synthase is

dependent on actin organization in Arabidopsis interphase cells. *Plant Physiology*, *162*(2), 675–688.

Schaefer, D. G., & Zryd, J.-P. (1997). Efficient gene targeting in the moss Physcomitrella patens. *The Plant Journal*, *11*(6), 1195–1206.

Schafer, W. R., Trueblood, C. E., Yang, C.-C., Mayer, M. P., Rosenberg, S., Poulter, C. D., Kim, S.-H., & Rine, J. (1990). Enzymatic coupling of cholesterol intermediates to a mating pheromone precursor and to the Ras Protein. *Science*, *249*(4973), 1133–1139.

Schaefer, D. G., & Zrÿd, J.-P. (2001). The Moss PHYSCOMITRELLA patens, now and then. *Plant Physiology*, *127*(4), 1430-1438.

Schoeman, D., & Fielding, B. C. (2019). Coronavirus envelope protein: Current knowledge. *Virology Journal*, *16*(1).

Schumaker, K. S., & Dietrich, M. A. (1997). Programmed changes in form during Moss Development. *The Plant Cell*, 1099–1107.

Schwab, R., Ossowski, S., Riester, M., Warthmann, N., & Weigel, D. (2006). Highly specific gene silencing by artificial micrornas in *arabidopsis*. *The Plant Cell*, *18*(5), 1121–1133.

Seabra, M. C., Brown, M. S., Slaughter, C. A., Südhof, T. C., & Goldstein, J. L. (1992). Purification of component A of rab geranylgeranyl transferase: Possible identity with the choroideremia gene product. *Cell*, *70*(6), 1049–1057.

Sheahan, M. B., Rose, R. J., & McCurdy, D. W. (2004). Organelle inheritance in plant cell division: The actin cytoskeleton is required for unbiased inheritance of chloroplasts, mitochondria and endoplasmic reticulum in dividing protoplasts. *The Plant Journal*, *37*(3), 379–390.

Shi, W., Zeng, Q., Kunkel, B. N., & Running, M. P. (2016). ArabidopsisRab Geranylgeranyltransferases Demonstrate Redundancy and Broad Substrate Specificity in vitro. *Journal of Biological Chemistry*, *291*(3), 1398-1410.

Shinozawa, A., Otake, R., Takezawa, D., Umezawa, T., Komatsu, K., Tanaka, K., Amagai, A., Ishikawa, S., Hara, Y., Kamisugi, Y., Cuming, A. C., Hori, K., Ohta, H., Takahashi, F., Shinozaki, K., Hayashi, T., Taji, T., & Sakata, Y. (2019). SNRK2 protein kinases represent an ancient system in plants for adaptation to a terrestrial environment. *Communications Biology*, *2*(1).

Singanayagam, A., Patel, M., Charlett, A., Lopez Bernal, J., Saliba, V., Ellis, J., Ladhani, S., Zambon, M., & Gopal, R. (2020). Duration of infectiousness and correlation

with RT-PCR cycle threshold values in cases of COVID-19, England, January to May 2020. *Eurosurveillance*, *25*(32).

Skoog, F., & Tsui, C. (1948). Chemical control of growth and Bud Formation in tobacco stem segments and callus cultured in vitro. *American Journal of Botany*, *35*(10), 782–787.

Sluiter, A., Hames, B., Ruiz, R., Scarlata, C., Sluiter, J.,& Templeton, D. (2008). Determination of ash in biomass. Laboratory Analytical Procedure (LAP). Technical Report, 1−5 NREL/ TP-510−42622.

Sluiter, A., Hames, B., Ruiz, R., Scarlata, C., Sluiter, J., Templeton, D., and Crocker, D. (2011). Determination of structural carbohydrates and lignin in biomass. Laboratory Analytical Procedure (LAP). Technical Report, NREL/TP-510-42618.

Smith, L. G. (2003). Cytoskeletal control of plant cell shape: Getting the fine points. *Current Opinion in Plant Biology*, *6*(1), 63–73.

Sorek, N., Bloch, D., & Yalovsky, S. (2009). Protein lipid modifications in signaling and subcellular targeting. *Current Opinion in Plant Biology*, 12, 714–720.

Stepanova, A. N., Yun, J., Robles, L. M., Novak, O., He, W., Guo, H., Ljung, K., & Alonso, J. M. (2011). The *arabidopsis* yucca1 flavin monooxygenase functions in the indole-3-pyruvic acid branch of auxin biosynthesis. *The Plant Cell*, *23*(11), 3961–3973.

Stimmel, J. B., Deschenes, R. J., Volker, C., Stock, J., & Clarke, S. (1990). Evidence for an S-farnesylcysteine methyl ester at the carboxyl terminus of the saccharomyces cerevisiae Ras2 protein. *Biochemistry*, *29*(41), 9651–9659.

Strotbek, C., Krinninger, S., & Frank, W. (2013). The Moss Physcomitrella patens: Methods and tools from cultivation to targeted analysis of gene function. *The International Journal of Developmental Biology*, *57*(6-7-8), 553-564.

Su, Y.-H., Liu, Y.-B., & Zhang, X.-S. (2011). Auxin–cytokinin interaction regulates meristem development. *Molecular Plant*, *4*(4), 616–625.

Sun, Y., Pri-Tal, O., Michaeli, D., & Mosquna, A. (2020). Evolution of abscisic acid signaling module and its perception. *Frontiers in Plant Science*, *11*.

Szumlanski, A. L., & Nielsen, E. (2009). The Rab GTPASE Raba4d Regulates pollen Tube tip growth in Arabidopsis thaliana. *The Plant Cell*, *21*(2), 526–544.

Tam, T. H., Catarino, B., & Dolan, L. (2015). Conserved regulatory mechanism controls the development of cells with rooting functions in land plants. *Proceedings of the National Academy of Sciences*, *112*(29).

Tang, L., Tsai, C., Gerberich, W. W., Kruckeberg, L., & Kania, D. R. (1995). Biocompatibility of chemical-vapour-deposited diamond. *Biomaterials*, *16*(6), 483–488.

Thelander, M., Olsson, T., & Ronne, H. (2005). Effect of the energy supply on filamentous growth and development in Physcomitrella Patens. *Journal of Experimental Botany*, *56*(412), 653–662.

Thole, J. M., Perroud, P.-F., Quatrano, R. S., & Running, M. P. (2014). Prenylation is required for polar cell elongation, cell adhesion, and differentiation in *physcomitrella patens*. *The Plant Journal*, *78*(3), 441–451.

Thompson, G. A., & Okuyama, H. (2000). Lipid-linked proteins of plants. *Progress in Lipid Research*, *39*(1), 19–39.

Trevisan, A., Piovesan, S., Leonardi, A., Bertocco, M., Nicolosi, P., Pelizzo, M. G., & Angelini, A. (2006). Unusual high exposure to ultraviolet-C radiation. *Photochemistry and Photobiology*, *82*(4), 1077.

Triola, G. (2012). The Protein Lipidation and Its Analysis. *Journal of Glycomics & Lipidomics*, *01*(S1).

van Doremalen, N., Bushmaker, T., Morris, D. H., Holbrook, M. G., Gamble, A., Williamson, B. N., Tamin, A., Harcourt, J. L., Thornburg, N. J., Gerber, S. I., Lloyd-Smith, J. O., de Wit, E., & Munster, V. J. (2020). Aerosol and surface stability of SARS-COV-2 as compared with SARS-COV-1. *New England Journal of Medicine*, *382*(16), 1564–1567.

van Gisbergen, P. A. C., Li, M., Wu, S.-Z., & Bezanilla, M. (2012). Class II formin targeting to the cell cortex by binding pi(3,5)P2 is essential for polarized growth. *Journal of Cell Biology*, *198*(2), 235–250.

Vandenbrink, J. P., Kiss, J. Z., Herranz, R., & Medina, F. J. (2014). Light and gravity signals synergize in modulating plant development. *Frontiers in Plant Science*, *5*.

Verdiá-Báguena, C., Nieto-Torres, J. L., Alcaraz, A., DeDiego, M. L., Torres, J., Aguilella, V. M., & Enjuanes, L. (2012). Coronavirus e protein forms ion channels with functionally and structurally-involved membrane lipids. *Virology*, *432*(2), 485–494.

Vernoud, V., Horton, A. C., Yang, Z., and Nielsen, E. (2003) Analysis of the small GTPase gene superfamily of Arabidopsis. *Plant Physiol.* 131, 1191–1208.

Viaene, T., Landberg, K., Thelander, M., Medvecka, E., Pederson, E., Feraru, E., Cooper, E. D., Karimi, M., Delwiche, C. F., Ljung, K., Geisler, M., Sundberg, E., & Friml, J. (2014). Directional auxin transport mechanisms in early diverging land plants. *Current Biology*, *24*(23), 2786–2791.

Vidali, L., Augustine, R. C., Kleinman, K. P., & Bezanilla, M. (2007). Profilin is essential for tip growth in the Moss *physcomitrella patens*. *The Plant Cell*, *19*(11), 3705–3722.

Vidali, L., Rounds, C. M., Hepler, P. K., & Bezanilla, M. (2009). Lifeact-megfp reveals a dynamic apical F-actin network in tip growing plant cells. *PLoS ONE*, *4*(5).

Vidali, L., van Gisbergen, P. A., Guérin, C., Franco, P., Li, M., Burkart, G. M., Augustine, R. C., Blanchoin, L., & Bezanilla, M. (2009). Rapid formin-mediated actin-filament elongation is essential for polarized plant cell growth. *Proceedings of the National Academy of Sciences*, *106*(32), 13341–13346.

Vidali, L., Burkart, G. M., Augustine, R. C., Kerdavid, E., Tüzel, E., & Bezanilla, M. (2010). Myosin XI is essential for tip growth in *physcomitrella patens*. *The Plant Cell*, *22*(6), 1868–1882.

Vimbela, G., Ngo, S. M., Fraze, C., Yang, L., & Stout, D. A. (2017). Antibacterial properties and toxicity from metallic nanomaterials. *International Journal of Nanomedicine*, *Volume 12*, 3941–3965.

Vincent, M., Duval, R. E., Hartemann, P., & Engels-Deutsch, M. (2018). Contact killing and antimicrobial properties of copper. *Journal of Applied Microbiology*, *124*(5), 1032–1046.

V'kovski, P., Kratzel, A., Steiner, S., Stalder, H., & Thiel, V. (2020). Coronavirus Biology and replication: Implications for SARS-COV-2. *Nature Reviews Microbiology*, *19*(3), 155–170.

Voet, D., Voet, J. G., & Pratt, C. W. (2013). Fundamentals of Biochemistry: Life at the Molecular Level (4th ed.). John Wiley & Sons, Inc. p. 263.

Yalovsky, S. (1999). Lipid modifications of proteins – slipping in and out of membranes. *Trends in Plant Science*, *4*(11), 439–445.

Yang, K., Wang, L., Le, J., & Dong, J. (2020). Cell polarity: Regulators and mechanisms in plants. *Journal of Integrative Plant Biology*, *62*(1), 132–147.

Yang, W., Zhang, W., & Wang, X. (2016). Post-translational control of Aba signalling: The roles of protein phosphorylation and ubiquitination. *Plant Biotechnology Journal*, *15*(1), 4–14.

Yang, Y., Sage, T. L., Liu, Y., Ahmad, T. R., Marshall, W. F., Shiu, S.-H., Froehlich, J. E., Imre, K. M., & Osteryoung, K. W. (2011). Clumped chloroplasts 1 is required for plastid separation in *arabidopsis*. *Proceedings of the National Academy of Sciences*, *108*(45), 18530–18535.

Yi, P., & Goshima, G. (2020). Rho of plants GTPases and cytoskeletal elements control nuclear positioning and asymmetric cell division during Physcomitrella patens branching. *Current Biology*, *30*(14).

Wada, M., & Suetsugu, N. (2004). Plant Organelle positioning. *Current Opinion in Plant Biology*, *7*(6), 626–631.

Walker, A. S., Pritchard, E., House, T., Robotham, J. V., Birrell, P. J., Bell, I., Bell, J. I., Newton, J. N., Farrar, J., Diamond, I., Studley, R., Hay, J., Vihta, K.-D., Peto, T., Stoesser, N., Matthews, P. C., Eyre, D. W., & Pouwels, K. B. (2020). CT threshold values, a proxy for viral load in community SARS-COV-2 cases, demonstrate wide variation across populations and over time. *eLife* 10:e64683.

Walsh, C., Garneau-Tsodikova, S., & Gatto, G. (2006). Protein posttranslational modifications: The chemistry of Proteome Diversifications. *ChemInform*, *37*(7).

Wang, X., Kuang, T., & He, Y. (2010). Conservation between higher plants and the Moss Physcomitrella patensin response to the phytohormone abscisic acid: A Proteomics analysis. *BMC Plant Biology*, *10*(1).

Wang, Y. H., & Irving, H. R. (2011). Developing a model of plant hormone interactions. *Plant Signaling & Behavior*, *6*(4), 494–500.

Wang, J., Yao, X., & Huang, J. (2017). New tricks for human farnesyltransferase inhibitor: Cancer and beyond. *MedChemComm*, *8*(5), 841–854.

Wang, Y., Grunewald, M., & Perlman, S. (2020). Coronaviruses: An updated overview of their replication and pathogenesis. *Coronaviruses*, 1–29.

Waudby-West, R., Parcell, B. J., Palmer, C. N. A., Bell, S., Chalmers, J. D., & Siddiqui, M. K. (2021). The association between SARS-COV-2 RT-PCR cycle threshold and mortality in a community cohort. *European Respiratory Journal*, *58*(1), 2100360.

Weber, D. J., & Rutala, W. A. (2013). Self-disinfecting surfaces: Review of current methodologies and future prospects. *American Journal of Infection Control*, *41*(5).

Wellman, C. H., & Strother, P. K. (2015). The terrestrial Biota prior to the origin of land plants (embryophytes): A review of the evidence. *Palaeontology*, *58*(4), 601–627.

Wickett, N. J., Mirarab, S., Nguyen, N., Warnow, T., Carpenter, E., Matasci, N., Ayyampalayam, S., Barker, M. S., Burleigh, J. G., Gitzendanner, M. A., Ruhfel, B.

R., Wafula, E., Der, J. P., Graham, S. W., Mathews, S., Melkonian, M., Soltis, D. E., Soltis, P. S., Miles, N. W., … Leebens-Mack, J. (2014). Phylotranscriptomic analysis of the origin and early diversification of land plants. *Proceedings of the National Academy of Sciences*, *111*(45).

Wu, S.-Z., & Bezanilla, M. (2014). Myosin VIII associates with microtubule ends and together with actin plays a role in Guiding Plant Cell Division. *ELife*, *3*.

Wu, S.-Z., & Bezanilla, M. (2018). Actin and microtubule cross talk mediates persistent polarized growth. *Journal of Cell Biology*, *217*(10), 3531–3544.

Xue, F., Liu, J., Guo, L., Zhang, L., & Li, Q. (2015). Theoretical study on the bactericidal nature of nanopatterned surfaces. *Journal of Theoretical Biology*, *385*, 1–7.

Yalovsky, S., Loraine, A. E., & Gruissem, W. (1996). Specific prenylation of Tomato Rab proteins by geranylgeranyl type-II transferase requires a conserved cysteine-cysteine motif. *Plant Physiology*, *110*(4), 1349–1359.

Yalovsky, S., Rodr Guez-Concepcion, M., & Gruissem, W. (1999). Lipid modifications of proteins – slipping in and out of membranes. *Trends in Plant Science*, *4*(11), 439–445.

Yalovsky, S., Kulukian, A., Rodriguez-Concepcion, M., Young, C.A., & Gruissem, W. (2000). Functional requirement of plant farnesyltransferase during development in Arabidopsis. *Plant Cell*, *12*, 1267-1278.

Zaffina, S., Camisa, V., Lembo, M., Vinci, M. R., Tucci, M. G., Borra, M., Napolitano, A., & Cannatà, V. (2012). Accidental exposure to UV radiation produced by Germicidal Lamp: Case report and risk assessment. *Photochemistry and Photobiology*, *88*(4), 1001–1004.

Zhao, Y. (2010). Auxin biosynthesis and its role in plant development. *Annual Review of Plant Biology*, *61*(1), 49–64.

Zerial, M., & McBride, H. (2001). Rab proteins as membrane organizers. *Nature Reviews Molecular Cell Biology*, *2*(2), 107–117.

Zhang, B., Gao, Y., Zhang, L., & Zhou, Y. (2021). The plant cell wall: Biosynthesis, construction, and functions. *Journal of Integrative Plant Biology*, *63*(1), 251–272.

Zhang, F. L., & Casey, P. J. (1996). Protein prenylation: molecular mechanisms and functional consequences. *Annual Review of Biochemistry 65*(1), 241-269.

Zhou, Y., Yang, Y., Niu, Y., Fan, T. T., Qian, D., Luo, C., Shi, Y., Li, S., An, L., & Xiang, Y. (2020). The tip-localized phosphatidylserine established BY

ARABIDOPSIS ALA3 is crucial for Rab gtpase-mediated VESICLE trafficking and pollen TUBE Growth. *The Plant Cell*, *32*(10), 3170–3187.

Zuo, J., Niu, Q.-W., & Chua, N.-H. (2000). An estrogen receptor-based transactivator XVE mediates highly inducible gene expression in transgenic plants. *The Plant Journal*, *24*(2), 265–273.

CURRICULUM VITA

Hyun Jin Jung

Department of Biology, University of Louisville
139 Life Science Building, Louisville, KY 40292
Mobile Phone: +1 213 446 2973
Email: hi1guswls@gmail.com

EDUCATION

Ph.D., Cellular, Molecular & Developmental Biology **2017-2022**
University of Louisville, Louisville, KY, USA

M.S., Cellular, Molecular & Developmental Biology **2015-2017**
University of Louisville, Louisville, KY, USA

B.S., Biological Science, and Technology **2009-2014**
Chonnam National University, Gwangju, Korea

ACADEMIC WORK EXPERIENCE

Graduate Teaching Assistant **Spring 2022**
Department of Biology, University of Louisville, KY, USA

Graduate Research Assistant **Spring 2020-Fall 2021**
NSF-EPSCOR
Department of Biology, University of Louisville, KY, USA

Graduate Teaching Assistant **Fall 2015-Fall 2019**
Department of Biology, University of Louisville, KY, USA

PROFESSIONAL WORK EXPERIENCE

KAMPERS **2021-2022**
The Kentucky Advanced Partnership for Enhanced Robotics and Structures
NSF funded

- Participated in "Bio-mimicking Nanostructured Surfaces Testing Project" collaborated with engineers

KAMPERS **2020-2022**
The Kentucky Advanced Partnership for Enhanced Robotics and Structures
NSF funded

- Participated in "The COVID-19 Sanitizing Robot (Adaptive Robotic Nursing Assistant; ARNA) Testing Project" collaborated with engineers

KAMPERS **2020-2021**
The Kentucky Advanced Partnership for Enhanced Robotics and Structures
NSF funded

- Participated in the project titled "Bioproduction of Organic, Conductive and Biodegradable 3D print Materials"

Undergraduate Research Assistant (Junior & Senior years) **2011-2013**
School of Biological Sciences and Technology at Chonnam National University, Korea

- Participated in Field Study directed by professor Chul-Ho Yun in 'Globiotech Corporation' Institution

Project Assistant **2011**
School of Biological Sciences and Technology at Chonnam National University, Korea

- Participated in 'Improvement of Problem-Solving Research Project' titled "Improved method to generate human drug metabolites by cytochrome P450 enzymes" and conducted oral presentations.

TEACHING EXPERIENCE

Undergraduate Course Taught as Primary Instructor at University of Louisville
BIOL 331 (Genetics and Molecular Biology) **Spring 2022**

- Hands-on laboratory experiments course for students who have taken Cellular Molecular biology (BIOL 329) and who are currently taking or who have taken Genetics and Molecular biology (BIOL 330); 4 hour-classes/week; 2 sections/semester; Enrolled: ~20 students per lab

Undergraduate Course Taught as Primary Instructor at University of Louisville
BIOL 104 (Introduction to Biological System lab) **Fall 2015-Fall 2019 (including Summers)**

- Hands-on laboratory experiments course for non-science students; 2 hour-classes/week; 2~3 sections/semester; Enrolled: ~33 students per lab
- This course is designed to develop skills in scientific methodology, observation, and critical thinking.

Undergraduate Research Mentorship at University of Louisville
Dr. Mark Running Lab **Spring 2018- Spring 2022 (including summers)**
(Logan Dailey, Calvin Pham, Adam Moon, Melisa Noa, Julie Nwosu, Hallie Maxwell, Calvin Ramirez, Riley Eriksen, Melissa Martinez Zaldivar, Javier Pauig, Briana Seibert, Shahil Desai, Harshith Gontla, Aaron Gronewold, etc.)

RESEARCH & SCHOLARLY ACTIVITIES

Scholarly Presentations
Poster presentation, KY-NSF-EPSCoR Annual Conference Supercollider Meeting
University of Louisville, Speed Art Museum, April 22nd, 2022

The Three Minute Thesis (3MT™) competition
University of Louisville, March 8th, 2021

Poster presentation, KY-NSF-EPSCoR Annual Conference Supercollider Meeting
KAMPERS Conference & Student Research Showcase virtually over Zoom, February 23rd, 2021.

Poster presentation, KY-NSF-EPSCoR Annual Conference Supercollider Meeting
University of Kentucky, February 29th, 2020.

Oral presentation, American Society of Plant Biologists Midwestern Section Annual Meeting
West Virginia University, March 16-17th, 2019.

Poster presentation, Graduate Student Regional Research Conference (GSRRC)
University of Louisville, February 28th, 2019.

Oral presentation, GRADtalk GNAS Brown Bag Series
University of Louisville, November 12th, 2018.

Poster presentation, Graduate Student Regional Research Conference (GSRRC)
University of Louisville, March 3rd, 2018.

Poster presentation, B.S. Dissertation
Chonnam National University, December, 2014

Scholarly Workshops

Dissertation Writing Retreat
University of Louisville, May 10-14th, 2021

ACHIEVEMENTS

Doctoral Dissertation Completion Award for Summer 2022 (**Full tuition, health insurance, and $1,833.33 per month**)

Undergraduate Mentored Research Award in the amount of **$1,000** for a mentor; plus **$500** for an undergraduate researcher by College of Arts & Sciences at the University of Louisville for Spring 2022

Graduate Teaching Assistantship (**Full tuition, health insurance, and $11,000 semiannual stipend**) granted for Spring 2022 by the Department of Biology at the University of Louisville.

Undergraduate Mentored Research Award in the amount of **$1,000** for a mentor; plus **$500** for an undergraduate researcher by College of Arts & Sciences at the University of Louisville for Fall 2021

Undergraduate Mentored Research Award in the amount of **$1,000** for a mentor; plus **$500** for an undergraduate researcher by College of Arts & Sciences at the University of Louisville for Summer 2021

1st place winner in the graduate student category: Better Poster competition (**$100 Visa Gift card**) hosted by the NSF EPSCoR EOD Council & EPSCoR/IDeA Foundation, March 2021

Undergraduate Mentored Research Award in the amount of **$1,000** for a mentor; plus **$500** for an undergraduate researcher by College of Arts & Sciences at the University of Louisville for Spring 2021

Graduate Research Assistantship (**Full tuition, health insurance, and $22,000 annual stipend**) granted from Spring 2020 to Fall 2021 by NSF-EPSCoR.

Travel Award funded by the American Society of Plant Biologists in the amount of **$400** to West Virginia University for the 2019 Midwestern Section Annual Meeting.

Graduate Teaching Assistantship (**Full tuition, health insurance, and $22,000 annual stipend**) granted from Fall 2015 to Fall 2019 by the Department of Biology at the University of Louisville.

RESEARCH PUBLICATIONS

- Paxton, W. F., Rozsa, J. L., Brooks, M. M., Running, M. P., Schultz, D. J., Jasinski, J. B., **Jung, H. J.**, & Akram, M. Z. (2021). A scalable approach to topographically mediated antimicrobial surfaces based on Diamond. *Journal of Nanobiotechnology, 19*(1). https://doi.org/10.1186/s12951-021-01218-3

- Ryu, S. H., Park, B.-Y., Kim, S.-Y., Park, S.-H., **Jung, H.-J.**, Park, M., … Yun, C.-H. (2014). Regioselective Hydroxylation of Omeprazole Enantiomers by Bacterial CYP102A1 Mutants. *Drug Metabolism and Disposition, 42*(9), 1493–1497. doi: 10.1124/dmd.114.058636